EXPERIMENTAL INVESTIGATION ON INTERNAL COMBUSTION ENGINE FOR MICRO-COGENERATION APPLICATION FUELLED WITH ALTERNATIVE FUELS: ENERGY RECOVERY, PERFORMANCE AND POLLUTANTS FORMATION

Agnese Magno

A thesis submitted to UNIVERSITÀ DEGLI STUDI DI NAPOLI FEDERICO II

and produced in collaboration with ISTITUTO MOTORI-CNR of Napoli

in fulfilment of the requirements for the Degree of Doctor of Philosophy

in

Mechanical Engineering

Scuola di dottorato in Ingegneria Industriale

Dottorato di Ricerca in Ingegneria dei Sistemi Meccanici XXVII Ciclo

2015

TUTOR

COORDINATOR

Prof. Ing. Adolfo Senatore

Prof. Ing. Fabio Bozza

Dr. Ing. Ezio Mancaruso

Dott.ssa Bianca Maria Vaglieco

A nonno Salvatore

ACKNOWLEDGMENTS

I am deeply grateful to Dr. Bianca Maria Vaglieco who gave me the opportunity to conduct my research activity at Istituto Motori-CNR. She has created a competitive but cooperative and friendly research team and I am proud to work with her group.

I am appreciative to eng. Ezio Mancaruso and eng. Silvana Di Iorio for sharing their wealth of knowledge related to internal combustion engines.

Special thanks to Carlo Rossi and Bruno Sgammato for their precious technical support.

Thanks to the people that, directly and indirectly, contributed to my research activity: Paolo Sementa, Francesco Catapano, Luigi Sequino, Renato Marialto, prof. Gaetano Continillo, Katarzyna Bizon and Simone Lombardi.

Lastly, thanks to my parents and Antonella for their support and their patience.

ABSTRACT

This thesis was carried out within the project "Smart GRID con Sistemi di POLIgenerazione Distribuita" (POLIGRID) funded by Regione Campania. The experimental activity was conducted in the labs of Istituto Motori - CNR of Napoli.

Smart-grid technologies are the vision of the future in the energy supply. Their main advantages are the lower greenhouse gas emissions, improved energy efficiency, increased large scale renewable energy and distributed generation integration. Smart-grid technologies include cogeneration systems, wind turbines, photovoltaic systems, fuel cells and energy storage units. It can be argued that internal combustion engines, as element of cogeneration systems, play an important role in the development of such new technologies for energy distributed generation. Therefore, internal combustion engine optimization is needed to better integrate them with other energy production technologies. In particular, results reported in this thesis could be useful for the development of new technology of engine based micro-cogeneration system working at different engine speeds and loads.

This work is aimed to characterize in terms of energy recovery, combustion characteristics and pollutant emissions a small compression ignition engine for micro-cogeneration application fuelled with blended and pure biodiesel. The engine under investigation was a three-cylinder, 1028 cm^3 of displacement, equipped with a common-rail injection system. The engine was fuelled with diesel, a blend of 20% v/v rapeseed methyl ester (RME), a blend of 50% v/v RME and pure RME. Tests were performed at different operating conditions. The quantity and the quality of the waste heat energy, which can be used for cogeneration purpose, were evaluated through energy and exergy analyses, respectively. Combustion process was studied by means of thermodynamic analyses. The environmental impact of the engine in terms of combustion noise and pollutant emissions was investigated. In particular, an in-depth understanding of pollutants formation was provided by non-intrusive optical diagnostics application.

It was found out a trade-off between the waste heat of the exhaust gas and the cooling water. By waste heat recovery, the efficiency changes from 34% detected at 2000 rpm full load to 66% at 3400 rpm full load. The quantity and quality of energy recovered by exhaust gas decreases as the content of biodiesel increases meanwhile a defined trend of the heat recovered

from cooling water was not detected for the tested fuels. Lower noise emissions were found out when the engine is fuelled with blended and pure biodiesel. Lower carbon monoxide, hydrocarbons and particulate matter emissions were measured when the engine ran with both blended and pure RME. Higher nitrogen oxides emissions when the engine ran with biodiesel were observed, in particular at full load conditions. Optical measurements showed that, in medium load conditions, the exhaust gas recirculation has a stronger effect on reducing the flame temperature of biodiesel with respect to diesel fuel leading to nitrogen oxides emissions slightly higher than diesel fuel. Therefore, the analysis of the data revealed that a proper engine calibration could further optimize the combustion process and emission formation when the engine is fuelled with biodiesel.

CONTENTS

LIST OF FIGURES

LIST OF TABLES

NOMENCLATURE

Acronyms

ASI	After Start of Injection
ATDC	After Top Dead Center
bmep	Brake Mean Effective Pressure
bsfc	Brake specific fuel consumption
BTDC	Before Top Dead Center
B20	Blend of 20% v/v RME and 80% v/v diesel fuel
B50	Blend of 50% v/v RME and 50% v/v diesel fuel
B100	Pure RME
cad	Crank angle degree
CCD	Charge Coupled Device
CDM	Crank Angle Degree Marker
CHP	Combined Heat and Power
CI	Compression Ignition
CN	Cetane Number
CO	Carbon Monoxide
CO_2	Carbon Dioxide
CR	Common Rail
DEED	Dekati Engine Exhaust Diluter
DOC	Diesel Oxidation Catalyst
ECU	Electronic Control Unit
EEPS	Engine Exhaust Particle Sizer^{TM}
EGR	Exhaust Gas Recirculation
FAEE	Fatty Acid Ethyl Esters
FAME	Fatty Acid Methyl Esters
FID	Flame Ionization Detector
FS	Full Scale
FSN	Filter Smoke Number
HC	Hydrocarbon
HR	Heat released
ICE	Internal Combustion Engine
imep	Indicated Mean Effective Pressure
LHV	Low Heating Value
NO	Nitrogen Monoxide
NO_x	Nitrogen Oxides
NO_2	Nitrogen Dioxide
OH	Hydroxyl Radical
O_3	Ozone
PAH	Polycyclic Aromatic Hydrocarbons
PID	Proportional Integral Derivative
PM	Particle Matter
PMP	Particle Measurement Programme
PSDF	Particle Size Distribution Function

RME	Rapeseed Methyl Ester
ROHR	Rate of Heat Release
SI	Spark Ignition
SOF	Soluble Organic Fraction
TDC	Top Dead Center
TTL	Transistor-Transistor Logic

Symbols

a	Absorption
A	Mass of air per unit time
c	Mass fraction of carbon
C	Concentration
c_p	Specific heat at constant pressure
c_v	Specific heat at constant volume
C_1	First Planck's constant
C_2	Second Planck's constant
D_m	Mean particle diameter
D_p	Particle diameter
E_b	Monochromatic emissive power
ex	Specific exergy
$\dot{Ex}$	Exergy rate
F	Mass of fuel per unit time
h	Mass fraction of hydrogen
H	Enthalpy of formation
hv	Intensity of light
K	Absorption coefficient
L	Work
	Optical length
	Geometric thickness of the flame
L_{jet}	Jet length
L_{ref}	Reference length
m	Mass
$\dot{m}$	Mass Flow Rate
M	Molecular weight
n	Total number of particle size classes
N	Engine speed
	Particle number
o	Mass fraction of oxygen
p	Pressure
P	Power
Q	Absorption efficiency
	Heat transfer
$\dot{Q}$	Heat rate
R	Gas constant
s	Mass fraction of sulphur

T	Temperature
	Torque
T_a	Apparent temperature
U	Internal energy
V	Cylinder Volume
W	Work transfer
y	Atoms of hydrogen per carbon atom
% m/m	Mass Percent Concentration
% v/v	Volume Percent Concentration

Greek Symbols

α	Parameter depending on the physical and optical properties of the soot
γ	Specific heat ratio c_p/c_v
ε	Emissivity
η	Efficiency
θ	Crank angle
λ	Wavelength
ρ	Density

Subscripts

a	Air
alt	Alternator
b	Brake
comb	Combustion
e	Electric
ex	Exhaust
f	Fuel
fric	Friction
i	Particle size class
in	Input to the engine
ind	Indicated
int	Intake
w	Cooling water

Chapter 1

Introduction

1 Introduction

1.1 State of art

Industrialization, population growth and improved standard of living have led to increased fuel consumption and environmental pollution. A more efficient use of the limited energetic resources is needed to pursuit both the energy saving and environment protection goals.

Cogeneration, also referred as combined heat and power (CHP), has been identified as an alternative technology to solve energy related problems [1]. Cogeneration is the simultaneous generation in one process of thermal and electrical and/or mechanical energy [2]. The main advantage of a CHP system is the possibility to improve the efficiency of the fuel use. Less fuel is required to produce a given amount of electrical and thermal energy in a single cogeneration unit than what is needed to generate the same quantities of both types of energy with separate conventional technologies [3]. The lower fuel consumption and emissions associated with the cogeneration systems have prompted the governments to take leading roles in promote the use of cogeneration not only in industrial sectors but also in residential ones. European Union has suggested the micro-cogeneration as an element in future energy generation to meet renewable energy targets in the long term [4]. Micro-CHP systems, characterized by a maximum capacity below 50 kWe [4], represent a feasible way to supply electric and thermal power to residential buildings, hospitals, hotels and offices [5].

Internal combustion engines (ICE) are suitable for small scale cogeneration applications because of their robust nature, higher efficiencies at lower power ranges and reduced cost with respect to other prime movers such as micro-turbines, fuel cells and Stirling engines [6]. ICE allows to recover heat from exhaust gas, engine cooling water and lube oil [7]. Moreover, it is possible to produce electrical energy by coupling the engine to a generator.

Conventional CHP units work at fixed engine speed depending on the desired frequency output. In order to satisfy with user demand, power output is regulated by acting on the engine load. Higher efficiency and lower fuel consumption for partial load could be achieved by adjusting the speed of the ICE to its optimum efficiency [8]. This goal can be accomplished by using variable speed generators. They are characterized by almost constant efficiency at all the engine speeds of the working range [9, 10].

The knowledge of the energy flows available at different operating conditions could be useful for the development of ICE based cogeneration systems working at different engine speeds and loads [11, 12]. The first law of thermodynamics gives useful information on the distribution of the supplied fuel energy in the engine. The second law of thermodynamics completes and enhances the energy analysis with the concept of exergy that represents the potentiality of a thermal system to produce useful work [13]. Fu et al. [14] applied the methods of energy and exergy analysis to evaluate the energy utilization efficiency, the energy distribution and the waste heat energy characteristics of a four-cylinder, 1.0 L gasoline engine. They stated the importance to perform energetic and exergetic analysis of ICE under mapping characteristics in order to identify the suitable engine operating condition. They found out that the distribution of the various kinds of energy is influenced by working parameters such as load and engine speed.

Some studies deal with energetic and exergetic analyses of compression ignition (CI) engines [15, 16], nevertheless, detailed investigations throughout the operating range is still missing. The main drawback correlated to the use of CI engine for micro-CHP applications are both noise and pollutant emissions. In CI engines, the self-ignition of premixed fuel causes a rapid pressure rise, producing the well-known knock, which excites the gas in the combustion chamber and consequently induces its oscillations. Gas oscillations cause the surfaces of the engine to vibrate; acoustic radiation from the vibrating surfaces completes the transmission to the ear [17].

Regarding the problem of pollutant emissions, cogeneration allows to reduce emissions levels with respect to conventional technology for separate thermal and electrical energy production [3]. Nevertheless, the micro-cogeneration tends to move emissions from power plants, located outside of cities, to the city center. Therefore, the problem of emission from micro-CHP systems is an important issue of the research activity.

The emission reduction target has led to look for cleaner fuels such as biodiesel. Moreover, biodiesel is a feasible solution for those countries that do not have petroleum reserves and can produce biodiesel from resources available within the country [18]. Biodiesel most commonly comes from soybean oil in the United States and from rapeseed oil in Europe [19]. It can be used in existing CI engine, either pure or in blend, without any technological modification [20-22]. Biodiesel is environmental-friendly compared to diesel fuel: it emits lower hydrocarbons

(HC), carbon monoxide (CO) and particulate matter (PM) with respect to fossil fuels [23]. Analyses of particle emissions have shown that biodiesel combustion produces smaller particles with respect to diesel fuel [24, 25]. It was observed that smaller are the particles, higher their negative impact on human health [26]. Therefore, further investigations are necessary to assess the actual benefits on human health resulting from biodiesel combustion in CI engines. On the other hand, the effect of biodiesel on nitrogen oxides (NO_x) emissions is not yet fully understood. Increased NO_x emissions are, generally, reported in literature when fuelling with biodiesel [27]. An argument to justify this trend, that has received great attention, is the increased flame temperature with biodiesel due to a reduction in the radiative heat losses from soot particles, as a consequence of the lower amount of soot produced [28]. However, a definite trend was not found about NO_x emissions from biodiesel combustion because of their dependence on several factors such as the exhaust gas recirculation (EGR) [29]. Tsolakis et al. [30], in fact, found out that biodiesel emits amount of NO_x quite similar to diesel fuel at fixed EGR amount.

The main drawback of biodiesel is the lower low heating value (LHV) than diesel fuel, resulting in lower torque and higher brake specific fuel consumption (bsfc) at fixed injection strategy [31]. From the energy point of view, Jena et al. [32] studied the effect of oxygenated fuels on energy and exergy efficiencies of a CI engine. Their results showed that the increase of oxygen content in the fuel results in a better combustion and reduced irreversibility. Nevertheless, they concluded that a more intensive research on energetic potentiality of biodiesel is needed. Abedin et al. [33] also suggested an in-depth investigation on energy balance at different test points to assess the feasibility of alternative fuels.

Several studies have investigated the effects of both blended and pure biodiesel on engine performance, efficiency and exhaust emissions [34-37]. However, invaluable insight for a better understanding of the biodiesel combustion evolution and pollutant formation could be provided by non-intrusive diagnostics such as optical measurements. Optically accessible engines have been widely used to detect combustion evolution and pollutant formation [38-50]. Dec et al. [44, 45] studied the combustion evolution in a heavy-duty, direct-injection diesel engine. To provide optical access, the engine was equipped with an extended piston and piston crown window; moreover, one of the two exhaust valves was replaced with a window in the cylinder head. Sison et al. [46] studied the effect of two oxygenated fuels on in-cylinder

soot temperature and concentration by two-colour pyrometry method. Their investigation was carried out on a single cylinder research engine equipped with the head of a 2.0 L, common rail (CR) production engine. They found out that the oxygenated fuels produce lower soot concentration during combustion and burn with lower flame temperature with respect to diesel fuel. Similar results were found out by Mancaruso et al. [47-50] in studies dealing with the injection and combustion investigation on an optically accessible cylinder equipped with the head of a 2.0 L, CR production engine. However, bottom view images acquisition requires modifications of the engine geometry resulting in a large field of view but also in changed flow characteristics. Moreover, optically accessible cylinders entail challenges such as speed and load limitations [51]. In order to overcome these difficulties, less intrusive measurements involving small diameter endoscopes can be performed [52-55]. This solution allows to investigate in-cylinder phenomena without comprehensive mechanical modifications and with minimal interference to the combustion process [51]. Jeon et al. [54] analysed the effect of injection timings and pressure on the flame temperature, combustion and exhaust emission characteristics in a 0.5 L, CR single cylinder research engine fuelled with biodiesel. They detected flames images by an endoscope fitted in the cylinder head and used dedicated software to apply the two-colour pyrometry method. They found out that the in-cylinder flame temperature and soot concentration directly affect the NO_x and PM formation, respectively. Aoyagi et al. [55] also used endoscope based optical diagnostic to investigate in-cylinder phenomena of an experimental 2.0 L single cylinder engine fuelled with diesel. In particular, they measured, by means of dedicated software, the flame temperature and soot concentration by two-colour pyrometry at different EGR levels. They stated that the diesel flame detection by an endoscope system is useful and very practical in spite of the limited observation range. They found out that when the EGR rate increases, the flame temperature and the exhaust NO_x decrease.

1.2   Objectives

The objective of this thesis is to characterize in terms of energy recovery, combustion characteristics and pollutant emissions a small CI engine for micro-CHP application. The

investigated engine is a three-cylinder, 1028 cm^3 of displacement with a CR injection system. Engine was fuelled with diesel fuel, and both blended and pure biodiesel of first generation.

This study aims to improve the knowledge on energy distribution and waste heat energy characteristics of a CI engine fuelled with both blended and pure biodiesel, at different operating conditions. For this purpose, energetic and exergetic analysis were carried out; in particular, the heat recovered from exhaust gas and from the engine cooling water was evaluated. Thermodynamic analyses of the combustion process were performed by detecting the in-cylinder pressure signal. Pressure data were elaborated to calculate the rate of heat release (ROHR) and the engine combustion noise. Gas emissions and PM were measured at raw exhaust by commercial instruments. Particles were characterized in terms of number and diameter at diluted exhaust too. The pollutant formation was investigated by combustion phase detection through non-intrusive optical diagnostic. Flames images were post-processed by two-colour pyrometry method to assess the flame temperature and the radiation of sooting flames that were correlated to NO_x and PM emissions measured at exhaust, respectively.

The novelty of the present work consists in employing optical diagnostic techniques for the optimization, mainly in terms of pollutant emission reduction, of a cogeneration system. Moreover, the experimental results have pointed out the need of dedicated injection strategies when the engine is fuelled with biodiesel.

1.3   Thesis layout

The thesis is arranged in four main sections. Chapter 2 provides an overview of the CI engines: the essential thermodynamics, the background of the combustion process, combustion noise and pollutant emissions are described. Moreover, the application of CI engines for micro-CHP systems is presented.

Chapter 3 focuses on the experimental apparatus, located in the labs of Istituto Motori-CNR, which was used to develop the research activity. The tested fuels and the operating conditions investigated are also presented.

Chapter 4 discusses the results of the experimental activity. Energetic and exergetic analyses of the engine are reported. Thermodynamic analysis of the combustion process, with particular

attention to the combustion noise, is shown. Optical data of combustion phase are reported and they are correlated to the pollutant emissions measured at exhaust.

The last section presents the main conclusions and the suggestions for further works.

Additional information with regard to various chapters is presented in the Appendices A, B, C.

Chapter 2

Compression Ignition Engine

2 Compression Ignition Engine

2.1 Background

Although the history of the diesel engine extends back into the closing years of the 19th century when Dr. Rudolf Diesel began his pioneering work on air blast injected stationary engine, and in spite of the dominant position it now holds in many applications, e.g. marine propulsion, land transport, both road and rail, and electrical power generation, it is today the subject of intensive development and capable of improvements [17].

The major distinguishing characteristic of the diesel engine is the compression ignition principle. CI engines operate with a heterogeneous charge of previously compressed air and a finely divided spray of liquid fuel. The latter is injected into the engine cylinder towards the end of compression when, after a suitably intensive mixing process with the air already in the cylinder, the self-ignition properties of the fuel cause combustion to be initiated from small nuclei. These spread rapidly so that complete combustion of all injected fuel, usually with air-fuel ratios well in excess of stoichiometric, is ensured. Therefore, the mixing process is crucial to the operation of the diesel engine and as such has received a great attention [56-58].

Diesel engine represents a true alternative power unit because of its higher performance and better fuel efficiency with respect to the gasoline engine. The increase in performance of diesel engine has been made possible by key engine component system developments. Firstly, there have been significant improvements in fuel injection system operating pressure, together with greater flexibility of timing and the number of injection events per cycle, which has been enabled by the development of CR fuel injection systems. More sophisticated electronic controls have been developed for greater flexibility and refinement of the engine systems to provide better power and response, and more acceptable noise levels. In parallel with these developments, EGR systems have become more sophisticated, and more efficient exhaust after-treatments in the form of diesel oxidation catalysts (DOC) and particulate traps have been developed [59].

The future of CI engines will be influenced by two factors: the development of alternative power plants, and the future cost and availability of suitable fuels. In the near future, CI engines could play an important role in electrical energy production, for example in

cogeneration units. Regarding the fuel availability, liquid fuels are by far the most convenient energy source for CI engine and the majority of such fuels come from crude oil. The price of petroleum based fuels is largely governed by political and taxation policy. In order to overcome this issue, CI engines could also be fuelled with renewable energy source such as vegetable fuels.

2.2   CI engine applications: micro-cogeneration systems

Cogeneration, also known as combined heat and power (CHP), consists in the simultaneous production of electrical and/or mechanical energy and thermal energy from a single energy source [2]. CHP systems consist of a prime mover, an electrical generator and heat recovery systems. CHP plants exist in various scales ranging from micro-CHP (< 50 kW$_e$) used for single family homes to large-scale facilities for industrial application such as pulp and paper mills, steel mills, and chemical processing plants.

The European Union currently generates 11.2% of its electricity using cogeneration [60]. However, there are wide differences between member states as shown in Figure 2.1, with varied shares of cogeneration ranging from 0% to 47.4%. According to official Eurostat data, there is no cogeneration in Malta, and very little in Cyprus (0.9%) or Greece (4.5%). Latvia has the greatest share of cogeneration in total electricity generation (47.4%) followed by Denmark (46.2%). In Italy the cogeneration reaches the 11.5%.
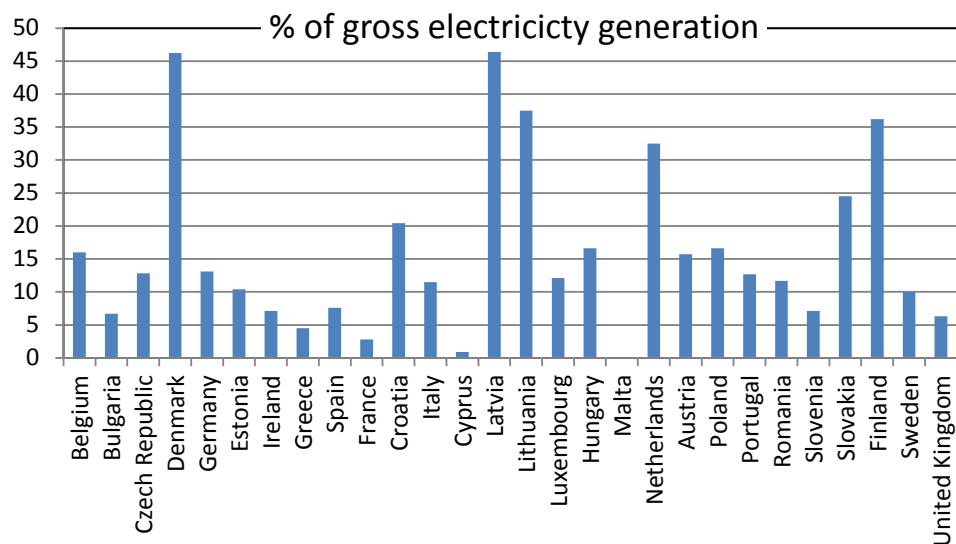
Figure 2.1. Eurostat data on share of CHP in total electricity generation [60]

The main benefits resulting from cogeneration application can be summarized as follows:

− increased efficiency of energy conversion and use;

− lower emissions to the environment;

− large cost savings, providing additional competitiveness for industrial and commercial users while offering affordable heat for domestic users too;

− an opportunity to move towards more decentralized forms of electricity generation where plants are designed to meet the needs of local consumers providing high efficiency, avoiding transmission losses and increasing flexibility in system use;

− an opportunity to increase the diversity of generation plant and provide competition in generation;

− improved local and general security of energy supply: local generation, through cogeneration, can reduce the risk of consumers being left without supplies of electricity and/or heating.

Cogeneration units are classified by the prime mover that could be ICEs, turbines, fuel cells and Stirling engines. In particular, CI engine based micro-CHP is the main focus of the present thesis. Figure 2.2 shows the schematic diagram of an ICE based cogeneration unit. ICEs provide mechanical energy at the crankshaft that can be used to drive an electrical generator to produce electricity; moreover, mechanical energy can also be used to drive rotating equipment such as compressors, pumps, and fans. The heat is available from exhaust gas, engine jacket cooling water, and in a smaller extent from lube oil. Exhaust gases typically leave the engine at temperature between 200 and 500˚C; they can be used to generate medium pressure steam (about 10 bar). The heat recovered from the engine jacket is at temperature between 80 and 90°C, and it can be used to generate hot water.
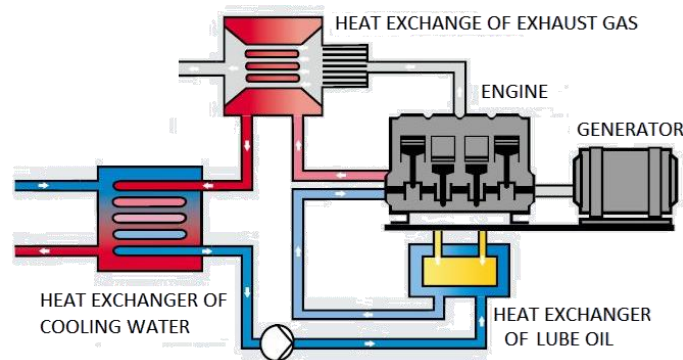
Figure 2.2. Schematic diagram of ICE based cogeneration system.

Some indexes are defined to evaluate the performance of a cogeneration unit. The first law efficiency, η_I, of a cogeneration system is calculated as follow:

$$\eta_I = \frac{P_e + \dot{Q}_{ex} + \dot{Q}_w}{\dot{Q}_{in}}$$

(2.1)

where P_e is the electric power that could be obtained by coupling the engine to an alternator and it is calculated as:

$$P_e = P_b \cdot \eta_{alt}$$

(2.2)

where P_b is the engine brake power and η_{alt} is the efficiency of the electric generator. Moreover, $\dot{Q}_{ex}$ is the heat rate lost with the exhaust gas, $\dot{Q}_w$ is the heat rate of engine cooling water and $\dot{Q}_{in}$ is the fuel heat rate input to the engine.

To take into account the different values of the electrical and thermal energy, the second law efficiency, η_{II}, of a cogeneration system can be calculated as follows:

$$\eta_{II} = \frac{P_e + \dot{Ex}_{\dot{Q}_{ex}} + \dot{Ex}_{\dot{Q}_w}}{\dot{Ex}_{in}}$$

(2.3)

where $\dot{Ex}_{\dot{Q}_{ex}}$ and $\dot{Ex}_{\dot{Q}_w}$ are the exergy rate of the exhaust gas and cooling water, respectively, while $\dot{Ex}_{in}$ is the fuel exergy rate input to the engine.

2.3 Energy recovery

2.3.1 Energy analysis

Energy and exergy analysis of ICE are useful means to evaluate its feasibility for cogeneration purpose. It is known that in an ICE, the chemical energy of the fuel is converted into heat energy by means of the combustion process. Since a fraction of the fuel chemical energy is not

fully released inside the engine and it is lost with the exhaust gas, it is useful to define the combustion efficiency, η_{comb}, as [19]:

$$\eta_{comb} = 100 \cdot \frac{LHV_f - (H_{NO_2} \cdot NO_2 + LHV_{CO} \cdot CO + LHV_f \cdot HC + LHV_{PM} \cdot PM)}{LHV_f} \qquad (2.4)$$

where LHV and H are the low heating value and the enthalpy of formation of the species, respectively. The combustion energy losses take into account the energy required to form nitrogen dioxide (NO_2) and the energy lost due to incomplete oxidation of CO to carbon dioxide (CO_2) and HC fuel to CO_2 and H_2O.

According to the first law of thermodynamics applied to an ICE, a part of the combustion energy provided by the fuel is converted into effective work and some is released to the environment with exhaust gas and cooling water. The remaining part is lost because of the heat radiation of the engine and frictional losses. Except for the waste heat that has to be necessarily released to the environment, according to the second law of thermodynamics, the rest can be utilized in order to improve the ICE efficiency.

If the ICE is considered as a control volume (surrounded by control surface), as shown in Figure 2.3, than the energy flowing from and to the engine are:

− IN: fuel, with its associated heat of combustion plus air, consumed by the engine.

− OUT: brake power, exhaust loss, cooling water loss and both convection and radiation heat to the surroundings.
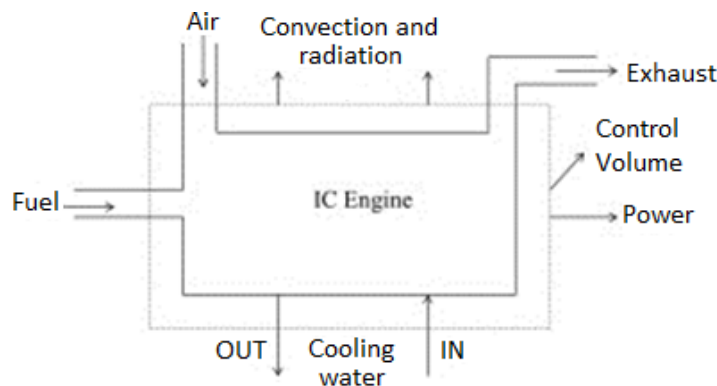
Figure 2.3. Control volume of ICE showing energy flows [33].

The steady state first law equation, for the control volume shown in Figure 2.3 can be expressed as follows [57]:

$$\dot{Q}_{in} = P_b + \dot{Q}_w + \dot{Q}_{ex} + \dot{Q}_{loss} \tag{2.5}$$

$\dot{Q}_{in}$ is the fuel heat rate input to the engine and it is calculated using the mass flow rate, $\dot{m}_f$, and the LHV of the fuel:

$$\dot{Q}_{in} = \dot{m}_f \cdot LHV_f \tag{2.6}$$

P_b is the brake power and it is calculated with experimental data of speed, N, and brake torque, T_b:

$$P_b = 2 \cdot \pi \cdot N \cdot T_b \tag{2.7}$$

The heat rate recovered from engine water, $\dot{Q}_w$, was calculated by means of an energetic balance on the heat exchanger external water to engine water, on the external water side:

$$\dot{Q}_w = \dot{m}_w \cdot c_{p,w} \cdot \Delta T_w \tag{2.8}$$

where $\dot{m}_w$ is the mass flow rate of water; $c_{p,w}$ is the specific heat capacity of water, and ΔT_w is the water temperature difference at outlet and inlet of the engine.

The heat rate lost with the exhaust gas, $\dot{Q}_{ex}$, can be calculated as:

$$\dot{Q}_{ex} = (\dot{m}_a + \dot{m}_f) \cdot c_{p,a}(T_{ex}) \cdot (T_{ex} - T_0) \tag{2.9}$$

where the mass flow rate of the exhaust gas was calculated as sum of intake air, $\dot{m}_a$, and fuel mass flow rate, $\dot{m}_f$; $c_{p,a}$ is the specific heat capacity of the air detected at the temperature of the exhaust gas, T_{ex}, and T_0 is the ambient reference temperature.

Heat rate loss from engine control volume, $\dot{Q}_{loss}$, can be written as:

$$\dot{Q}_{loss} = \dot{Q}_{in} - \left(P_b + \dot{Q}_w + \dot{Q}_{ex} \right) \tag{2.10}$$

$\dot{Q}_{loss}$ includes the heat transfer by radiation to the environment from hot external surfaces (crankcase and cylinder wall) of the engine and the friction losses, P_{fric}:

$$P_{fric} = P_{ind} - P_b$$

(2.11)

where P_{ind} is the indicated power:

$$P_{ind} = \frac{L_{ind} \cdot N}{2} \tag{2.12}$$

L_{ind} is the indicated work calculated as:

$$L_{ind} = \oint p dV \tag{2.13}$$

in which p is the in-cylinder pressure and V is the engine volume.

The amount of heat carried out by lubricating oil is very small and it will be neglected in this study.

The fuel conversion efficiency, η_f, is calculated as the ratio of the net power output to the fuel heat rate input:

$$\eta_f = \frac{P_b}{\dot{Q}_{in}} \tag{2.14}$$

2.3.2 Exergy analysis

According to the second law of thermodynamics the evaluation indicator of energy is not only the quantity, but also the quality. Compared to effective mechanical energy, waste heat energy is a kind of low grade energy since it requires various kinds of thermodynamic cycles to convert into effective work. In accordance with Carnot principle, the maximum efficiency of thermodynamic cycles cannot be higher than Carnot cycle efficiency. Thus, only part of waste heat energy can be recovered. From this viewpoint, exergy analysis is more useful to evaluate

the waste heat energy characteristics. Exergy is defined as the maximum theoretical work that can be obtained when a system of interest interacts with a reference environment to equilibrium. It indicates the maximum recoverable energy of waste heat energy. The mathematical expression of exergy is given as:

$$\dot{Ex}_{\dot{Q}} = \dot{Q} \cdot \left(1 - \frac{T_0}{T}\right) \tag{2.15}$$

where $\dot{Ex}_{\dot{Q}}$ is the exergy rate of the waste heat rate $\dot{Q}$ of exhaust gas or cooling water. T_0 and T are the reference temperature and the waste heat temperature, respectively. The exergy efficiency is calculated as the ratio of the exergy content of an energy source and the fuel exergy rate input to the engine, $\dot{Ex}_{in}$:

$$\eta_{\dot{Ex}} = \frac{\dot{Ex}_{\dot{Q}}}{\dot{Ex}_{in}} \tag{2.16}$$

$\dot{Ex}_{in}$ is calculated as:

$$\dot{Ex}_{in} = \dot{m}_f \cdot ex_f \tag{2.17}$$

where ex_f is the specific chemical exergy of the fuel: for liquid fuel it can be calculated according to the following expression on unit mass basis [61]:

$$ex_f = \left[1.0401 + 0.1728\frac{h}{c} + 0.0432\frac{o}{c} + 0.2169\frac{s}{c}\left(1 - 2.0628\frac{h}{c}\right)\right] \cdot LHV_f \tag{2.18}$$

where h, c, o and s are the mass fraction of hydrogen, carbon, oxygen and sulphur, respectively.

2.4 Combustion process

As mentioned in the previous section, CI engines are particularly suitable for cogeneration application. However, they suffer from high NO_x and PM emissions. Moreover, diesel engines

are characterized by high combustion noise. Both pollutant and noise emissions are correlated to the combustion evolution. Therefore, it is helpful to have a physical knowledge of the diesel combustion process in order to address significant reductions in both engine-out emissions (prior to after-treatment) and engine noise.

A conceptual model of diesel combustion that employs a single injection event near the top dead center (TDC) at the end of the compression stroke was developed by Dec [44, 45].
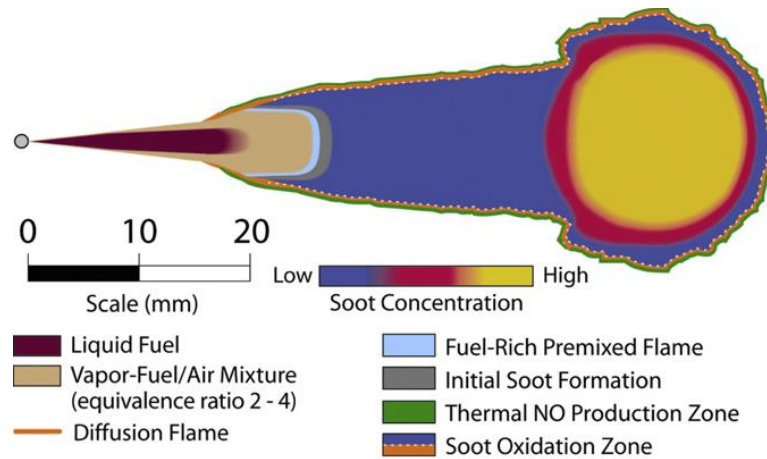
Figure 2.4. Schematic of a reacting direct injection diesel jet [44].

Figure 2.4 presents an idealized schematic of diesel combustion: it shows the main features of a free reacting diesel fuel jet during the quasi-steady period of combustion which occurs between the end of the premixed burn and the end of fuel injection. This representation of diesel combustion is appropriate for typical heavy-duty diesel engines operating at moderate to high load conditions. As soon as the cold fuel jet starts to penetrate into the combustion chamber, it begins to mix with the hot compressed air. As penetration increases, more and more hot air is entrained, the droplets begin to vaporize and a sheath of vaporized heated fuel-air mixture forms around the jet periphery. When the temperature inside this fuel-rich zone reaches about 750 K, the first reactions, resulting in a breakdown of high cetane fuel, begin to occur. These reactions, as well as the further entrainment of hot air and the additional compression of the cylinder charge, increase the temperature and the rate of the reactions. The products of these basic reactions are largely C_2H_2, C_2H_4, and C_3H_3 fuel fragments as well as CO and H_2O. Then, the temperature and reaction rate increase quickly resulting in a burning of the complete fuel-air mixture that has been formed during the ignition delay. This sudden combustion of well-prepared fuel-air mixture results in a strong and sudden increase of heat

release and in-cylinder pressure, the so-called premixed peak. The strong pressure gradients cause considerable noise, and the high temperatures in the premixed zone are responsible for a first production of NO_x. Due to the triple bond of N_2-molecules, temperatures of about 2000 K must be reached in order to split the molecules and to enable the formation of NO_x (Zeldovich mechanism). However, as soon as these temperatures are reached, the NO_x production increases exponentially with temperature. The premixed combustion consumes all fuel-air mixture around the inner spray region. The temperatures of the inner spray region increases to about 1600–1700 K and all available oxygen in this region is consumed by partial oxidation of the fuel fragments. From now on, air and partial burnt products, which diffuse from inside the spray to the outer regions, are burnt in a very thin reaction zone at the periphery of the spray, the so-called diffusion flame. This kind of combustion is limited by the mixing of partial burnt products and air, resulting in a slower reaction compared to the premixed one. The fuel drops being injected heat up due to the entrainment of hot air and combustion products into the jet near the nozzle. As the evaporated fuel further penetrates into the spray, it breaks down into small molecules, which are then subject to partial oxidation due to the lack of sufficient oxygen inside the hot spray cloud. The partial oxidation reactions and the heat transferred form the diffusion flame keep the temperature of the inner zone at values of about 1600–1700 K. These high temperatures, in combination with the low oxygen content, are ideal conditions for the formation of soot; therefore, large amounts of soot are produced in the inner cloud. The products from inside this partial oxidation zone diffuse to the boundary and are consumed by the diffusion flame. The diffusion flame is fed with oxygen from the surrounding of the burning spray, and near stoichiometric equivalence ratios are reached at its outer zone. Due to the very high temperatures, of about 2700 K, nearly all soot entering the diffusion flame is consumed. At the outer boundary of the hot diffusion flame, there is enough oxygen to produce large amounts of NO_x. After the end of the injection process, the partial burning zone is no longer fed with fuel vapor, and it can be consumed by the diffusion flame. The reduction of soot finally becomes stronger than the production, and the overall amount of soot inside the combustion chamber decreases [62].

An extension of Dec's conceptual model of diesel combustion for actual engines was given by Musculus et al. [63]. The model is for highly dilute (~13% intake O_2), low-load (~4 bar indicated mean effective pressure, imep) conditions with ignition occurring at or after the end

of injection. They proposed a model for light-duty engines, with either early or late injection, in which in-cylinder surfaces and flows significantly deflect the fuel jets. An approximate picture of how the low temperature combustion conceptual model applies to light-duty engines is presented in Figure 2.5.
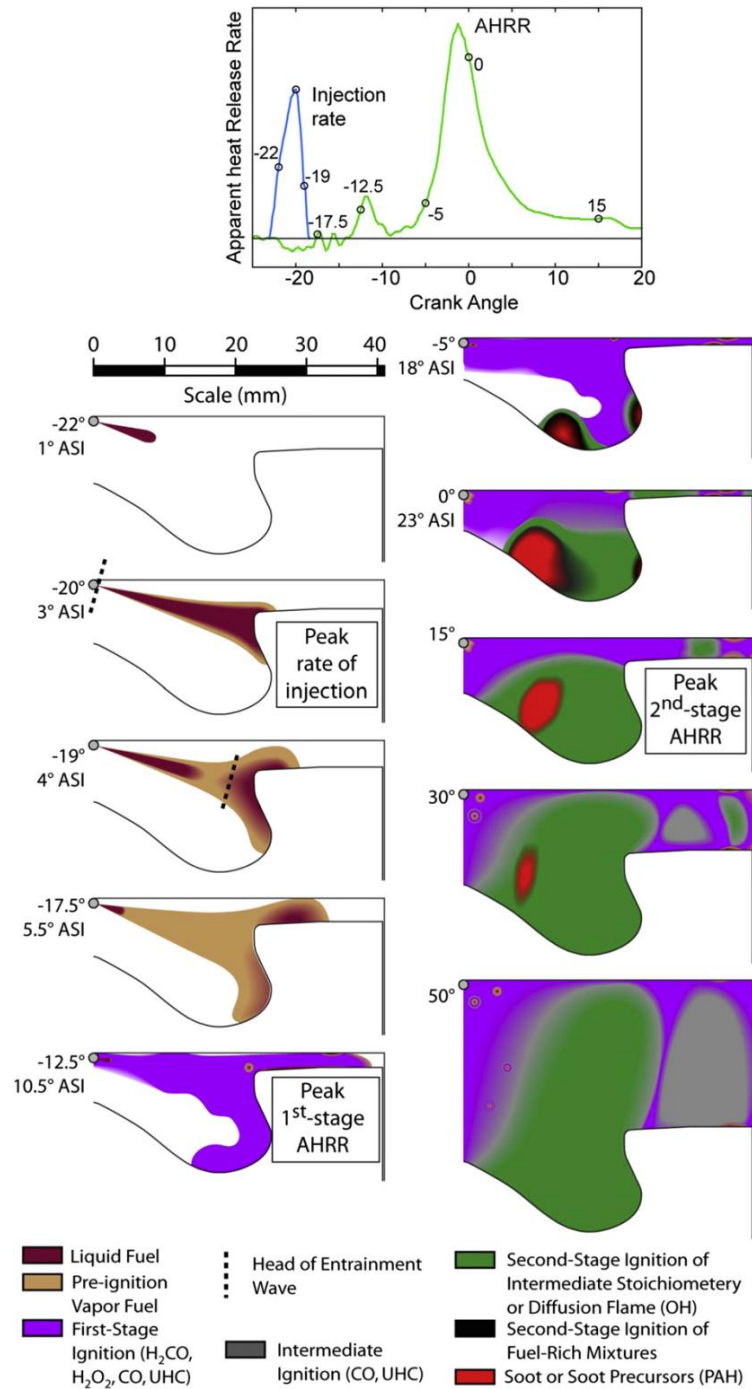
Figure 2.5. Conceptual model for single early-injection, low load, EGR-diluted, PCCI low-temperature light duty DI diesel combustion [63].

Liquid and vapor fuel initially penetrate together, with little difference seen in the penetration of the two phases. The peak rate of injection occurs at 3 crank angle degree (cad) after the start of injection (ASI). As the injection rate falls after 3 cad ASI, the entrainment wave is initiated at the injector but the liquid phase has already impacted the bowl rim. Near the end of injection at 4.5 cad ASI, the liquid core retreats toward the injector; liquid fuel also remains near the bowl rim, at the head of the jet. The liquid near the bowl rim persists for a few more cads, and penetrates farther into the squish volume and deeper into the bowl, as well as leaving a fuel film around the bowl rim. Generally, the maximum liquid penetration is similar to the maximum observed vapor penetration. The heat release associated with the first stage of ignition peaks near -12.5 cad after TDC (ATDC): a zone associated to unburned hydrocarbon is observed. By -5 cad ATDC, at the start of the second-stage heat release, a distinct two-zone distribution associated with fuel rich mixture are observed. Just beyond the peak apparent heat release rate near TDC, second-stage ignition has been reached in much of the mixture deep in the bowl (0 cad ATDC). At this time, polycyclic aromatic hydrocarbons (PAH), soot, zone is more pronounced. At the start of second-stage heat release, equivalence ratios are sufficiently low that significant soot or PAH is not formed. While over-lean mixture between the fuel jets is undoubtedly present and leads to regions of unburned H_2CO and HC along the head near the bowl rim and well within the squish volume, on both the head and piston surface. From this time onward (0 cad ATDC and later), volume expansion induced by piston motion push/draw the lean mixture exhibiting continued H_2CO zones into the squish volume, eventually forming a two-zone distribution of HC and CO. In the inner zone near the cylinder center, the HC and the CO distribution is dominated by lean mixture within which discrete fuel droplets are embedded.

The model above described for light duty engines is valid for a single injection; however, it is well known that modern high speed direct injection engines are equipped with high pressure CR system capable of multiple injections. Therefore, a deepen insight of the combustion evolution can be provided by experimental tests. In this regard, Figure 2.6 shows a selection of images of combustion process detected in a research engine equipped with the head of four-cylinder, 2 L, commercial engine. It is provided with a second-generation CR injection system with 6-holes piezoelectric injectors. In particular, the images refer to the operating conditions at the engine speed of 1500 rpm and 2 bar of brake mean effective pressure (bmep). This

operating condition is characterized by two injections with a pressure of 615 bar: the pilot injection occurs at 13.5 cad before TDC (BTDC) with a duration of 180 µs and the main injection occurs at 3.5 cad BTDC with a duration of 440 µs. Moreover, EGR percentage of 44% was set. Premixed flames are not visible in the images since they are characterized by too low luminosity to be distinguishable. Diffusion flames are visible due to the burning high temperature carbon particles. In particular, at first crank angles, after the main injection is finished, diffusion flames propagate along the fuel jets towards the bowl wall. They are localized at the spray side of the jets because of the swirl motion that moves the fuel vapour out of the spray and forms an ignitable fuel-air mixture in rich condition. At 10 cad ATDC, the diffusion flames spread out over the entire combustion chamber, showing very high luminosity proving the presence of high soot concentration regions. Then, the luminosity decreases (21 cad ATDC) and the flames remain close to the bowl wall up to the depletion of the impinged fuel.

| 4 cad ATDC | 6 cad ATDC | 8 cad ATDC | 10 cad ATDC | 13 cad ATDC | 21 cad ATDC |
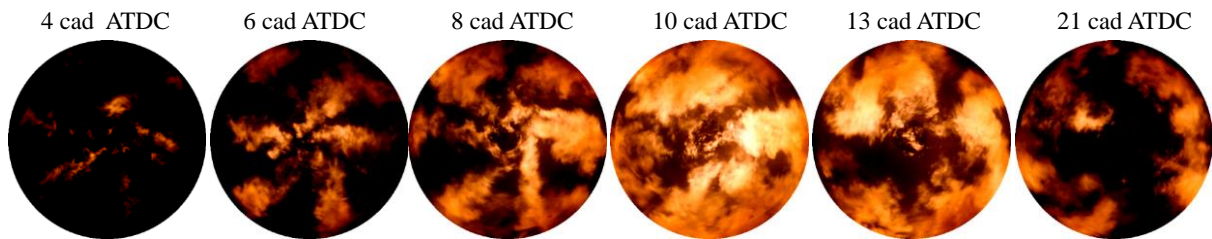
Figure 2.6. Images of combustion process detected in a research engine equipped with the head of a commercial engine [38].

2.5   Combustion noise

Combustion process is the most important noise source in CI engines. The cause of this phenomenon is associated with the sudden pressure rise, due to the initial fuel and air mixture ignition inside the cylinder, which is one of the main features of combustion in diesel engines. This abrupt pressure gradient produces the well-known "diesel knock" and it is a very strong excitation source that excites the oscillation of the burned gases in the combustion chamber. Because of its regular geometry, a resonance effect leads to the establishment of different modes of oscillation and thus, after a short time of stabilization, a periodic pressure evolution is established in the combustion chamber. This non-stationary phenomenon induces the block wall to vibrate and, conversely, this vibration causes noise radiation [64]. Much of the

literature suggests that combustion noise depends almost entirely upon the peak rate of pressure rise caused in turn by an initial peak in the rate of heat release. For individual engines, quite good relationships exist between peak rate of rise in-cylinder pressure and the noise that originates directly in the combustion processes. However, when such relationships for several different engines are compared, large discrepancies appear. The shape of the cylinder pressure curve can be related to the Fourier Analysis (or spectrum) of the cylinder pressure quite simply [17]:

- the compression ratio and turbocharger boost ratio directly influence the level of components up to 500 Hz (as well as indirectly influencing the peak rate of pressure rise via the compression temperature and hence the ignition delay);

- the peak cylinder pressure influences the average level of low frequency spectrum components up to between 500 and 900 Hz;

- the peak rate of pressure rise influences the components between 500/900 Hz and 3/5 kHz depending upon the engine speed, turbocharger boost (if any) and the rate of injection diagram.

- the second derivative of pressure with respect to time can influence very high frequency components (above 5 kHz).

The first option to reduce combustion noise is to reduce the ignition delay and hence the quantity of fuel that contributes to the premixed burn. Pilot injection reduces the fuel injected during the ignition delay, and hence the heat released from the premixed burn. Control of the initial rate of injection and 'boot-shaped' injection rate diagrams are effective for the same reasons. EGR will reduce the rate of the premixed burn and hence the peak rate of rise in the cylinder pressure [17].

2.6 Pollutant formation

Figure 2.7 shows the typical composition of exhaust gas from a modern direct injection diesel engine at full load. The part of pollutant emissions is only 0.3 %vol. The highest part of this 0.3 %vol is formed by NO_x and particulates. Following are described the main pollutants of a diesel engine
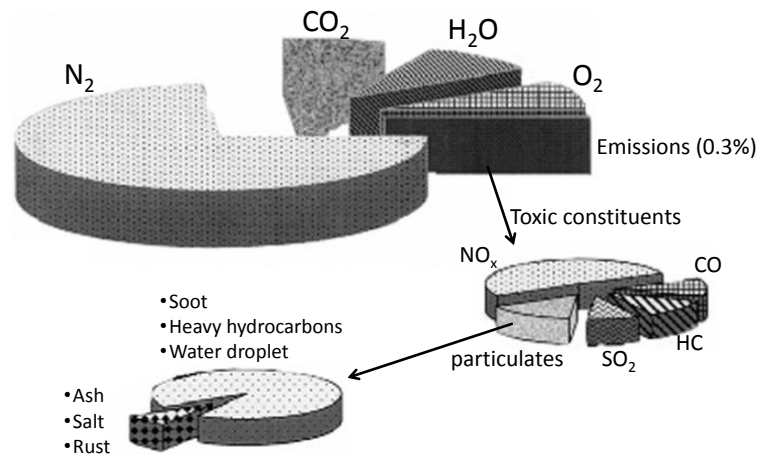
Figure 2.7. Exhaust gas composition of diesel engine [59].

Nitrogen Oxides

The term nitrogen oxide refers to a group of nitrogen and oxygen based chemical compounds with varying atom-to-atom relationships. Nitrogen monoxide (NO) is the main component (>90%). It is essentially produced in three different ways during combustion processes [59]:

− *Thermal NO* is formed at high temperatures (T > 2200 K) in the burnt component of the working medium (post-flame range) from molecular nitrogen in the combustion air. This process is initiated by oxygen radicals and assisted by hydroxyl radical (OH). The reaction kinetics that form the basis of thermal NO formation can be described using the extended Zeldovich mechanism.

− *Prompt NO* is also formed from molecular atmospheric nitrogen, but inside the radical-enriched main reaction zone of hydrocarbon combustion (flame zone). The temperatures reached at this point are practically the same as the temperatures present under adiabatic combustion conditions and achieve maximum values up to 2800 K depending on the air–fuel mixture and localised air–fuel ratio.

− *Fuel NO* is formed by the oxidation of the nitrogen chemically bound within the fuel. Before entering the combustion zone, nitrogen within the fuel is converted to radicals or compounds of the cyan compounds that partially oxidise to form NO in the flame zone. However, the nitrogen content of standard diesel fuels is so low that the fuel NO formation can be disregarded.

Investigations carried out to date indicate that in diesel engine combustion processes NO is essentially formed via the formation mechanism of thermal NO. The extended Zeldovich

mechanism forms the basis of thermal NO formation and encompasses the following reactions:

$$N_2 + O = NO + N \qquad\qquad (2.19)$$

$$N + O_2 = NO + O \qquad\qquad (2.20)$$

$$N + OH = NO + H \qquad\qquad (2.21)$$
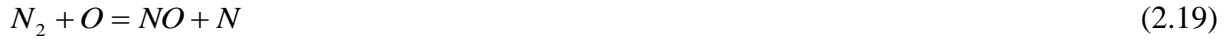
Figure 2.8 shows the thermal NO formation rate in combustion products formed by burning a mixture of a typical hydrocarbon fuel with air. The critical time period is when burned gas temperatures are at a maximum. Mixture which burns early in the combustion process is especially important since it is compressed to a higher temperature, increasing the NO formation rate, as combustion proceeds and in-cylinder pressure increases. After the time of peak pressure, burned gas temperatures decrease as the in-cylinder gases expand. The decreasing temperature due to expansion and due to mixing of high-temperature gas with air or cooler burned gas freezes the NO chemistry [57].
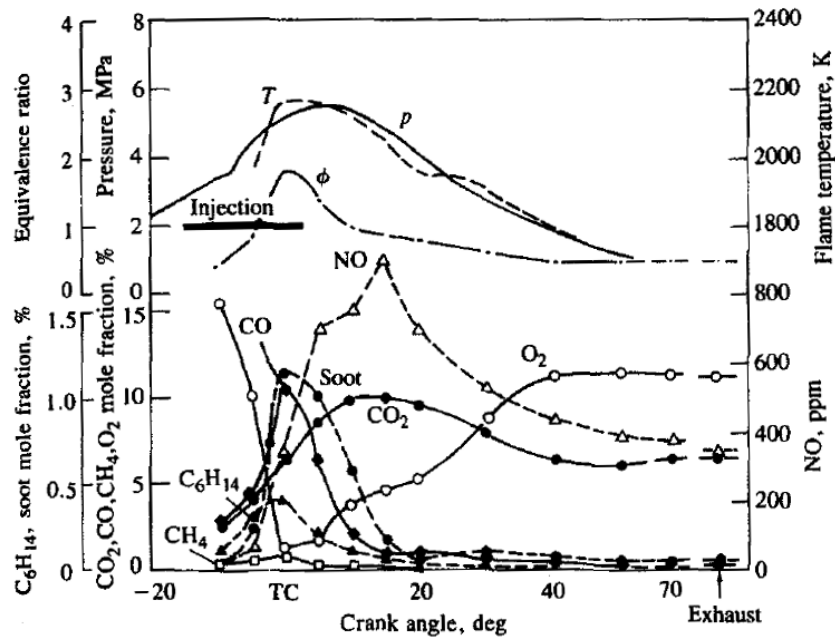
Figure 2.8. NO concentration and other combustion product species measured in a combustion chamber of a DI engine with rapid sampling valve [57].

Particulate Matter

Soot is not a clearly defined substance, but in general terms, soot is a solid element consisting of roughly eight parts carbon and one part hydrogen. Soot is formed from unburned fuel, which nucleates from the vapour phase to a solid phase in fuel-rich regions at elevated temperatures. Hydrocarbons or other available molecules may condense on, or be absorbed by soot depending on the surrounding conditions. PM is the combination of soot and other liquid or solid-phase materials that are collected when exhaust gases pass through a filter. Particulate is often separated into a soluble and an insoluble or dry fraction. The fraction of particulate, which is soot, is often estimated by finding the insoluble portion.

The evolution of liquid- or vapour-phase hydrocarbons to solid soot particles involves six commonly identified processes: pyrolysis, nucleation, coalescence, surface, growth, agglomeration, and oxidation. A sequence depicting the first five of these processes comprises the soot formation process as pictured schematically in Figure 2.9, while oxidation, the sixth process, converts hydrocarbons to CO, CO_2 and H_2O at any point in the process [65].
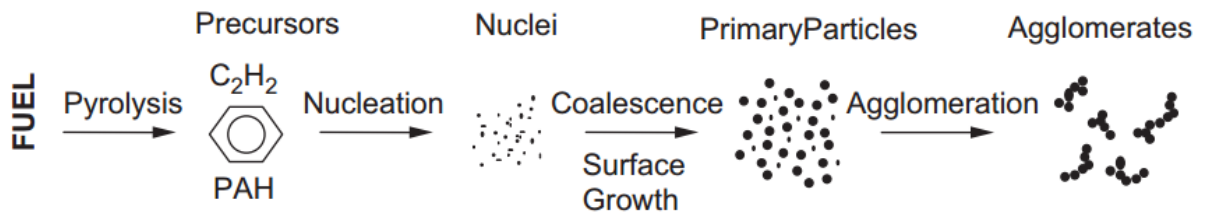
Figure 2.9. Schematic diagram of the steps in the soot formation process from gas phase to solid agglomerated particles [65].

Oxidation is the conversion of carbon or hydrocarbons to combustion products. It occurs when the temperature is higher than 1300 K; OH is most likely to dominate soot oxidation under fuel-rich and stoichiometric conditions while under lean conditions, soot is oxidized by both OH and O_2.

Pyrolysis is the process of organic compounds, such as fuels, altering their molecular structure in the presence of high temperature without significant oxidation even though oxygen species may be present. Pyrolysis results in the production of some species which are precursors or building blocks for soot. Soot precursor formation is a competition between the rate of pure fuel pyrolysis and the rate of fuel and precursor oxidation by OH. Both pyrolysis and oxidation rates increase with temperature, but the oxidation rate increases faster. This explains

why premixed flames (where some amount of oxygen is present) soot less and diffusion flames (no oxygen is present in the pyrolysis region) soot more as the temperature increases. All fuels undergo pyrolysis and produce essentially the same species: unsaturated hydrocarbons, polyacetylenes, PAH and, especially, acetylene. If enough O and OH are present, some acetylene is oxidized to relatively inert products. C_2H_2, C_2H_4, CH_4, C_3H_6 and benzene are typical pyrolysis products too.

Nucleation or soot particle inception is the formation of particles from gas-phase reactants. Particle nuclei do not contribute significantly to the total soot mass, but do have a significant influence on the mass added later, because they provide sites for surface growth. Spatially, nucleation is restricted to a region near the primary reaction zone where the temperatures and radical and ion concentrations are the highest in both premixed and diffusion flames.

Surface growth is the process of adding mass to the surface of a nucleated soot particle. There is no clear distinction between the end of nucleation and the beginning of surface growth and the two processes are concurrent. During surface growth, the hot reactive surface of the soot particles readily accepts gas-phase hydrocarbons, which appear to be mostly acetylenes. This leads to an increase in soot mass, while the number of particles remains constant.

Coalescence and agglomeration are both processes by which particles combine. Coalescence occurs when particles collide and coalesce, thereby, decreasing the number of particles and holding the combined mass of the two soot particles constant. During coalescence, two roughly spherically shaped particles combine to form a single spherically shaped particle. Agglomeration occurs when individual or primary particles stick together to form large groups of primary particles. The primary particles maintain their shape. Typically, the combined soot particles form chain-like structures, but in some cases clumping of particles has been observed.

Figure 2.10 shows idealized diesel exhaust particle number and mass weighted particle size distribution function (PSDF). The distributions shown are trimodal, lognormal in form. The concentration of particles in any size range is proportional to the area under the corresponding curve in that range. Most of the particle mass exists in the so-called accumulation mode in the 0.1-0.3 µm diameter range. This is where the carbonaceous agglomerates and associated adsorbed materials reside. The nuclei mode typically consists of particles in the 0.005-0.05 µm diameter range. This mode usually consists of volatile organic and sulfur compounds that form

during exhaust dilution and cooling, and may also contain solid carbon and metal compounds. The nuclei mode typically contains 1-20% of the particle mass and more than 90% of the particle number. The coarse mode contains 5-20% of the particle mass. It consists of accumulation mode particles that have been deposited on cylinder and exhaust system surfaces and later reentrained. Also shown in Figure 2.10 are some definitions of size for atmospheric particles: PM10, diameter (D)<10 μm; fine particles, D<2.5 μm; ultrafine particles, D<0.10 μm; and nanoparticles D<0.05 μm or 50 nm [66].
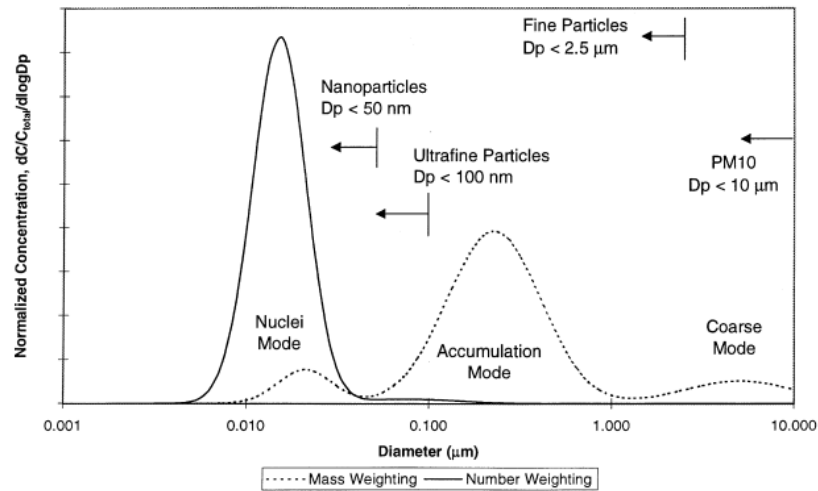
Figure 2.10. Typical engine exhaust PSDF [66].

Carbon Monoxide

Carbon monoxide results from incomplete combustion. CO concentration is largely dependent on air/fuel mixture and it is the highest where the excess-air factor is less than 1.0. In the rich mixtures, due to air deficiency and reactant concentration, all the carbon cannot convert to CO_2 and resulting in CO formation. Although CO is produced during operation in rich mixtures, a small portion of CO is also emitted under lean conditions because of chemical kinetic effects. Diesel engines operate in lean mode so the formation of CO is minimal. Nevertheless, CO is produced if the droplets in a diesel engine are too large or if insufficient turbulence or swirl is created in the combustion chamber [67].

Unburned hydrocarbon

The causes of unburned hydrocarbon emissions are the same as these of CO. The molecular bonds of heavy fuel components break down at high temperatures in the combustion chamber, forming a variety of HC with smaller carbon-atom chains (thermal cracking). They are

27

surrounded by the flame during subsequent combustion. However, the flame cannot propagate further in certain areas of the spray as the necessary preconditions (oxygen concentration and temperature) do not exist (quenching effect). HC cannot be oxidised further in these areas and remain unburned until the end of combustion unless they reach areas with more favourable oxidation conditions by suitable flow characteristics. The zones close to walls and the spray core and periphery are critical in this regard [59].

Chapter 3

Experimental details

3 Experimental details

3.1 Measurement equipment

The research activity was carried out in the labs of Istituto Motori of CNR. Figure 3.1 shows a schematic diagram of the experimental setup: it includes a CI engine loaded by an electrical dynamometer, the data acquisition systems, the optical diagnostic arrangement and the emissions measurement devices. These different modules of the experimental apparatus are described in detail in the next sections.

1.	Test engine	6.	High speed data acquisition	11.	Mexa 7100 DEGR
2.	Dynamometer	7.	Low speed data acquisition	12.	Smoke Meter
3.	DOC	8.	Endoscope & CCD camera	13.	EEPS
4.	Air flow meter	9.	AVL ThermoVision system		
5.	Fuel balance	10.	Delay Unit		
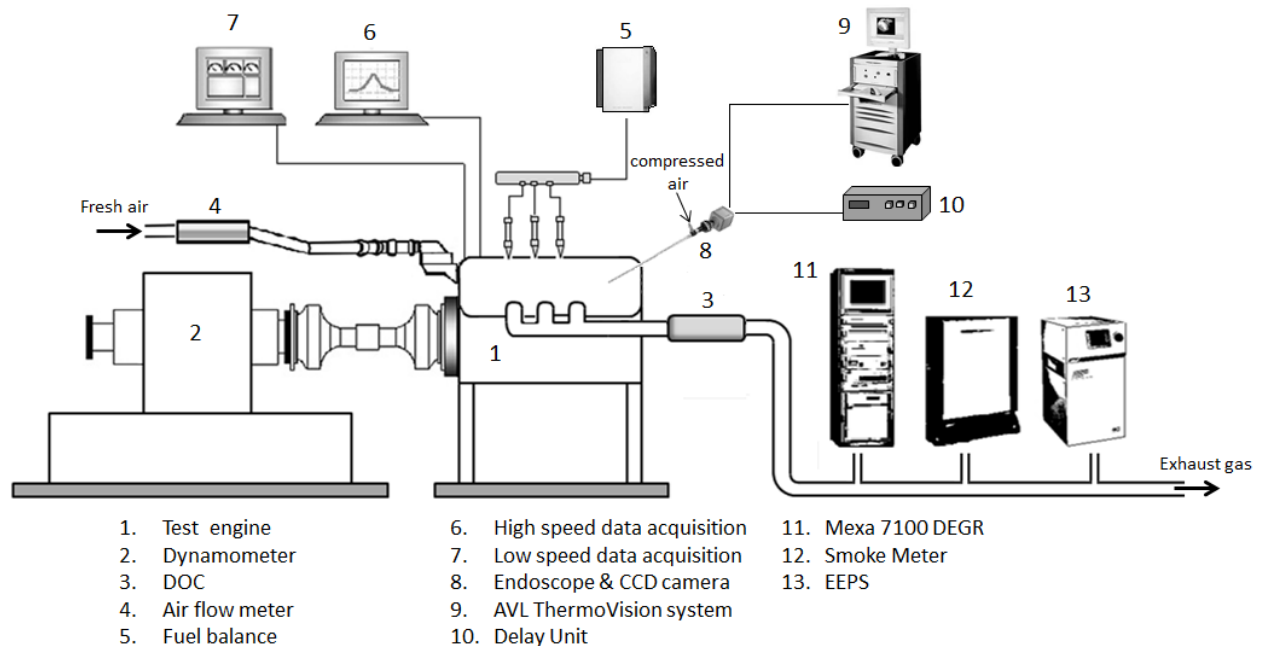
Figure 3.1. Experimental setup.

3.1.1 Compression Ignition Engine

The investigation was carried out on a three-cylinder, six valves, four stroke, naturally aspirated, 1028 cm^3, CI engine shown in Figure 3.2. It is compact in size and of high performance: maximum torque and maximum power are available at low rotational speeds. The main engine specifications are listed in Table 3.1. The engine is equipped with an electronically controlled CR injection system characterized by a unit pump operated by a three-lobe cam that allows to reach a maximum injection pressure of 1400 bar. The engine is provided with a closed electronic control unit (ECU). The engine has two emission reduction

systems: a cooled EGR for NO_x and a DOC for CO and HC. Moreover, a proper engine calibration guarantees low particle emissions. The engine cooling system was arranged to keep the temperature of the cooling water at 80°C. The original water pump was used to circulate the coolant through the engine and the liquid-to-air radiator of the real configuration was replaced by a shell and tube exchanger. The temperature of the engine coolant was controlled by adjusting the flow of cold water through the heat exchanger via a control valve operated by a proportional-integral-derivative (PID) temperature controller.

Figure 3.2. Engine setup.

Table 3.1. Engine specifications.

Engine	Compression ignition
Number of Cylinders	3, in-line
Bore [mm]	75.0
Stroke [mm]	77.6
Displacement [cm³]	1028
Compression Ratio	17.5:1
Max. Power [kW]	15 @ 3600 rpm
Max. Torque [Nm]	60 @ 2000 rpm
Injection System	Direct, CR electronic control
Max injection pressure [bar]	1400
Intake	Naturally Aspirated

3.1.2 Measurement setup

The engine was coupled to an electrical dynamometer characterized by maximum power of 100 kW and maximum speed of 5300 rpm. It allows to measure the engine torque output with a resolution of 1 Nm. The injection strategies were set by a closed ECU: a hall-effect sensor mounted on the injector of the first cylinder was used to detect the injector drive current while the EGR level set by the ECU was evaluated by measuring the recirculated CO_2 in the intake manifold. The gravimetric balance AVL730 was used to measure the fuel consumption on a time of 30 s; the balance was calibrated with an accuracy of 0.1 g. Inlet air mass flow rate was measured by a hot-wire sensor. The engine was instrumented with K thermocouples and pressure transducers PTX 1400 to measure the temperature and the pressure, respectively, in the intake and exhaust manifold. Low speed data collection of pressure, temperature was performed by homemade software developed in LabVIEW. In particular, three thermocouples were located at exhaust of each cylinder and another one was positioned downstream the DOC. The latter provided the exhaust gas temperature at which the heat could be recovered (Figure 3.3a). Moreover, the exhaust gas mass flow rate was calculated as sum of intake air and fuel mass flow rate in order to calculate the heat released from exhaust gas. Two thermocouples were used to measure the temperature of the cold water at the inlet and outlet of the shell and tube exchanger. An ultrasonic flow meter with a resolution of 0.001 L/min and a measurement range of 0.1-8 L/min was used to determine the flow rate of the cold water at the inlet of the exchanger (Figure 3.3b). The density of the cold water at the mean temperature in the exchanger was evaluated in order to calculate the mass flow rate. The knowledge of the water mass flow rate together with the temperature in the exchanger allowed to calculate the heat that could be recovered from the cooling water.
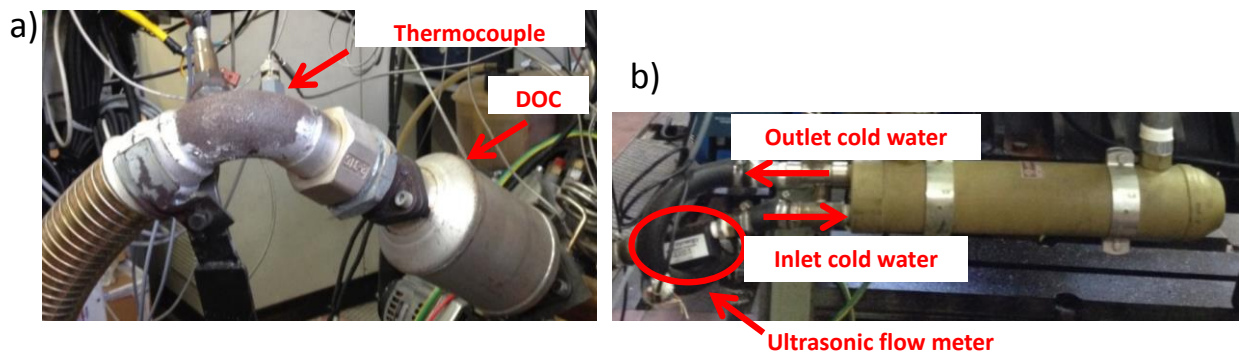
Figure 3.3. Waste heat sources: a) exhaust manifold; b) cooling water exchanger.

AVL Piezoelectric transducers with a sensitivity of 15.6 pc/bar and a natural frequency of 130 Hz were used to detect the pressure signal in the combustion chamber. Pressure sensors were mounted in the head of both the first and the third cylinder by means of glow plug adaptors. The electrical charge output of the sensor was converted into a voltage by the amplifier and then it was sent to the AVL Indimodul that is a high-speed data acquisition system. Pressure signals of 200 cycles were recorded and they were post-processed by the AVL Indicom software for thermodynamic analysis. An optical shaft encoder AVL365 C was used to transmit the crankshaft position to the AVL acquisition system. The information was in digital pulses, the encoder has two outputs, the first one is the TRIGGER; it has a resolution of 1 pulse/revolution and it is the TDC index signal. The second one is the crank angle degree marker (CDM) characterized by a resolution of 1 pulse/0.025°. The engine is a 4-stroke and the encoder gives as output two TDC signal per engine cycle so, in order to have the right crankshaft position, one pulse is suppressed via software.

3.1.3 Optical setup

In order to have an optical access in the combustion chamber, a hole for endoscope was designed in Istituto Motori and realized in the first cylinder of the engine. The endoscope accesses the combustion chamber via an adaptor provided with a sapphire window of 5 mm of diameter. Digital imaging of the combustion process was performed by the pixelfly VGA, a charge coupled device (CCD) camera produced by pco. The main camera specifications are listed in Table 3.2. The camera was equipped with a c-mount adaptor and a 25 mm lens. The camera spatial resolution is 9.5 pixel/mm.

Table 3.2. Pixelfly camera specifications [68].

Camera	CCD
Resolution [pixel]	640 x 480
Pixel size [μm^2]	9.9 x 9.9
Quantum efficiency @ 500 nm [%]	40
Frame rate [fps]	50
Spectral range [nm]	290 - 1100
Exposure time [s]	5 μs - 65 s
Dynamic range [bit]	12

Figure 3.4. a) Endoscope field of view; b) image detected in the combustion chamber.
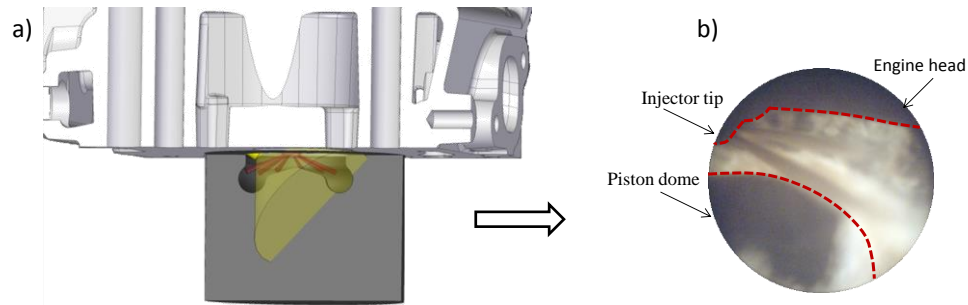
Before starting the tests, an endoscope was placed in the glow plug seat and it was connected to a strobe light in order to illuminate the combustion chamber; the other endoscope was connected to the CCD camera. This arrangement allowed a proper focus of the camera. In motored conditions, the endoscope used to light the chamber was removed and replaced by piezoelectric pressure transducer while the other endoscope was used to detect images of the combustion process. The housing of the endoscope was cooled by means of compressed air in order to stand for long time in a system at high pressure and temperature. The endoscope provides a field of view of 100°. Figure 3.4a shows a visualization of the endoscope field of view in the bowl while Figure 3.4b shows a typical image of combustion process detected by the endoscope: the injector tip and the piston dome are clearly distinguishable. Before starting imaging measurements, the engine ran in motored condition for a considerable period to warm up the system. Images were detected with an angular range of 1 cad and high gain. Exposure time and gain were properly set to detect the flame as bright as possible without causing saturation. The synchronization of the CCD camera with the engine was made by the crank angle encoder signal through a delay unit. AVL Indimodul recorded the transistor-transistor logic (TTL) signal of the CCD acquisition together with the pressure trace from the piezoelectric transducer; in this way, it was possible to determine the crank angles where optical data were detected. The camera is not cycle resolved and images were detected at crank angles of different engine cycles. For each image, 3 repetitions were acquired in order to take into account the cycle-to-cycle variability. Images were acquired by the AVL VisioScope that is a digital image acquisition and analysis system. Then, images were post-processed by the AVL ThermoVision program that allows to apply the two colour pyrometry method to the flame images. Details about the two colour pyrometry theory are reported in APPENDIX A.

3.1.4 Emissions Measurement Systems

The exhaust line was provided with three probes located downstream the DOC in order to take samples of exhaust gas to be sent to the emissions measurement systems. Steady-state measurements of CO, CO_2, HC, NO_x and PM were performed at the raw exhaust. Particles were characterized in terms of number and diameter at diluted exhaust.

Gas emissions were measured by Horiba MEXA 7100 DEGR analysers whose main specifications are reported in Table 3.3.

Table 3.3. Horiba MEXA 7100 DEGR specifications [69].

Pollutant	Measurement technique	Range	Repeatability
CO	Non Dispersive Infrared	min. 0-5000 ppm; max 0-12 %vol	< 0.5% FS
CO_2	Non Dispersive Infrared	0-20 %vol	< 0.5% FS
HC	Flame Ionization Detector	min. 0-500 ppmC; max 0-50000 ppmC	< 0.5% FS
NO/NO_x	Chemiluminescence	min 0-500 ppm max 0-10000 ppm	< 0.5% FS

Non-dispersive infrared (NDIR) analysers were used for measuring concentrations of CO and CO_2. Their principle of operation is based on the absorption of infrared radiation by these gases. For example, CO absorbs at about 4.6 µm whereas CO_2 absorbs at about 4.2 µm. The amount of radiation absorbed, *a*, is given by Beer's law [70]:

$$a_\lambda = 1 - \exp(-C_i Q_\lambda L) \tag{3.1}$$

where

− C_i is the concentration of the species i;

− Q_λ is the absorption efficiency;

− L is the optical path length.

Therefore, the NDIR analyser works by passing a pulsed beam of infrared light through a chamber containing the sampled gas. The amount of light absorbed by the measured gas is detected and is converted into an electrical signal. The electrical signal then is scaled to provide the concentration of the measured gas.

The technique for HC measurement is the flame ionization detector (FID). A sample of exhaust gas is passed through a hydrogen flame that burns any HC present in the sample gas. An electrical current is passed across the flame and it changes in proportion to the amount of HC [71].

Chemiluminescence analysers were used to measure the NO_x. They measure the NO by detecting the light emitted when it reacts with ozone (O_3):

$$NO + O_3 \Rightarrow NO_2^* + O_2 \Rightarrow NO_2 + O_2 + h\nu \tag{3.2}$$

The intensity of the light, $h\nu$, proportional to the amount of NO in the sample gas, is measured and converted to an electrical signal. Other oxides of nitrogen are measured by passing them through a converter located before the reaction chamber that changes any NO_2, NO_3 and so forth into NO [70].

Particles concentration was measured by the AVL Smoke Meter whose main characteristics are shown in Table 3.4. Particles consist principally of combustion generated carbonaceous materials (soot) on which some organic compounds have become absorbed. The AVL Smoke uses a pump to draw a raw sample of exhaust gas through a filter paper. The blackening of the filter paper is measured with a reflectometer and indicates the soot content in the exhaust gas. A value of 10 is assigned to a filter paper with no reflection and a value of 0 is assigned to a clean filter paper [70]. It was shown, that the Filter Smoke Number (FSN), measured with the Smoke Meter, represents the carbon (C) part of the particles. This is expressed through the empirical equation [72]:

$$C[mg/m^3] = \frac{1}{0.405} \cdot 4.95 \cdot FSN \cdot \exp(0.38 \cdot FSN) \tag{3.3}$$

Table 3.4. Smoke Meter Specifications [72].

Instrumentation	AVL Smoke Meter
Measurement range	0-10 FSN; 0-32000 mg/m^3
Resolution	0.001 FSN; 10 µg/m^3
Low detection limit	0.002 FSN; 20 µg/m^3
Repeatability	$\sigma \leq \pm 0.005$ FSN^2+3% of the measurement value
Reproducibility	$\sigma \leq \pm 0.005$ FSN^2+6% of the measurement value

The Horiba MEXA 7100 DEGR provides the gas emissions in ppm or % unit while the AVL Smoke Meter gives the PM in mg/m^3. The emission values were converted in *g/kg$_f$* by means of the air and fuel flow method [73]. Moreover, the knowledge of the engine bsfc allowed to express the emissions in g/kWh. This procedure was explained in detail in APPENDIX A

The sizing and the counting of the particles were performed in the size range from 5.6 to 560 nm by means of the Engine Exhaust Particle Sizer^{TM} (EEPS) spectrometer developed by TSI (Table 3.5). The instrument draws a sample of the exhaust flow into the inlet continuously. Particles are positively charged to a predictable level using a corona charger. Charged particles are then introduced to the measurement region toward the center of a high-voltage electrode column. A positive voltage is applied to the electrode and creates an electric field that repels the positively charged particles outward according to their electrical mobility. Charged particles strike the respective electrometers and transfer their charge. A particle with higher electrical mobility strikes an electrometer at the top; whereas, a particle with lower electrical mobility strikes an electrometer lower in the stack. The time response of the EEPS is approximately 100 ms [74].

Before entering the EEPS, the sample of exhaust gas is taken by a heated line of 1.5 m and diluted by means of the Dekati Engine Exhaust Diluter (DEED), a Particle Measurement Programme (PMP)-compliant conditioning system. In the DEED, the sample is first diluted with air heated above 150°C. Then the sample passes through an evaporation chamber at a temperature above 300°C for removing volatile particles. Any particles that remain in the aerosol after this point are considered to be solid particles [75]. After the thermal conditioning, the sample is further diluted to reduce the particle concentration along with the temperature to a suitable level for the size distribution measurement [76].

Table 3.5. EEPS specifications [74].

Particle Size Range	5.6 to 560 nm
Particle Size Resolution	16 channels per decade (32 total)
Electrometer Channels	22
Charger Mode of Operation	Unipolar diffusion charger
Inlet Cyclone 50% Cutpoint	1 µm
Time resolution	10 size distributions/sec
Inlet Aerosol Temperature	10 to 52°C

3.2 Tested fuels

Tests were performed with commercial diesel fuel and with pure and blended biodiesel. Biodiesel is defined as "a fuel comprised of mono-alkyl esters of long chain fatty acids derived from vegetable oils or animal fats" [77]. Biodiesel comes from the transesterification process of oils with an alcohol (methanol or ethanol) in the presence of a catalyst. The products are fatty acid methyl esters (FAME) or ethyl esters (FAEE) consisting of straight saturated and unsaturated hydrocarbon chain and glycerine [78]. The basic biodiesel reaction is shown in Figure 3.5. In particular, rapeseed methyl ester (RME) is made through a reaction of rape seed oil and methanol.

In the present research activity, a blend of 20% v/v RME with diesel fuel (B20), a blend of 50% v/v RME (B50) and lastly, pure RME (B100) were tested. Table 3.6 shows the main fuels properties obtained by laboratory analysis. The chemical composition of biodiesel is different from diesel fuel, having less carbon and more oxygen. The different chemical structure and higher molecular weight of RME result in higher density and viscosity of the biodiesel leading to a worsened fuel atomization [79]. RME has cetane number (CN) 10% higher than diesel fuel resulting in an advanced combustion [80]. Biodiesel has lower LHV than diesel fuel resulting in less torque for a given injector pulse width; the lower energy content per mass also results in higher bsfc [31]. Biodiesel has improved lubrication characteristics with respect to diesel fuel but they could contribute to the formation of deposits, plugging of filters depending mainly on degradability, glycerol content and cold fuel properties [81]. Moreover, RME has the distillation curve that stretches in the temperature range corresponding to the tail of the diesel fuel. The usually lower final boiling point of biodiesel, despite its higher average distillation temperature, provides lower probability of soot being formed from heavy hydrocarbon fractions unable to vaporize [23].
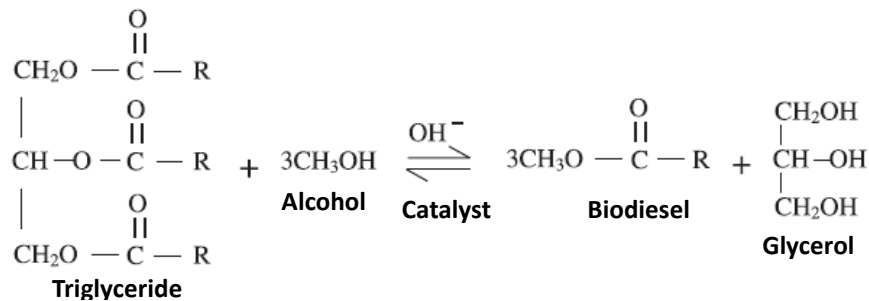

Figure 3.5. Transesterification reaction.

Table 3.6. Fuels properties.

Properties	Method	Diesel	B20	B50	B100
Density @ 15°C [kg/m^3]	ASTM D4052	834.4	844.9	860.6	886.8
Viscosity @ 40°C [mm^2/s]	ASTM D445	2.69	3.16	3.87	5.04
Cetane Number	ISO 5165	51.8	52.8	54.4	57.0
Low Heating Value [MJ/kg]	ASTM D240	42.9	41.9	40.5	38.1
Cold Filter Plugging Point [°C]	EN 116	-11.00	-1.2	13.6	38.10
Lubricity @ 60°C [μm]	IP 450	220	176	110	-1
Carbon [%, m/m]	ASTM D5291	86.3	84.4	81.6	76.9
Hydrogen [%, m/m]	ASTM D5291	12.7	12.5	12.2	11.7
Oxygen [%, m/m]	ASTM D5291	0.9	2.9	5.9	10.8
Nitrogen [%, m/m]	ASTM D5291	< 0.1			0.6
C/H ratio	ASTM D5291	6.80	6.8	6.7	6.57
Sulphur [mg/kg]	UNI EN ISO 20846	7.00			< 3
Distillation [°C]:	ASTM D86				
Initial boiling point [°C]		173.9	187.1	207.0	240.0
10 %vol [°C]		204.7	227.8	262.4	320.0
50 %vol [°C]		262.0	276.0	296.9	331.8
90 %vol [°C]		334.9	335.2	335.7	336.5
95 %vol [°C]		349.6	347.7	344.8	340.0
Final boiling point [°C]		360.4	356.5	350.8	341.1

3.3 Operating conditions

Before starting the tests the engine was heated up until the coolant water reached 80°C. Tests with blended and pure biodiesel were carried out without any hardware and engine management system modification. Injection strategies consisted of two injections per cycle, a pilot and a main. Tests were performed at different engine speeds, from 1400 to 3600 rpm with a step of 200 rpm, at full and medium load. Optical investigations were performed in the operating conditions at 1400, 2000 3400 rpm, medium and full load. The conditions and 2000 and 3400 rpm, full load are representative of the maximum torque and power, respectively.

Table 3.7 shows the brake torque output (T_b) and the bsfc for all the fuels in the test points at 1400, 2000 and 3400 rpm, at both full and medium load. The pressure, humidity and temperature of the ambient air inducted into an engine affect the air mass flow rate and the power output. Therefore ambient conditions were monitored during the tests and correction factors were used to adjust measured torque output to standard atmospheric conditions in order

to provide a more accurate basis for comparison between engine tests [57]. It is worth underling that at full load, the ECU set the same injection strategies for all the tested fuels and deactivated the EGR. Lower torque and higher bsfc were measured for blended and pure biodiesel because of the lower LHV, as it can be observed in Table 3.7. At medium load, the accelerator pedal throttle position was changed to set, for all the fuels, the test point corresponding to the 50% of the diesel maximum torque at fixed engine speed. In these conditions, the ECU changed the injection strategies and the EGR level for the tested fuels. Figure 3.6 shows the EGR percentage set by the ECU; it was assessed by measuring the CO_2 recirculated at intake, according to the following formula:

$$EGR = \frac{CO_{2,\text{int}}}{CO_{2,ex}} \cdot 100\% \tag{3.4}$$

Table 3.7. T_b and bsfc at 1400, 2000 and 3400 rpm, full and medium load, for the tested fuels.

Speed	Fuel	full load		medium load	
		T_b	bsfc	T_b	bsfc
[rpm]		[Nm]	[g/kWh]	[Nm]	[g/kWh]
1400	diesel	51.9	238.1	26.0	259.5
	B20	49.5	245.7		261.2
	B50	43.7	274.6		313.5
	B100	41.5	294.3		328.0
2000	diesel	59.0	238.8	29.0	262.2
	B20	57.1	256.1		265.8
	B50	53.6	267.3		295.9
	B100	52.4	275.7		308.6
3600	diesel	43.9	257.8	22.0	308.4
	B20	43.8	255.7		324.4
	B50	43.0	283.5		336.4
	B100	42.0	295.9		360.5
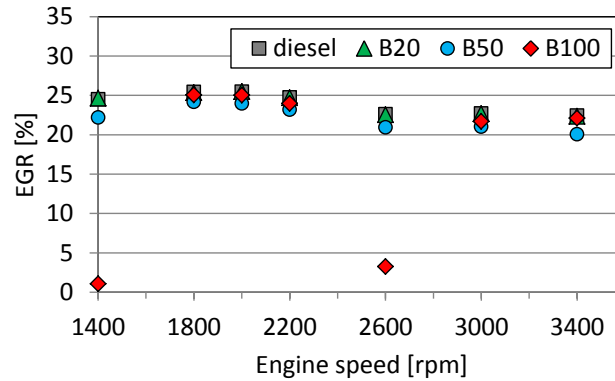
Figure 3.6. EGR percentage for diesel fuel, B20, B50 and B100 at medium load conditions.

3.4 Uncertainty analysis

In any experiment, errors and uncertainties can arise from instrument selection, condition, calibration, environment, observation reading and test procedure. Uncertainty analysis is needed to prove the accuracy of the experiments [82]. Standard deviation is a statistical indicator to describe errors. The error is thus derived using the standard deviation from the mean. For each test point, experimental data were detected for three repetitions and results displayed graphically with ± standard error of average value. Similar conditions were maintained for all the tests for better comparison of the results.

Chapter 4

Experimental results

4   Experimental results

4.1   Energy analysis

Energy distribution and waste heat energy characteristics of the engine were studied by combining the methods of energy and exergy analysis. First of all, the combustion efficiency, η_{comb}, was evaluated when the engine ran with diesel and with blended and pure biodiesel. It is known that during the combustion process, not all the fuel molecules combine and react with the oxygen because of a not good mixing, local variations in temperature and low level of turbulence. Consequently, a small fraction of fuel does not react and exits with the exhaust flow. In a CI engine the air utilization is limited by the onset of black smoke that, together with incomplete combustion products such as HC and CO, represents a combustion inefficiency [57].
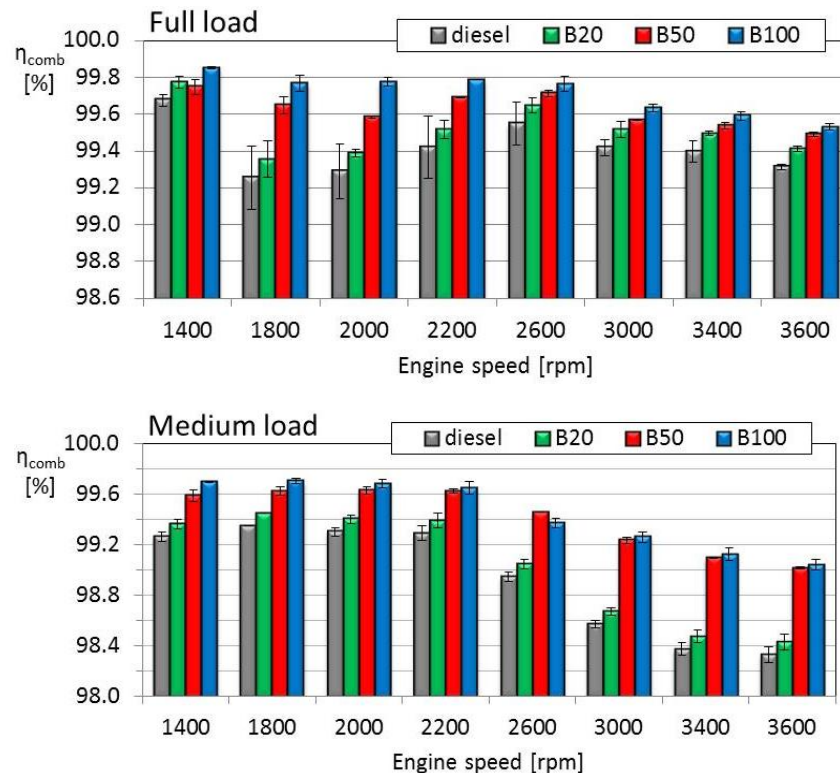

Figure 4.1. Combustion efficiency for all the tested fuels at different engine speeds and at full (up) and medium load (down).

In order to evaluate the completeness of combustion, η_{comb} is evaluated according to the Equation 2.4. For CI engines, it is greater than 98% [57] as confirmed also by Figure 4.1 that shows η_{comb} assessed for all the tested fuels in the investigated operating conditions. It can be observed that η_{comb} has lower values at medium load with respect to the full load conditions because of the EGR presence that worsens the combustion process. Regarding the effect of fuel, η_{comb} increases with the RME content because of the structural oxygen content of the biodiesel molecules that improve the homogenization of oxygen with the fuel during the combustion [83]. The improved combustion provided by biodiesel results in lower concentration of CO, HC and PM, as confirmed by exhaust measurements presented in the next section, and in lower exhaust gas temperature.

The heat supplied to ICE by the fuel combustion is in part converted into useful mechanical work and the remaining part is lost in the form of exhaust gas, cooling water and other types of losses. The waste heat recovery could be a useful mean to improve the engine thermal efficiency, reducing the fuel consumption and pollutant emissions.

Exhaust gas energy is the most attractive among the waste heat sources because of the temperature at which this heat flow is available. Nevertheless, it is not possible to exploit all the energy content of the exhaust gas when the engine runs with fuels containing sulphur. The limiting factor is the temperature at which the heat exchanger surfaces reach a point where both combustion product acids and water precipitate on the metal surfaces causing corrosion.
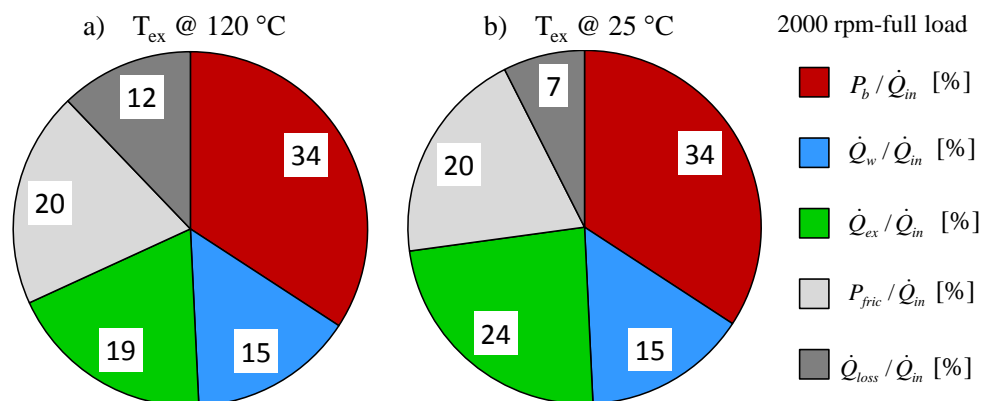

Figure 4.2. Flow energy diagram for diesel fuel at 2000 rpm, full load: a) exhaust gas cooled down to 120°C; b) exhaust gas cooled down to 25°C.

The acid dew point is a function of the amount of sulphur in the fuel and, subsequently, in the exhaust gas [84]. Therefore, exhaust gas can be cooled down to 120°C to avoid the formation of acid condensations. In order to appreciate the loss of exhaust gas heat rate, $\dot{Q}_{ex}$, resulting when exhaust gas are cooled down to 120°C, rather than to the ambient temperature (25°C), the energy flows of the engine were calculated in both cases, as shown in Figure 4.2. In the second one, the condensed mass flow rate of water in the exhaust gas was calculated from the equation of the combustion reaction [57] and the c_p of the condensed water was considered. This comparison was performed in the engine point at 2000 rpm-full load, representative of the maximum torque condition (Table 3.1). The flow energy diagrams show that about one-third of the fuel input heat rate is converted in brake power output. The cooling water heat rate, $\dot{Q}_w$, is about the 15% of the fuel heat rate, $\dot{Q}_{in}$. The ratio $\dot{Q}_{ex}/\dot{Q}_{in}$ changes from 19 to 24% as the temperature varies from 120 to 25°C. Therefore, the total losses (the sum of friction losses and minor thermal losses) decrease of about 15% when exhaust gas are cooled down to the ambient temperature.

In order to take into account the issue of acid condensations, the data on energy flows that will be presented in this thesis where calculated by assuming to cool exhaust gas down to 120°C, for all the tested fuels; Table 3.6 shows, in fact, that also biodiesel contains sulphur, even if to a lesser extent than diesel fuel.

Figure 4.3 shows the energy distribution of the engine for diesel fuelling. The graphs represent the maps of the brake power (Figure 4.3a), the exhaust gas heat rate (Figure 4.3b) and the cooling water heat rate (Figure 4.3c). All the energy flows are expressed in percentage of the fuel heat rate and they are represented as function of the imep and the engine speed by means of a contour-plot type map. The data were interpolated using a triangle-based cubic model over a uniform grid of speed and load points. The graphs reveal how the speed and the load influence the engine energy distribution.

Figure 4.3a shows the percentage of the brake power, P_b, in fuel heat rate input that is representative of the fuel conversion efficiency, η_f (Equation 2.14). It is clear that a better exploitation of the fuel is reached at high loads because of the lower friction losses. The maximum $P_b/\dot{Q}_{in}$ value is 34% and it is reached at 2000 rpm and about 11 bar of imep.
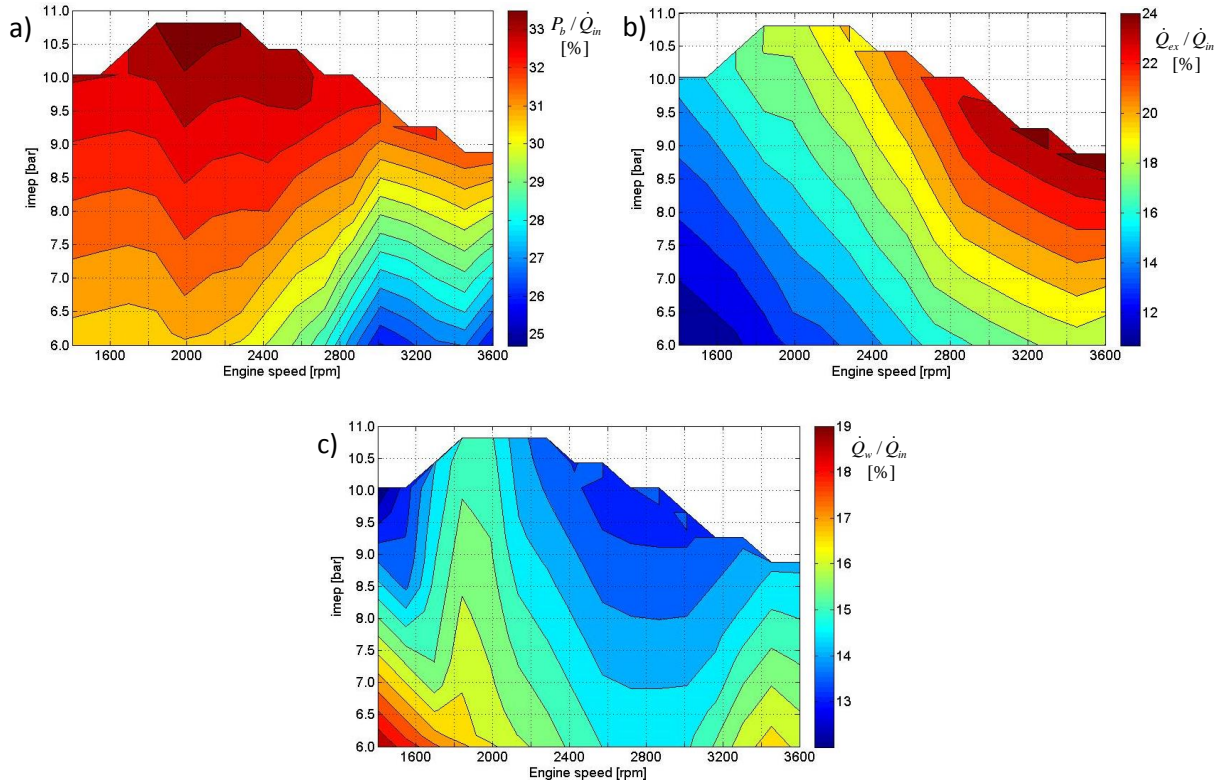
Figure 4.3. Energy distribution under mapping conditions for diesel fuel: a) $P_b / \dot{Q}_{in}$, b) $\dot{Q}_{ex} / \dot{Q}_{in}$, c) $\dot{Q}_w / \dot{Q}_{in}$.

Figure 4.3b shows that exhaust gas contains a lot of energy that can be used as a new energy source. The term $\dot{Q}_{ex} / \dot{Q}_{in}$ is more sensitive to the engine speed than the load: it increases with the speed under most of the operating conditions. At engine speeds lower than 2000 rpm, $\dot{Q}_{ex} / \dot{Q}_{in}$ has values below 15%; the maximum value (about 24%) is reached at 3400 and 3600 rpm full load. This trend can be explained as follows: as the engine speed increases, the combustion is faster and the time for heat transfer from the combustion products to the surrounding is reduced, causing lower heat losses. Therefore, more fuel energy flows to the exhaust gas resulting in higher temperature at exhaust and, hence, higher waste heat recovery potentiality.

Figure 4.3c reveals that an important quantity of waste heat is carried away by the coolant system. It can be observed that the load mainly affects the cooling water heat rate. The general trend is that $\dot{Q}_w / \dot{Q}_{in}$ increases as the load decreases. The reason is that the percentage of fuel energy converted into effective work decreases at low load; consequently, the most of the fuel energy is converted into friction and heat transfer losses that are taken away by the cooling water. The highest $\dot{Q}_w / \dot{Q}_{in}$ is about 20% and it is detected at low load and in particular at low

speed. The reason is that the heat losses depend on both the transfer time and in-cylinder temperature: when the engine speed increases, the in-cylinder temperature increases but the transfer time decreases, therefore, $\dot{Q}_w / \dot{Q}_{in}$ decreases as the engine speed increases because of the lower heat losses.

Figure 4.3 shows that the operating condition area of the highest $P_b / \dot{Q}_{in}$ is inconsistent with that of the highest $\dot{Q}_{ex} / \dot{Q}_{in}$ and $\dot{Q}_w / \dot{Q}_{in}$. In order to take into account the improvement of the engine efficiency resulting by the waste heat energy recovery, the first law efficiency, η_I, of the cogeneration system based on the engine under investigation has been calculated according to the Equation 2.1. It is worthy underling that for the electrical power calculation (Equation 2.2) the efficiency of the electric generator was assumed equal to 0.9 [9, 10]. Figure 4.4 shows η_I calculated for diesel fuel under mapping condition. First of all, it can be observed that η_I is two times higher than η_f (Figure 4.3a). From the viewpoint of improving the engine total fuel efficiency by waste heat recovery, the optimal operating condition area is located at high-speed and high load which is different from the optimal operating condition area for η_f (2000 rpm, full load). High values of η_I, about 60%, are detected at 2000 rpm full load in agreement with η_f trend; however, the highest η_I values are reached at high engine speed (from 3200 to 3600 rpm) full load, in disagreement with η_f, because of the high energy recovery from the exhaust gas.
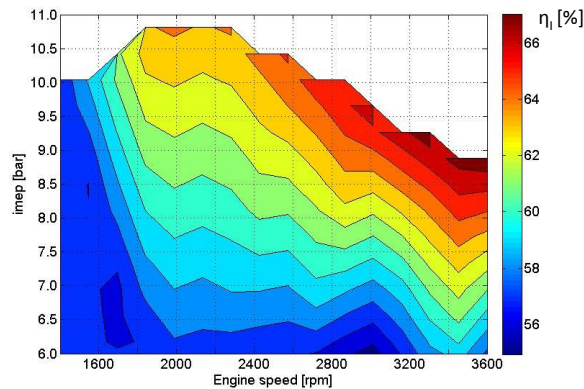
Figure 4.4. η_I under mapping conditions for diesel fuel.

In order to investigate the effects of both blended and pure biodiesel on the engine energy distribution, the energy flows of diesel, B20, B50 and B100 were compared at different engine speeds, at medium and full load, as shown in Figure 4.5.
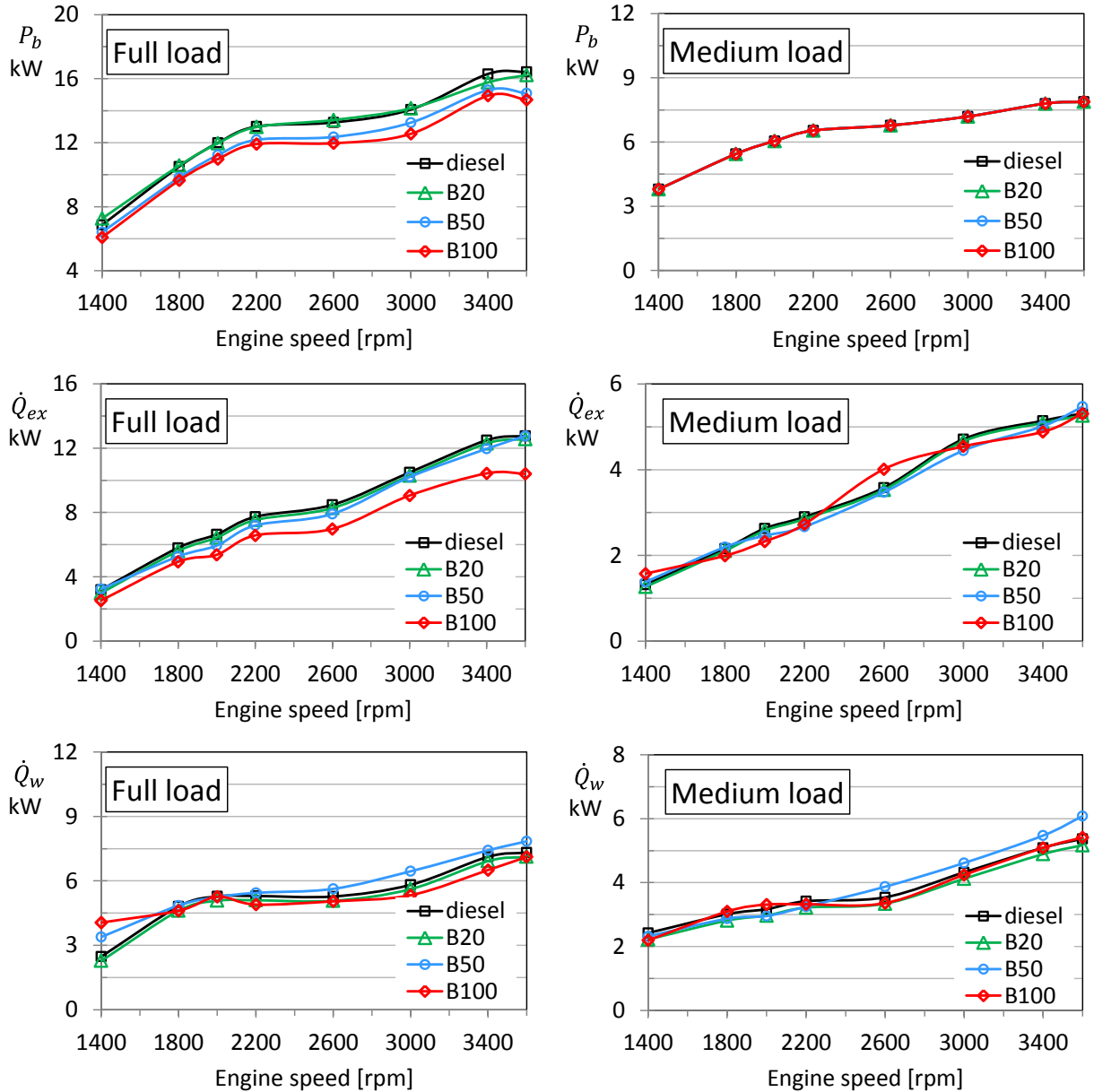
Figure 4.5. Energy flows (P_b , $\dot{Q}_{ex}$, $\dot{Q}_w$) for all the tested fuels, at different engine speeds and at full (left) and medium load (right).

At full load conditions, P_b varies from 6 to 16 kW as the engine speed changes from 1400 to 3600 rpm, for diesel fuel. As mentioned in the previous section, at full load conditions the injected quantity of fuel was the same for all the fuels and so a reduction of the power output

is detected for blended and pure RME because of the lower LHV of biodiesel. By way of example, at 3600 rpm full load, a 12% reduction of P_b is observed for B100 with respect to diesel fuel. At medium load conditions, the injection strategies were changed to reach the same power output for all the fuels and it ranges between 4 and 8 kW.

Concerning $\dot{Q}_{ex}$, at full load, it increases with the engine speed from 3 to 12 kW, for diesel fuel. At medium load conditions, lower values of $\dot{Q}_{ex}$, between 1 and 5 kW, are detected for diesel fuel. Moreover, it can be observed that the heat rate recovered by exhaust gas decreases as the content of biodiesel increases because of the lower exit temperature of exhaust gas for biodiesel with respect to diesel fuel.

The lower LHV of biodiesel, in fact, reduces the total energy released from combustion process and, hence, reduces the exhaust gas temperature. Lower $\dot{Q}_{ex}$ for RME is observed at almost all the operating conditions except for the test point at 1400 and 2600 rpm medium load. In these cases, in fact, the ECU deactivates the EGR for pure RME in order to reach the same power output of diesel fuel (Figure 3.6). Consequently, larger amount of exhaust gas is available at exhaust resulting in higher value of $\dot{Q}_{ex}$ with respect to diesel fuel.

$\dot{Q}_w$ of diesel fuel ranges between 2.5 and 7 kW at full load, meanwhile, lower values, in the range 2.5-5 kW are detected at medium load conditions. Regarding the effect of fuel on $\dot{Q}_w$, it can be observed in Figure 4.5 that there is not a definite trend of $\dot{Q}_w$ among the tested fuels.

It is worthy underling that the heat produced by a cogeneration plant could be also used to generate chilled water, for air conditioning or refrigeration. For this purpose, absorption chillers could be linked to the CHP unit. By way of example, the heat rate of exhaust gas in the operating condition at 2000 rpm full load, for diesel fuel, could provide a power of about 4 kW for cooling applications.

Figure 4.3-Figure 4.5 report the quantity of various kinds of waste heat energy. According to the second law of thermodynamics, the evaluation indicator of energy is not only the quantity but also the quality. From this point of view, exergy analysis is more useful to evaluate the waste heat energy characteristics. Therefore, waste heat energy has been studied by using the method of exergy analysis with the aim of revealing its recovery potentiality.
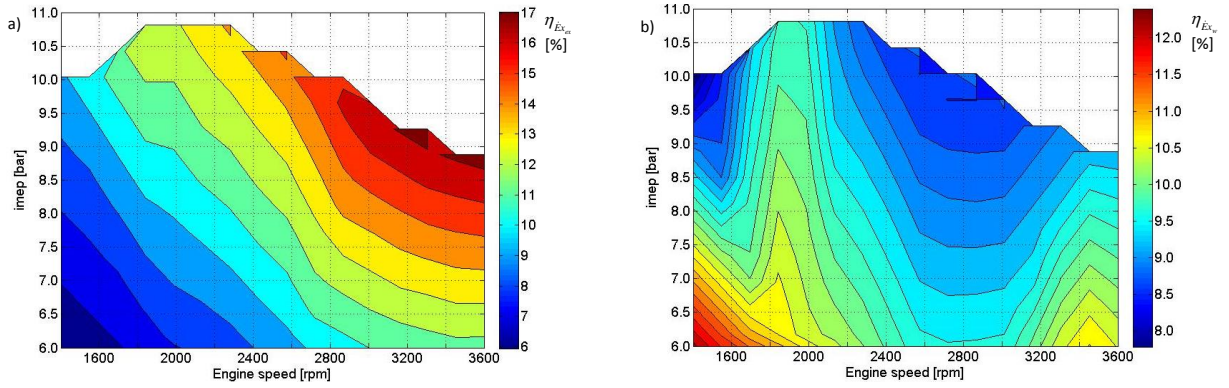
Figure 4.6. a) $\eta_{\dot{E}x_{ex}}$ and b) $\eta_{\dot{E}x_{w}}$ under mapping conditions for diesel fuel.

Figure 4.6 shows the exergy efficiency of the exhaust gas, $\eta_{\dot{E}x_{ex}}$, and of the engine cooling water, $\eta_{\dot{E}x_{w}}$, at different operating conditions, for all the fuels investigated. It can be observed that $\eta_{\dot{E}x_{ex}}$ is more sensitive to the speed, which is consistent with the distribution regularity of exhaust gas energy percentage (Figure 4.3b). The highest $\eta_{\dot{E}x_{ex}}$ is about 17% and it occurs at high speed and high load. Being different from exhaust gas exergy efficiency, the cooling water exergy efficiency is more sensitive to the load. The highest $\eta_{\dot{E}x_{w}}$ value is about 12% and it is detected in the low speed and low load area.

The differences in energy and, in particular, in exergy characteristics between exhaust gas and cooling water are mainly due to the temperature at which these energy flows are available. The exhaust gas temperature, in fact, ranges between 250 and 500°C depending on the operating condition and the highest temperature is detected at high speed and high load. On the other hand, the temperature of cooling water is constant at 80°C.

In order to investigate the opportunity of a cogeneration system with the engine under investigation, exergy analysis was performed through the second law efficiency, η_{II}, calculation (Equation 2.5). Figure 4.7 shows the η_{II} detected for diesel fuel under mapping characteristics. The trend is similar to that one of η_{I}; highest values, in fact, is detected at high speed and high load. However, the highest value of η_{II} is about 20% lower than the highest η_{I} since, although the LHV and exergy content of the fuel, ex_f, are approximately equivalent, the exergy outputs are smaller than energy outputs.
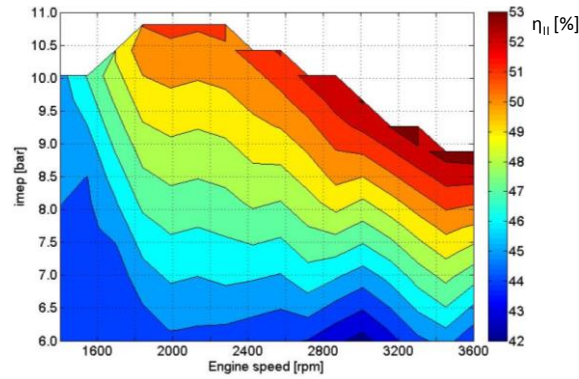
Figure 4.7. η_{II} under mapping conditions for diesel fuel.

The exergy analysis has been carried out for all the tested fuel as shown in Figure 4.8. The exergy rate of exhaust gas, $\dot{Ex}_{ex}$, for diesel fuel changes between 2 and 9 kW when the speed varies from 1400 to 3600 rpm, at full load. Lower values, between 1 and 3.5 KW, are detected at medium load. It can be observed that the exergy of exhaust gas decreases as the content of biodiesel increases because of the lower exhaust gas temperature. This trend is not valid in the test points at 1400 and 2600 rpm as previously mentioned for the Figure 4.5.

Figure 4.8. Exergy content of exhaust gas and cooling water for all the tested fuels, at different engine speeds and at full (left) and medium load (right).

The exergy rate of cooling water, $\dot{Ex}_w$, has values between 2 and 5 kW at full load, meanwhile, at medium load it ranges between 2 and 4 kW. It is not possible to identify a definite trend of $\dot{Ex}_w$ with the fuel properties.

4.2   Indicating data

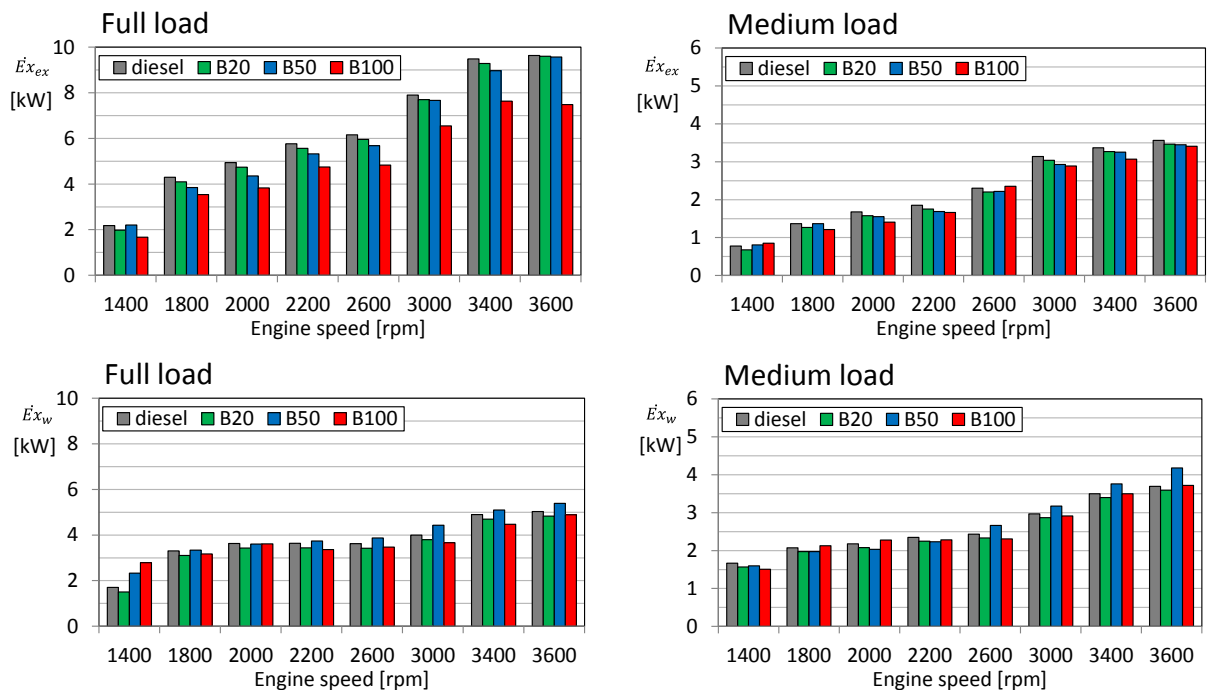The in-cylinder pressure measurement is an effective tool to analyse the engine behaviour since the pressure history directly influences the power output and the engine out emissions. The pressure data allow to calculate the ROHR evolution by means of the perfect gas law and the first law of thermodynamics [57]. Figure 4.9 shows the in-cylinder pressure and the ROHR curves of all tested fuels over the end of compression and the early expansion stroke at 1400, 2000 and 3400 rpm, full and medium load. The curves refer to the first cylinder, however, indicating data of the third one were also investigated and they showed similar trend. As mentioned in the section 3.3, in the full load conditions the injected fuel quantities are the same for all the fuels and the EGR is deactivated; hence, the differences in combustion evolution can be ascribed just to the different fuels properties. At medium load conditions, instead, the indicating data profiles are affected not only by the fuel properties but also by the engine test point and, in particular, by the EGR.

Pressure traces exhibit two peaks: the first one, centred on the TDC, due to the pilot combustion and the second one, more pronounced, due to the main combustion. At 1400 and 2000 rpm full load, diesel fuel has higher pressure peak and pressure traces during the expansion stroke with respect to blended and pure biodiesel. In particular, pressure signal decreases with the content of biodiesel in the fuel because of the lower LHV. At 3400 rpm full load, the main pressure peak is more advanced as higher the biodiesel content because of the higher CN. At 1400 rpm medium load, B20 and B50 show lower pressure than diesel fuel while B100 reaches pressure peak similar to diesel as consequence of the absence of EGR (Figure 3.6).At 2000 rpm medium load, the pressure evolution shows similar behaviour for diesel and B20, while B50 and B100 have more advanced and higher pressure: in presence of EGR the higher CN of biodiesel plays an important role on the fuel ignition. At 3400 rpm medium load, the pressure peak is more advanced as higher the biodiesel content; in particular, the effect of higher CN of biodiesel is more remarked for biodiesel blend higher than 20% v/v.
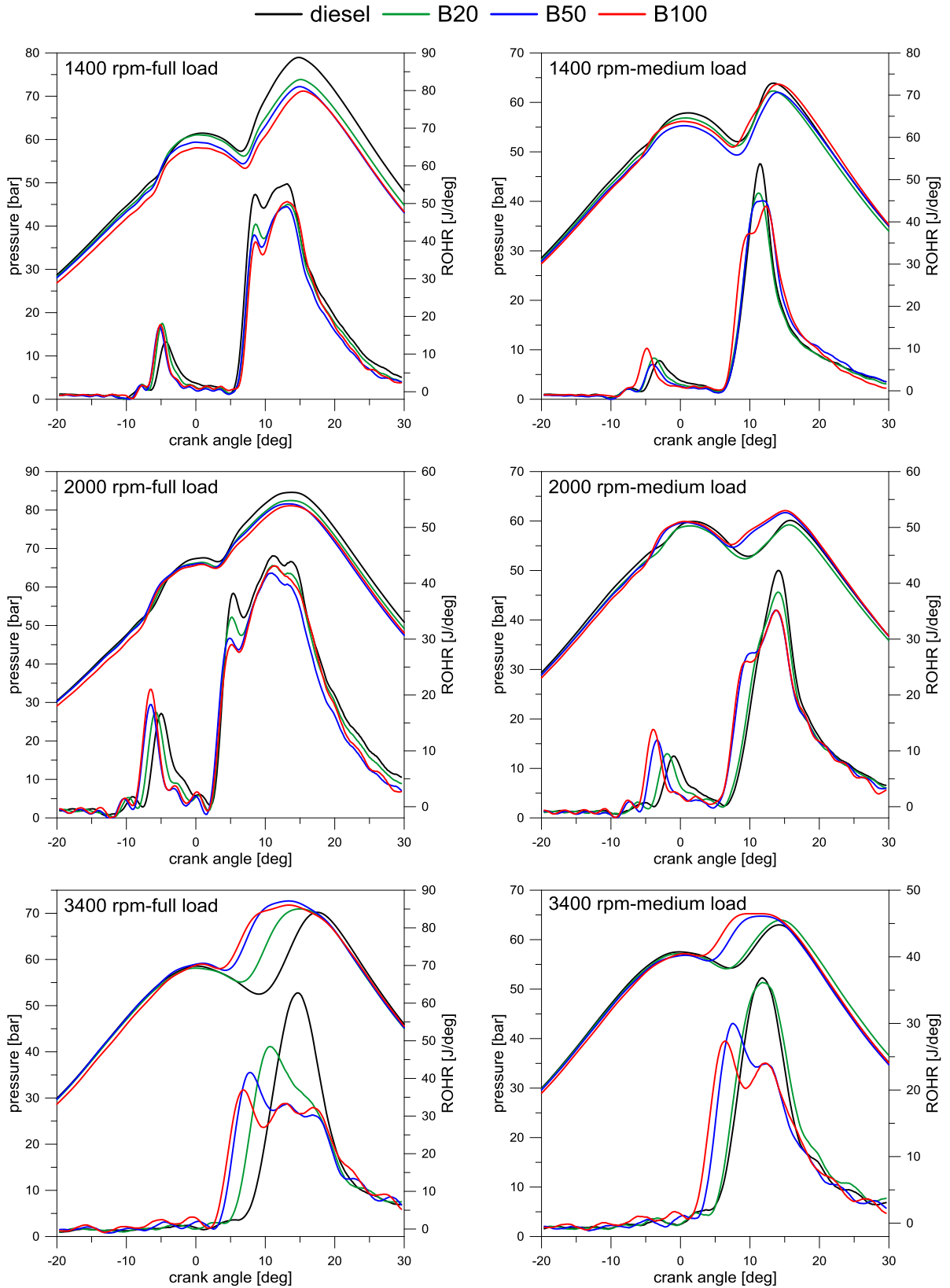
Figure 4.9. In-cylinder pressure measurements and ROHR for all the tested fuels at 1400, 2000 and 3400 rpm, at full (left) and medium load (right).

Looking at the ROHR curves, two well-defined peaks are observed at 1400 and 2000 rpm at both full and medium load; they are due to the combustion of the pilot and main injections. At 3400 rpm, full and medium load, the pilot combustion is not distinguishable because of the lower amount of fuel injected at high engine speed due to the lower time available for the combustion process. At 1400 and 2000 rpm full load, the heat released by the pilot combustion is more advanced as higher the RME content. The heat released by diesel pilot combustion is higher due to the higher LHV. Therefore, the in-cylinder temperature at the time of diesel main injection is higher with respect to the other fuels. The higher in-cylinder temperature allows to overcome the fuel characteristics of RME, mainly the higher CN, and so the main combustion starts at same time for all the fuels. ROHR traces of the main combustion show a similar trend for all the fuels: they are characterized by a first fast rate of premixed phase followed by a diffusive tail. The peak of heat released decreases with the RME percentage because of the lower LHV. A different behaviour is observed at 3400 rpm full load: the addition of RME to diesel fuel results in more advanced combustion and lower heat released. Moreover, for diesel fuel the combustion develops mainly in premixed mode while blended and pure biodiesel combustion occurs in premixed and diffusive way. The longer diffusive phase with biodiesel, in this test point, can be ascribed to the fuel properties. At high engine speed, in fact, the high density and viscosity of RME could lead to large droplet formation and, hence, poor fuel air mixing, resulting in longer combustion duration. These considerations will be confirmed by optical investigation shown in the section 4.3. At 1400 rpm medium load, the combustion evolution has a similar behaviour for diesel fuel, B20 and B50. An advanced main combustion is detected for B100 due to the higher CN of RME coupled with the absence of EGR; moreover, B100 is characterized by a more lengthened diffusive tail. Also in this case, the heat released decreases with the RME content. At 2000 rpm, medium load the pilot combustion is more advanced as higher the RME percentage. Moreover, in presence of EGR, pilot combustion of blended and pure biodiesel is more efficient, thanks to the larger oxygen availability, and releases more heat than diesel fuel leading to high temperature in the chamber at the time of the main injection. This, together with the high CN of RME, results in advanced main combustion of B50 and B100 with respect to B20 and diesel fuel. Moreover, B50 and B100 show a more evident diffusive phase. Lastly, at 3400 medium load no significant differences are observed between diesel and B20 while

B50 and B100 are characterized by a more advance combustion characterized by lower peak and stronger diffusive phase.

The knowledge of the in-cylinder pressure allows to have information about the combustion noise that is the main source of noise for a CI engine. It is known from literature [17] that the in-cylinder pressure curve can be related to the Fourier Analysis (or spectrum) of the in-cylinder pressure. Figure 4.10 shows the combustion noise calculated from the pressure traces for the tested fuels at different operating conditions. Pressure signal was elaborated by AVL-Indicom software; it used an algorithm to calculate a power spectrum by means of a Fast Fourier Transform; then the power spectrum was filtered through the standardized structure transfer curve and the standard hearing curve (A-curve).
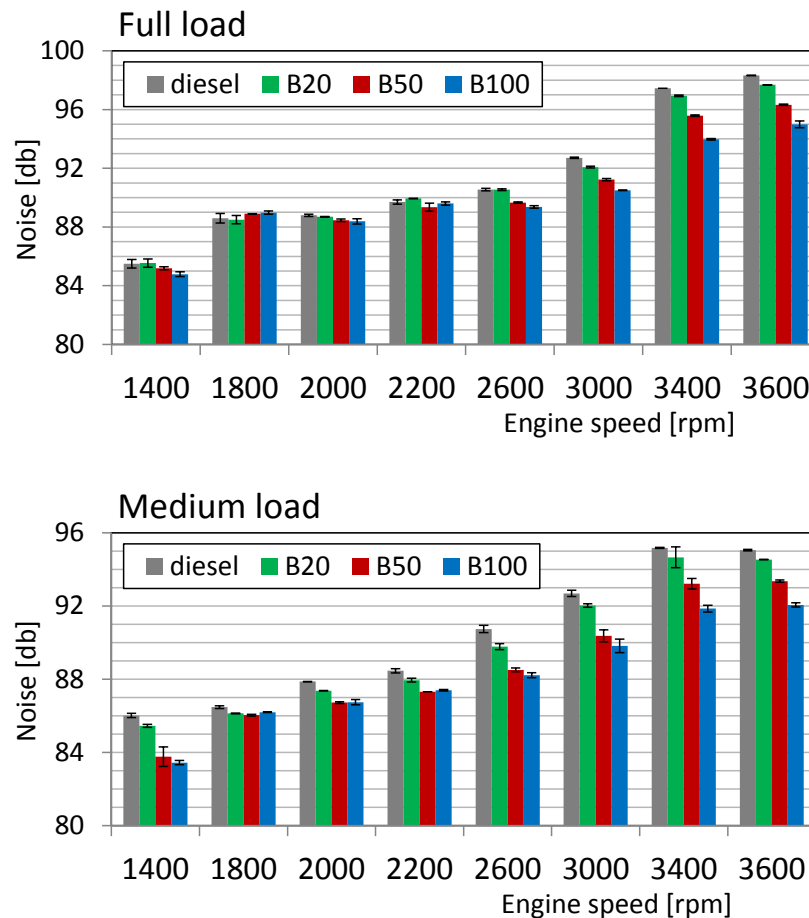

Figure 4.10. Combustion noise for all the tested fuels at different engine speeds, at full (up) and medium load (down).

It can be observed in Figure 4.10 that the combustion noise is affected by the engine operating condition: the noise, in fact, increases with the engine speed and load. Moreover, the combustion noise depends on the biodiesel content in the fuel. It can be observed that from 1400 to 2200 rpm blended and pure biodiesel emit slightly lower combustion noise than diesel fuel. The differences can be ascribed to the pressure evolution; at these engine speeds, in fact, pressure traces of the tested fuels have a similar beavhiour (Figure 4.9) but the pressure peak decreases with the biodiesel content also reducing the noise level. Larger differences in noise emissions between diesel and RME based fuels are detected at high engine speeds. Indicating data have shown that the effect of the higher CN of biodiesel is more evident at high engine speeds and, in fact, the pressure peak is more advanced as higher the RME content. Therefore, the ignition delay and, hence, the quantity of fuel that contributes to the premixed combustion is reduced for blended and pure biodiesel resulting also in lower combustion noise.

4.3   Optical investigation

ICEs rely on the conversion of chemical energy into mechanical power through combustion of fuel and air mixture in the cylinder. Optical investigation of combustion phase, combined with analyses of in-cylinder pressure data, represents a useful tool to optimize the combustion process for maximum power output, maximum efficiency and minimum pollutant emissions. Optical detection of combustion phase was an important object of this thesis work. Optical tests were performed with diesel fuel, B50 and B100. The operating conditions at 1400, 2000 and 3400 rpm, full and medium load, were selected for optical measurements. In particular, in the operating conditions at full load, the effect of the fuel properties on the jets distribution and the combustion evolution was investigated. At medium load, instead, also the effects of engine parameters, such as the EGR, were analysed.

Figure 4.11 shows a selection of images of combustion process in the angular range 6-26 cad ATDC , for the tested fuels, at 2000 rpm full load. Images where acquired with an exposure time of 83 µs corresponding to 1 cad.
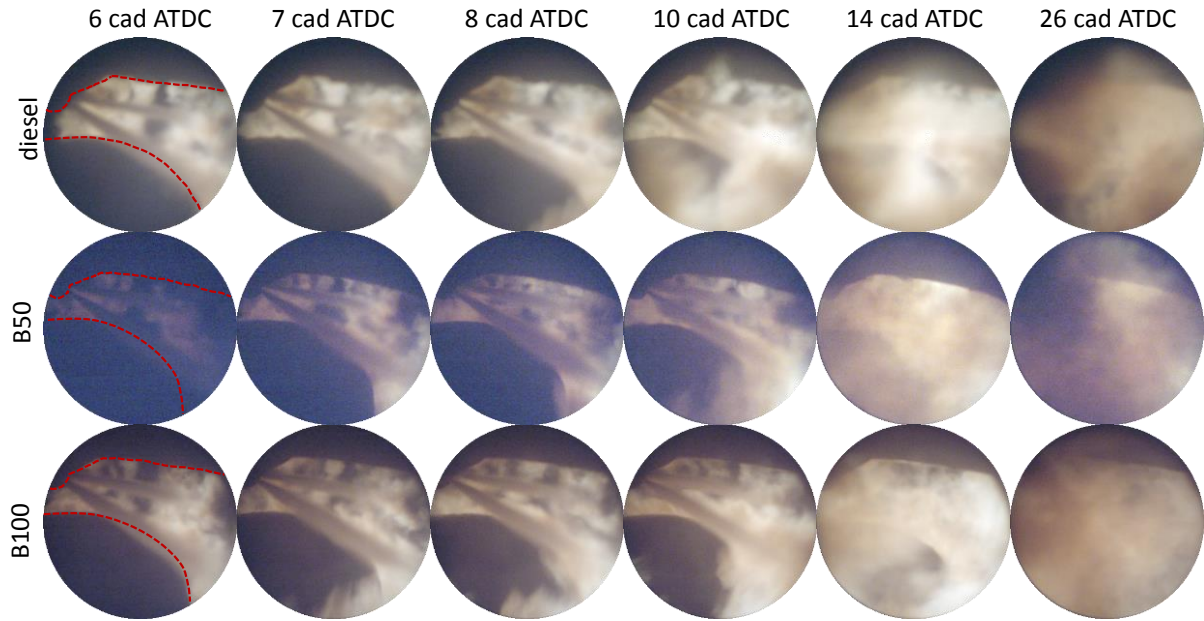
Figure 4.11. Images of combustion process for diesel fuel, B50 and B100 at 2000 rpm full load.

In the images, the jets of the pilot event are not visible since they are not lighted by any luminous source. The jets of the main event are visible in the optical field of view from 6 cad ATDC because illuminated by the pilot flames occurring in the bowl. The jets are visible up to 10 cad ATDC: they spread along the spray axis and impinge towards the bowl wall. In this angular range, some luminous flames are visible due to the fuel vapour that moves out the spray core and forms an ignitable fuel-air mixture in rich condition. From 8 cad ATDC, the flames rise from the bowl because of the air motions that guarantee the depletion of the impinged fuel. From 14 cad ATDC the flames spread out over the entire field of view and the burning high-temperature carbon particles provide very high luminosity appearing yellow-white. The brown region surrounding the white diffusion flames indicates an excessively rich mixture region where substantial soot production has occurred. When this fuel-rich soot-laden cloud contacts unburned air, there is a hot white diffusion flame. The combustion proceeds during the expansion stroke; at 26 cad ATDC the piston is positioned away from the TDC and, thus, the flames spread in the cylinder above the piston surface.

It can be observed that B50 and B100 combustion develops in the same way of diesel fuel but with lower luminous intensity. The flame emission intensity can be correlated to the soot concentration in the combustion chamber. The highest flame emissions are recognized as the

highest sooting flame thus diesel fuel is expected to have higher in-cylinder soot concentration than blended and pure RME.

In order to detect the effect of the fuel properties on the jets distributions, the length and cone angle were measured for the jet that is clearly distinguishable in the endoscopic field of view, as shown in Figure 4.11. The jet is isolated from the rest by masking the image. The jet length (L_{jet}) is measured as the distance from the exit hole up to the spray tip and, then, it is divided by a reference length (L_{ref}) that is the distance from the injector tip up to the optical limit of the endoscope, along the jet axis. The used optical setup does not allow to characterize the jets from the start up to the end of injection. The first jets are, in fact, visible when they are already developed since they are lighted by the combustion flames. Therefore, the jet characterization was performed just at one cad in order to detect the effect of the fuel on the spray when the combustion is ongoing.
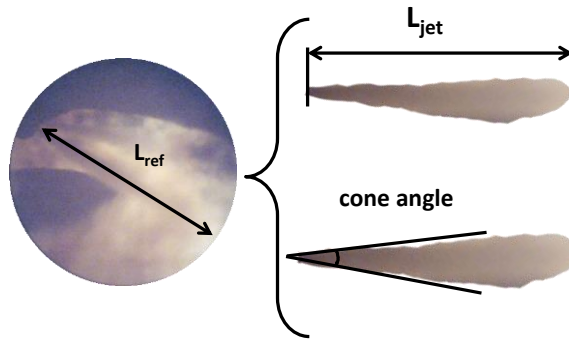

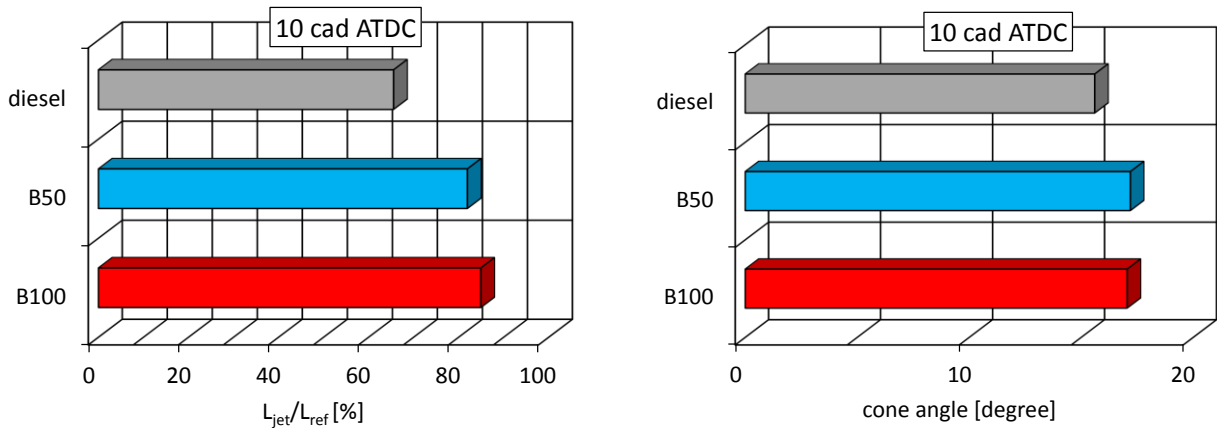Figure 4.12. Elaboration method for the jets analysis.

Figure 4.13. L_{jet}/L_{ref} and cone angle for diesel fuel, B50 and B100 at 2000 rpm full load, at 10 cad ATDC.

Figure 4.13 shows the ratio L_{jet}/L_{ref} and the cone angle of the jet at 10 cad ATDC, for all the tested fuels, in the operating condition at 2000 rpm full load. Blended and pure biodiesel show higher L_{jet}/L_{ref} and cone angle with respect to diesel fuel. Higher jet penetration with biodiesel was already found out in literature by numerical and experimental investigation in an injection test bed equipped with a glass injection chamber [85]. This behaviour can be ascribed to the higher viscosity and density of biodiesel (Table 3.6) that result in larger diameter of the fuel droplets. Since the inertia of the big droplets is higher, their penetration in the combustion chamber is higher. Although the poor atomization of biodiesel, the oxygen presence in biodiesel guarantees good fuel combustion as confirmed also by optical data of in-cylinder soot concentration.

The PM–NO_x trade off in diesel combustion is due to the fuel injection, air and EGR management and combustion chamber geometry. How the flame succeeds or fails in burning at desired temperature and with best utilisation of the available air is of central concern to combustion development. In this regard, to analyse the effect of the fuel properties and operating conditions on the combustion evolution and pollutant formation, flame images were post-processed by two-colour pyrometry method to quantify the flame temperature and the in-cylinder soot concentration that provide information about the two main exhaust emissions of a diesel engine, NO_x and PM, respectively. The two-colour method consists in the measurement of the radiation emitted at two wavelengths by the incandescent soot particles generated during the combustion process. Appropriate assumptions about the nature of the soot allow to estimate the instantaneous flame temperature and the soot concentration [86]. The theory of the two-colour pyrometry method is described in detail in APPENDIX A.
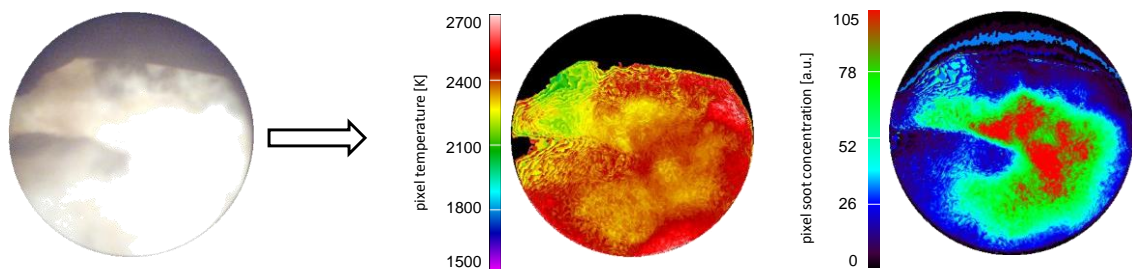

Figure 4.14. Post-processing of flame images.

Figure 4.14 shows a typical temperature and soot concentration distribution resulting from post processing of flame images. About temperature images, the color scale was set to 1500-

2700 K to allow the reading of the temperature gradients. For the same reason, the color scale of soot concentration was set to 0-105 arbitrary unit (a.u.). Each image includes 104.000 pixels; a pixel can be interpreted as a combustion chamber area of about 0.1x0.1 mm^2.
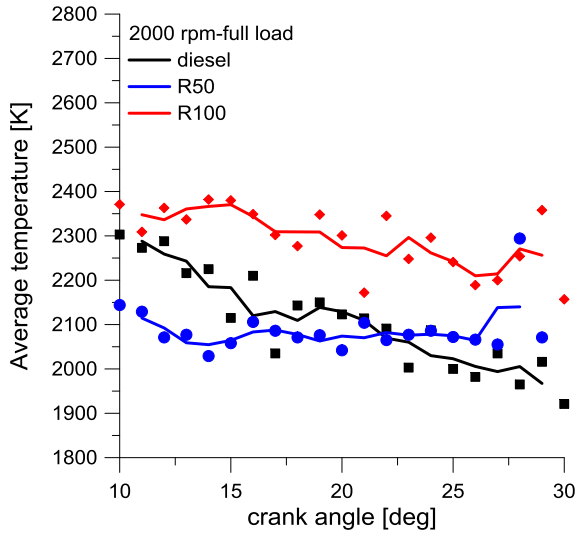

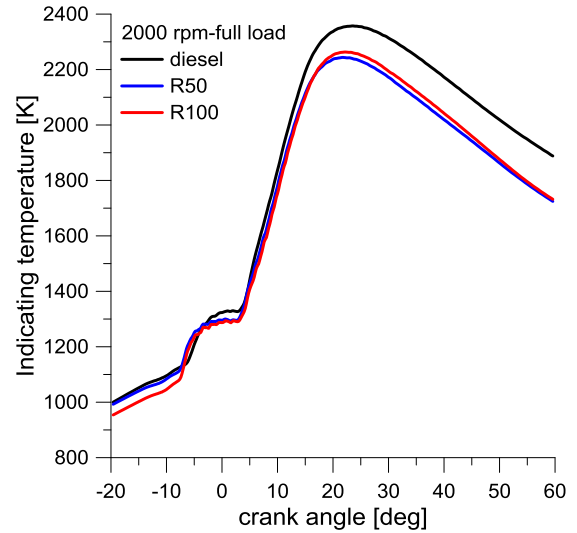Figure 4.15. Average flame temperature for diesel fuel, B50 and B100 at 2000 rpm full load.

Figure 4.16. Indicating temperature for diesel fuel, B50 and B100 at 2000 rpm full load.

Temperature images can be processed to calculate the average temperature during the combustion process, as shown in Figure 4.15 for the tested fuels in the operating condition at 2000 rpm full load; the symbols were obtained by averaging pixel-by-pixel the temperature map (Figure 4.14) and the black area, such as the one corresponding to the engine head, was excluded. Moreover, the interpolating curves of the average temperature data at each crank angle are also reported. It is worthy underling that optical measurements allow to have better insight of the local temperature distribution in the cylinder with respect to indicating temperature data. In this regard, Figure 4.16 shows the temperature calculated by the pressure signal for the tested fuels in the operating condition at 2000 rpm full load. It can be observed that diesel fuel has the highest temperature. An opposite behaviour is reported in Figure 4.15: B100 exhibits the highest flame temperature of about 2300 K; B50 has lower temperature than diesel fuel up to 22 cad ATDC and then it raises.

In order to have a more comprehensive knowledge of the local temperature distribution, for each image the number of pixel at fixed temperature was counted and it was normalized by the total number of pixels of the image in order to better investigate the flame temperature

distributions in the chamber. In this regard, Figure 4.17 and Figure 4.18 show the normalized pixel number at the temperature of 2000, 2400 and 2700 K, at full and medium load, respectively, for the tested fuels. It can be observed that the larger number of pixels is at temperatures over 2000 K that are responsible of the thermal NO_x reactions (Equation 2.19-Equation 2.21). As regards the effect of the fuels on the flame temperature distribution, it can be observed that at 1400 rpm full load, B50 has about 50% of the flame area at temperature of 2400 K in the angular rage 9-30 cad ATDC; this trend is quite similar to diesel fuel. However, B50 has larger number of pixels at 2700 K with a maximum value of 50% at about 18 cad ATDC. B100 shows lower temperature, at both 2400 and 2700 K with respect to diesel fuel and B50. At 2000 rpm full load, all fuels have about the same flame area at 2400 K while B100 shows larger number of pixels at 2700 K and in a wider angular range with respect to the other fuels.At 3400 rpm full load, no significant differences in the pixel number at 2400 K are detected for the tested fuels while, as observed in the previous operating condition, B100 has the largest flame area at 2700 K.

Figure 4.18 shows the temperature distribution at medium load conditions. It can be observed that the EGR strongly affects the flame temperature and, hence, the NO_x formation. At 1400 rpm medium load, there is no EGR for B100 and lower EGR level for B50 with respect to diesel fuel (Figure 3.6); consequently, the pixel number at 2400 K increases with the RME content. Moreover, high temperatures are detected in advance, resulting in increased residence time of the gas at high temperature, for B50 and, particularly, for B100. Moreover, low pixel number at 2700 K, about 10%, is detected just for blended and pure RME. At 2000 and 3400 rpm, the EGR level is quite similar for all the tested fuels. However, it can be observed that the EGR has a stronger effect on reducing the temperature of blended and pure RME with respect to diesel fuel. Diesel fuel, in fact, exhibits larger number of pixels at 2400 and 2700 K with respect to blended and pure biodiesel, in opposite trend with the full load conditions.

Due to the triple bond of N_2 molecules, temperatures of about 2000 K must be reached in order to split the molecules and to enable the formation of NO_x according to the Zeldovich mechanism. However, as soon as these temperatures are reached, the NO_x production increases exponentially with temperature. Therefore, it can be argued that higher is the flame temperature, higher the NO_x production. The effects of flame temperature on NO_x emissions will be better described in the section 4.4.

Figure 4.17. Normalized pixel number at temperature of 2000, 2400 and 2700 K, for diesel fuel, B50 and B100 at the engine speeds of 1400, 2000 and 3400 rpm, full load.
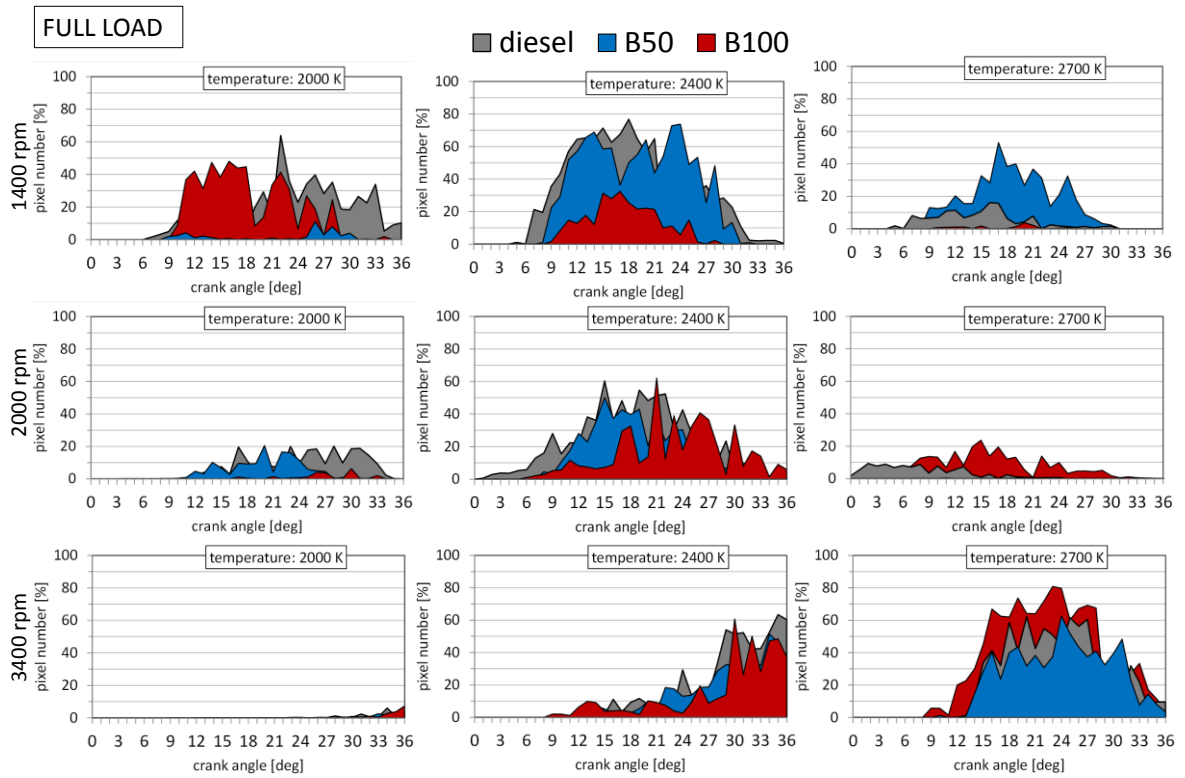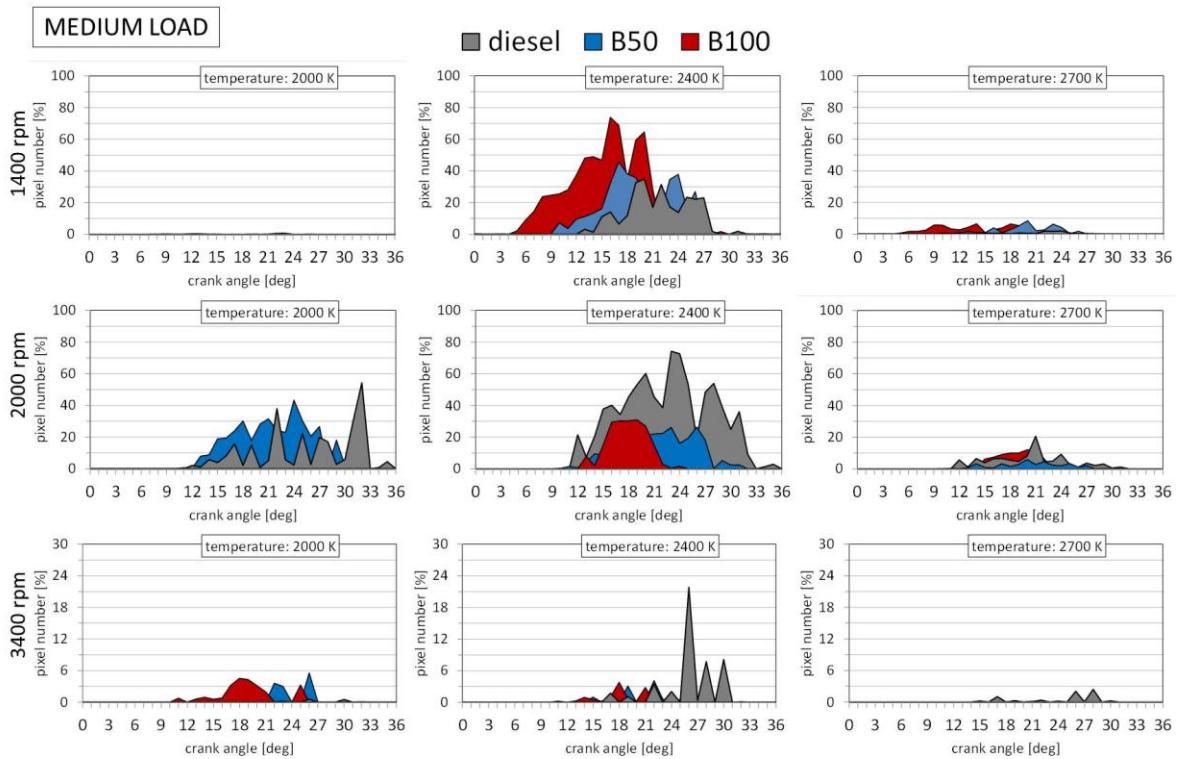

Figure 4.18. Normalized pixel number at temperature of 2000, 2400 and 2700 K, for diesel fuel, B50 and B100 at the engine speeds of 1400, 2000 and 3400 rpm, medium load.
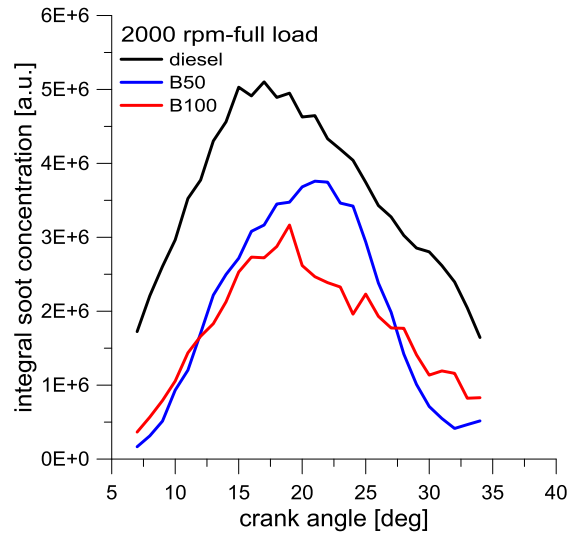
Figure 4.19. Integral soot concentration for diesel fuel, B50 and B100 at 2000 rpm full load.

The flame temperature knowledge allows to calculate the in-cylinder soot concentration. Soot images can be processed to calculate the integral soot over the time as shown in Figure 4.19 for the tested fuels in the operating condition at 2000 rpm, full load. The curves were obtained by summing the soot values of each pixel in soot map (Figure 4.14). They show a first rising portion representative of the soot production. They reach a maximum peak and then decrease as result of the soot oxidation. Diesel fuel shows the highest soot concentration and it decreases with the RME content.

As for the flame temperature, in order to better investigate the in-cylinder soot formation the local soot distribution was evaluated. Figure 4.20 and Figure 4.21show the pixel number with a soot concentration of 20, 60 and 105 a.u., normalized by the total pixel number, at full and medium load conditions, respectively. It can be observed that the larger flame area has low soot concentration (20 a. u.); a smaller fraction of zones have higher soot concentration (60 and 105 a. u.) that could affect strongly the PM exhaust emissions.

Figure 4.20. Normalized pixel number with a soot concentration of 20, 60 and 105 a.u., for diesel fuel, B50 and B100 at the engine speeds of 1400, 2000 and 3400 rpm, full load.

Figure 4.21. Normalized pixel number with a soot concentration of 20, 60 and 105 a.u., for diesel fuel, B50 and B100 at the engine speeds of 1400, 2000 and 3400 rpm, medium load.
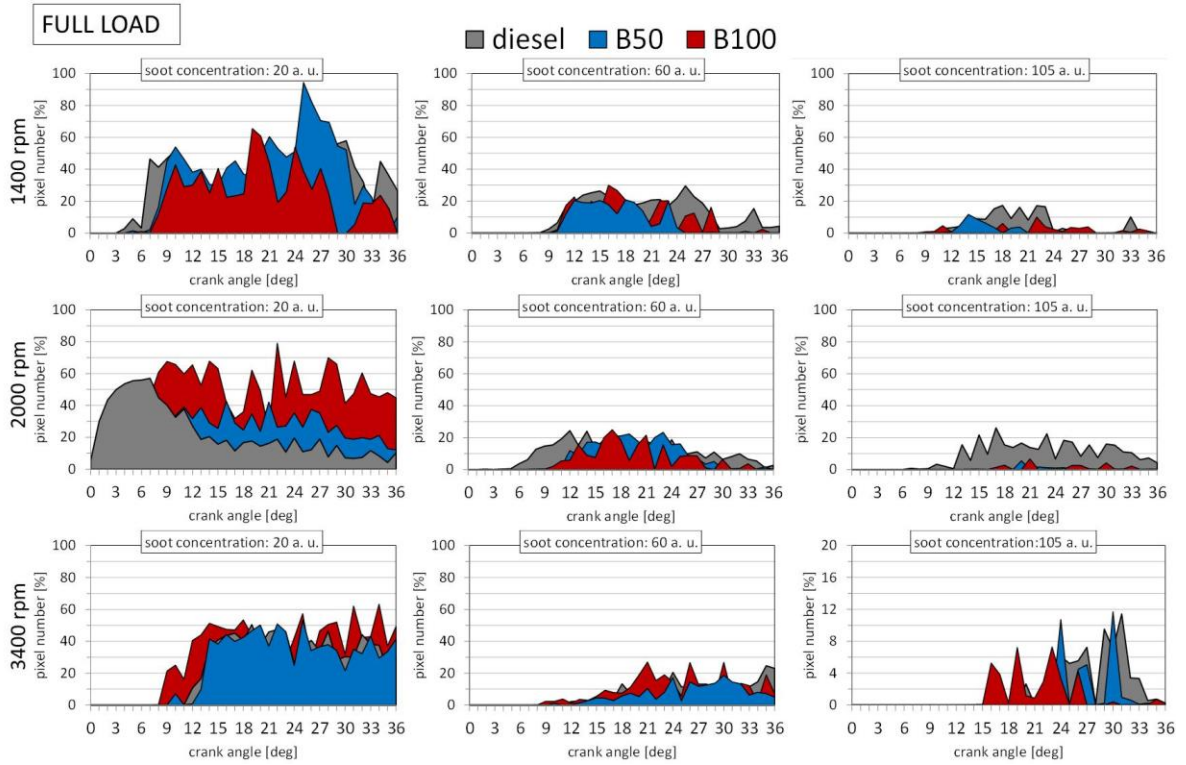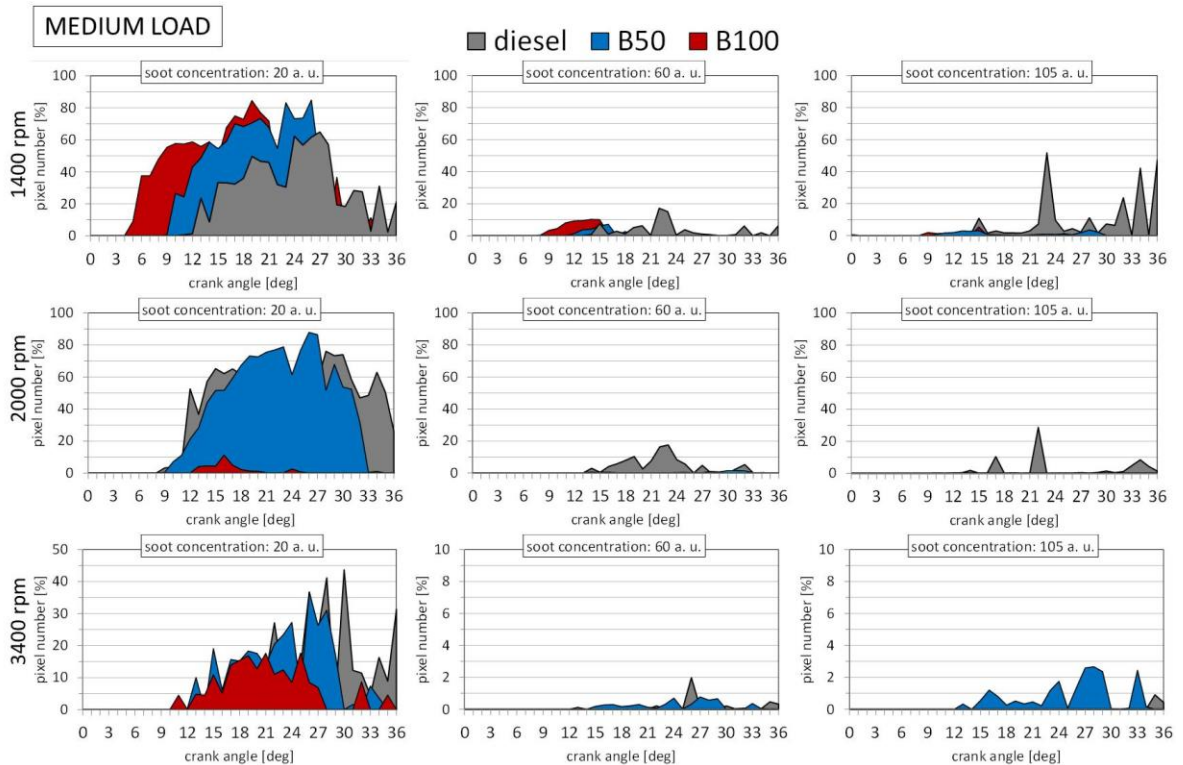
At 1400 and 2000 rpm, at both medium and full load, diesel fuel shows higher number of pixel with a soot concentration of 105 a.u. with respect to B50 and B100. The lower soot formation with RME can be ascribed to the oxygen presence in the biodiesel molecules. As well described by Sison et al. [46], in a diesel engine, soot precursors and soot primary particles form principally in the rich core regions of the fuel sprays, where oxygen availability is very low. In-cylinder turbulence breaks down the fuel sprays, allowing mixing with the turbulent cylinder contents, where the soot precursors and primary particles are subject to oxidation attack from air-borne oxygen and other combustion species (OH in particular). Oxygen, liberated from the molecules of the oxygenated fuels into the fuel-rich spray core could play an important role in the oxidative attack of the soot precursors and primary particles since soot oxidation does not have to rely just on air-borne oxygen. Significant oxidation, in fact, could be provided by the fuel-borne oxygen, directly within the rich spray core, where much of the soot is being produced and ahead of the time when air-borne oxygen starts to play a substantial role in soot oxidation. At 3400 rpm full load, B50 and B100 have a number of pixels with soot concentration of 105 a.u. comparable to diesel fuel as result of a not optimized combustion, characterized by a strong diffusive phase with blended and pure biodiesel, as pointed out also by indicating curves (Figure 4.9). Similar considerations can be done at 3400 rpm medium load. At this test point, B50 shows a portion of area with a soot concentration of 105 a.u. while for B100 the oxygen presence plays a more important role leading to low in-cylinder soot concentration.

Soot is formed from unburned fuel, which nucleates from the vapour to a solid phase in fuel-rich regions at high temperatures. Hydrocarbons or other available molecules could condense on, or be absorbed by soot. PM is the combination of soot and other liquid or solid phase materials that are collected during expansion and exhaust stroke. Therefore, higher is the in-cylinder soot concentration higher are expected the PM emissions at exhaust.

4.4   Exhaust emissions

The study on the feasibility of the engine under investigation for cogeneration purpose has been concluded with the pollutant emissions analysis. Figure 4.22 shows the gas emissions detected for all the tested fuels at different engine speeds and at both full and medium load.

It can be observed a reduction of CO and HC emissions for blended and pure biodiesel in agreement with the higher combustion efficiency shown in Figure 4.1. At full load, CO emissions increase up to a maximum value of at 1800 rpm (6 g/kWh for diesel fuel) and then decrease with the engine speed because of the better air-fuel mixing due to the higher turbulence. On the other hand, the increased engine speed results in shorter combustion duration and, hence, less time available for the CO oxidation; therefore, a slight increase in CO emissions is observed from 2600 rpm. Higher CO emissions are measured at medium load with respect to the full load conditions because of the EGR presence that reduces the temperature and the oxygen availability promoting the CO formation. Moreover, the EGR and the shorter combustion phase lead to increased CO with the engine speed, at medium load. Regarding the effect of fuel properties, a reduction in CO emissions when the engine is fuelled with blended and pure RME is observed at all the operating conditions. CO decrease is due to the oxygen content in the biodiesel that enhances a complete combustion, promoting the oxidation of CO into CO_2. HC emissions are very low at all the investigated conditions; however, it can be observed an increase in HC emissions with the engine speed, at both full and medium load, due to the shorter duration of the combustion phase. Moreover, HC emissions increase as the load decreases as result of the EGR presence. It can be noticed that blended and pure biodiesel emit lower amount of HC than diesel fuel at almost all the operating conditions. The general trend of HC reduction with biodiesel can be ascribed to the absence of aromatic compounds. Distillation curve also could affect HC formation in the cylinder and their emissions. Diesel fuel has higher final distillation points than biodiesel (Table 3.6); the final fraction of the diesel could not completely vaporize and burn, increasing HC emissions. The positive effect of RME on HC emissions is reduced at high speed and full load conditions. In these operating conditions, the combustion event of B50 and B100 is not properly phased (Figure 4.9) because the engine was not optimized to work with biodiesel, thus promoting HC formation.
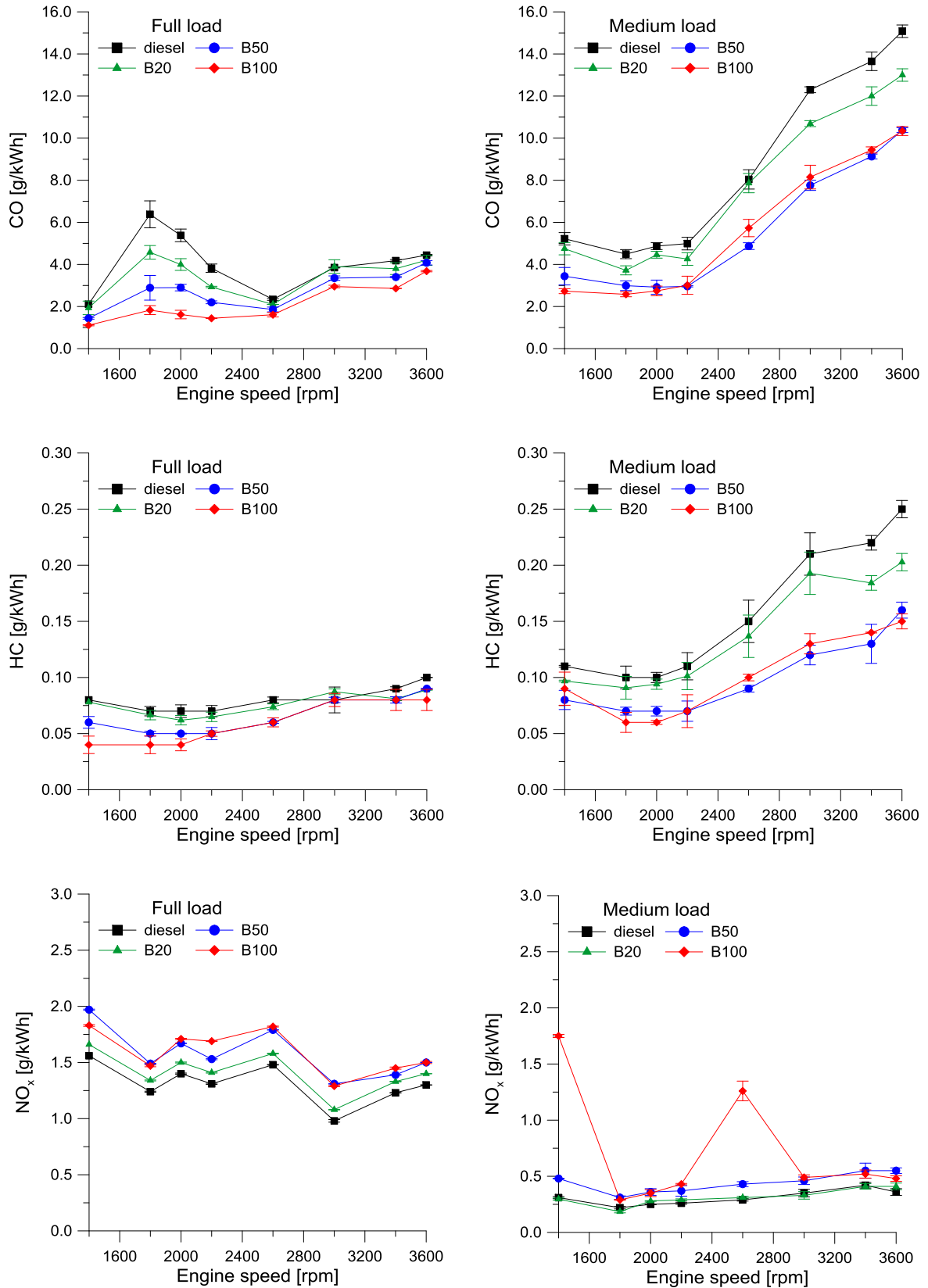
Figure 4.22. CO, HC and NO$_x$ emissions for all the tested fuels at different engine speeds and at full (left side) and medium load (right side).

The high temperature and the residence time of the gas at high temperature, coupled with the oxygen availability, are the main factors affecting the NO_x formation. At full load, blended and pure biodiesel emits larger amount of NO_x than diesel fuel resulting by the higher local flame temperature and the larger oxygen availability. In particular, at 1400 rpm, Figure 4.17 has shown larger flame area at temperature of 2700 K for B50 and higher NO_x emissions are detected at exhaust (Figure 4.22) with respect to pure RME. At 2000 and 3400 rpm, instead, B100 exhibits higher number of pixels at 2700 K and also larger NO_x emissions than B50. At medium load conditions, the effect of EGR has to be considered to explain the NO_x trend. EGR is more effective on temperature reduction for blended and pure biodiesel, as commented for Figure 4.18. Therefore, low differences in NO_x emissions are detected among the tested fuels due mainly to the higher oxygen content of biodiesel. A different behaviour is observed at 1400 and 2600 rpm for B100. In these cases, in fact, the ECU deactivates the EGR for B100 (Figure 3.6) leading to higher in-cylinder temperatures (as confirmed by optical measurement) that, together with the oxygen presence, promote the NO_x formation.

Figure 4.23 shows the PM emissions at the exhaust in both cases of diesel and pure RME fueling. PM values are represented as function of imep and engine speed through a contour-plot type map. PM emissions were measured at different engine speeds, at both full and medium loads and then the data were interpolated using a triangle-based cubic model over a uniform grid of speed and load points. The diesel fuel graph shows that PM emissions increase with the load. A high PM region is identified in the engine speed range 1600-2400 rpm between 10 and 11 bar of imep. The largest amount of PM is about 80 mg/m^3 and it is emitted at 2000 rpm, 11 bar of imep, corresponding to the full load condition. The PM emission graph referred to B100 is characterized by lower upper boundary than diesel fuel because the lower LHV of biodiesel does not allow to reach the same imep values of diesel fuel when the accelerator pedal throttle is fully opened. Also for B100, PM emissions increase with imep values with higher concentrations between 1600 and 2400 rpm and between 9 and 10 bar of imep.
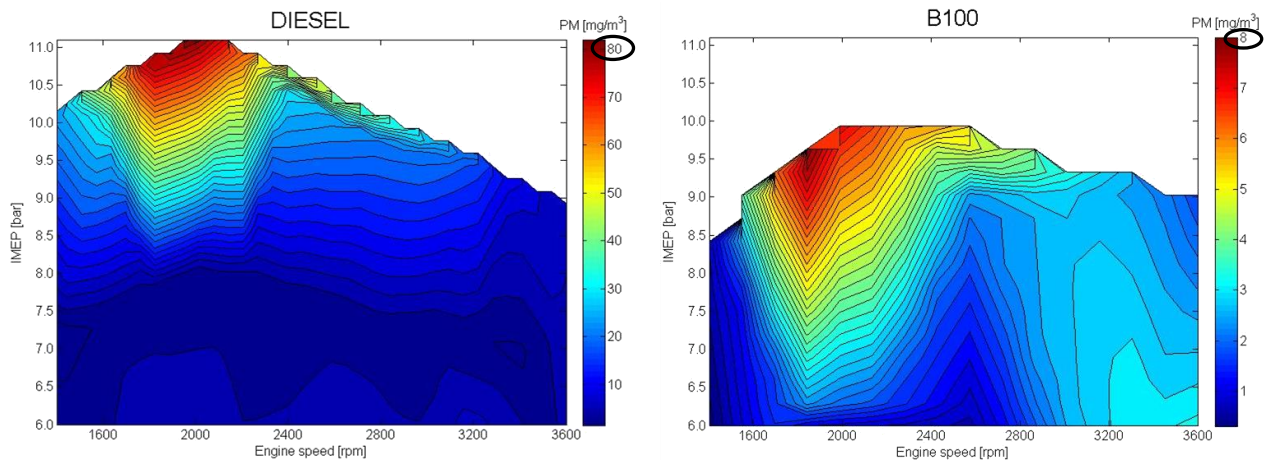
Figure 4.23. PM emissions for diesel fuel (left side) and B100 (right side) under mapping conditions.
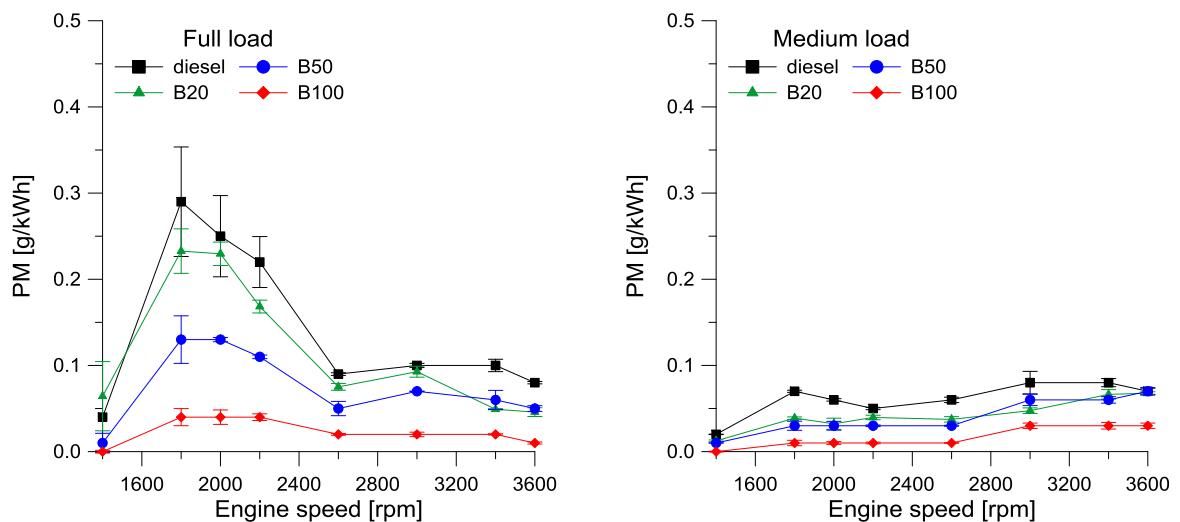
Figure 4.24. PM emissions for diesel fuel, B20, B50 and B100 at different engine speeds and at full (left side) and medium load (right side).

It is worth underlining that PM emissions for RME are one order of magnitude lower than diesel fuel. The largest concentration measured with RME is, in fact, about 8 mg/m^3. The reasons of PM reduction for RME with respect to diesel fuel are the larger oxygen content in the biodiesel molecule and the absence of PAH, considered soot precursors. In particular, the oxygen enables a more complete combustion even in the fuel rich diffusion flames as well as an enhanced particle oxidation. Moreover, it can be noted for B100 that PM emissions increase with engine speed. This result could be due to the more advanced and diffusive combustion as indicating data have shown (Figure 4.9).

Figure 4.24 shows the comparison of PM emitted from the tested fuels in the investigated conditions. The PM trend with the engine speed and load is similar to that described for CO,

since both emissions are related to the engine efficiency. PM emissions decrease with the content of RME in the fuel in agreement with optical measurements that have shown lower in-cylinder soot concentration for B50 and B100 with respect to diesel fuel. However, at 3400 rpm and at both medium and full load, optical measurements have revealed in-cylinder soot concentration of blended and pure RME comparable to diesel fuel, as expected also by indicating data that have shown a stronger diffusive combustion for B50 and B100. Altough the high in-cylinder soot concentration, B50 and B100 emits lower PM emissions than diesel fuel because of the high soot reactivity of biodiesel and its oxygen content that promote the oxidation of the formed soot.
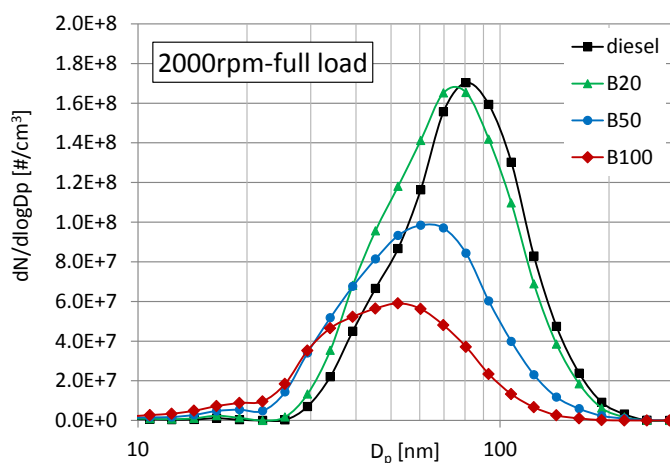
Figure 4.25. PSDFs for all the tested fuels at 2000 rpm full load.

Particle number and size give more valuable information than the mass alone because of the adverse effect of ultrafine particles (smaller than 100 nm) on environment and human health. Figure 4.25 shows the PSDF detected for the tested fuels in the operating conditions at 2000 rpm, full load. Particles range from 10 up to 200 nm for all the investigated conditions and fuels. PSDF is characterized by a bimodal behaviour. Nuclei mode ranges from 10 to 30 nm and it is mainly due to semivolatile components. In particular, nuclei particles are formed from semivolatile organic and sulphuric acid vapours originated from unburned fuel, lubricant oil and partial combustion products. Upon dilution and cooling in ambient air or during sampling, these vapours can either condense on pre-existing soot particles or nucleate to form nucleation mode particles. Accumulation mode ranges from 30 up to 200 nm and consists of fractal-like carbonaceous agglomerates [87]. These particles are formed in locally fuel-rich regions of the flame. The PSDFs show that the number of particles greater than 30 nm decreases as the

biodiesel content in the fuel increases. The peak of particle number, in fact, changes from 1.7E8 for diesel fuel up to 5.6E7 for pure RME. As above mentioned, this behaviour can be ascribed to the absence of aromatic hydrocarbons in biodiesel that reduce the soot precursor formation. Moreover, the peak size of accumulation mode decreases from 80 nm for diesel fuel up to 45 nm for RME because of the oxygen content in the biodiesel that causes particle to change from larger to smaller size [88]. Regarding the nuclei particles, they increase with the biodiesel blend ratio since biodiesel reduces the number of carbonaceous agglomerates typical of the accumulation mode that act as "sponges" and soak up volatile particles precursors [89]. Therefore, soluble organic fraction (SOF) condensation and adsorption on soot particles are weakened leading to the creation of more nuclei-mode particles. Another aspect that has to be considered is the higher viscosity and lower volatility of biodiesel that could result in slower evaporation and poorer air mixing with respect to diesel fuel. This could result in increased SOF and, hence, increased nuclei particles. Lastly, the oxygen content of biodiesel causes carbonaceous particles to change from fine size to ultrafine or nano-particle size [24].

In order to better analyse the effect of the fuel on particle number and size, the mean particle diameter (D_m) and the particle number (N) were taken into account. D_m was calculated as weighted average of diameters at each particle size class:

$$D_m = \frac{\sum_{i=1}^{n} D_{p,i} \cdot N_i}{\sum_{i=1}^{n} N_i}$$

(4.1)

where n is the total number of particle size classes, D_p is the particle diameter and N_i is the particle number concentration at the ith particle size class. As the particle size classes are logarithmically spaced, to convert $dN/dlogD_p$ to N, it is necessary to divide by 16:

$$N_i = \frac{dN_i / d \log D_p}{16}$$

(4.2)

where 16 is $dlogD_p$. By integrating the area under the curves $dN/dlogD_p$ over D_p, the total particle number was calculated.
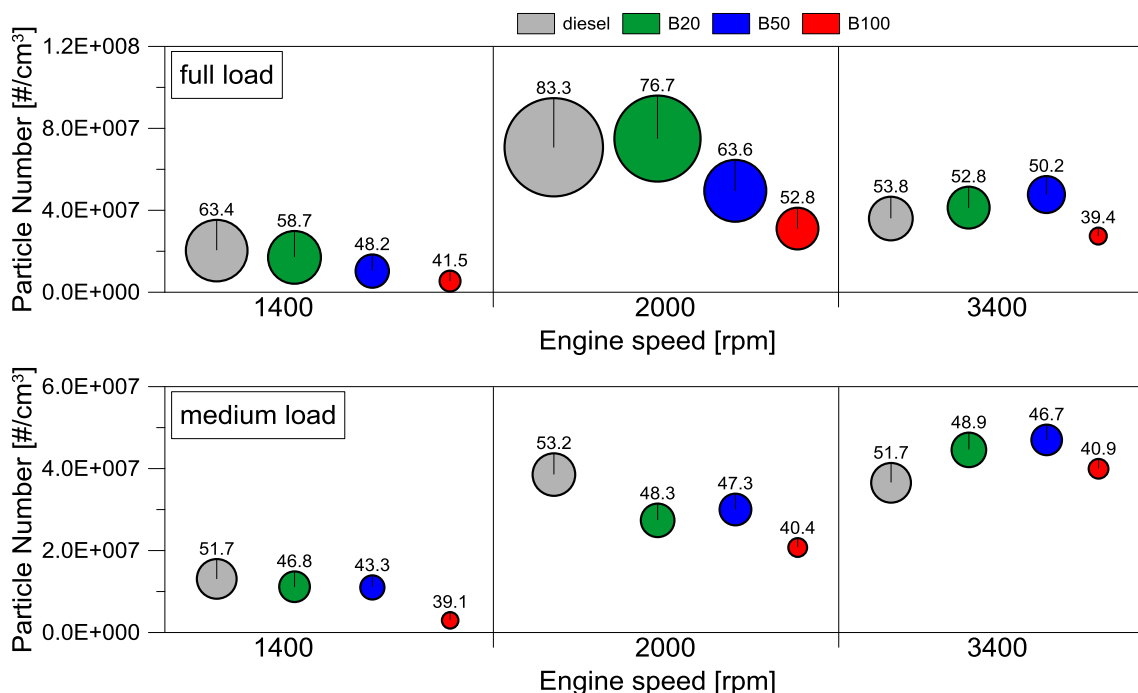
Figure 4.26. Particle number and diameter for all the tested fuels at the engine speeds of 1400, 2000 and 3400 rpm and at full (up) and medium load (down).

Particle number and diameter are represented in Figure 4.26 by means of a bubble chart: the y axis represents the particle number while the size of the bubble corresponds to the particle diameter. The data refer to the tested fuels in the operating conditions at 1400, 2000 and 3400 rpm, full and medium load. It can be observed that the particle number and size are strongly influenced by the engine operating conditions. At medium load, the particle number increases with the engine speed for all the fuels. At full load, the trend with the engine speed is not linear; the main difference is the largest particle number at 2000 rpm also observed for PM emissions. Mean diameters are larger at full load whit respect to the medium load conditions. At high loads, the combustion temperature and the amount of fuel injected increase while the air/fuel ratio decreases. These conditions promote the precursor soot formation and at the same time accelerate the agglomeration process. Regarding the effect of fuel, the general trend is a decrease of particle number and size as the content of RME increases. This behaviour is in agreement with optical measurements (Figure 4.20 and Figure 4.21). However, this trend is not followed at 3400 rpm; B50, in fact, emits larger number of particles than diesel fuel, as expected by optical data that have shown higher in-cylinder soot concentration for blended and pure biodiesel. However, because the higher soot reactivity, B100 emits smaller particles (Fig. 15).

Conclusions

Conclusions

Internal combustion engines could be considered attractive for small scale cogeneration applications because of their robust nature, higher efficiency in lower power range and lower capital cost with respect to other prime movers such as the turbines. ICEs are characterized by fast start-up capability, good partial load efficiencies and good operating reliability. Two types of ICEs are currently in use for cogeneration applications: SI engines, which are operated mainly with natural gas and CI engines. The latter have very good fuel consumption and are more efficient than SI engines since they operate at higher compression ratio. CI engines are characterized by higher durability, resulting in longer service life, due to the robust and heavy structure required to sustain the high combustion pressure. The main drawbacks of CI engines are related to the use of fossil fuels, the engine noise and the pollutant emissions. To solve these problems, alternative fuels, such as biodiesel, can be used. A key advantage of CI engines is, in fact, their fuel-tolerance. They can run with a variety of fuels such as diesel, heavy fuel oil, light fuel oil and vegetable oil. Finally, they can be set up to operate in dual fuel mode burning primarily natural gas with a small amount of diesel/biodiesel pilot fuel.

This thesis deals with an experimental investigation carried out on a CI engine for micro-cogeneration applications. The engine was a three-cylinder, 1028 cm^3 of displacement with a CR injection system. Tests were performed with diesel fuel, a blend of 20% v/v RME, a blend of 50% v/v RME and, lastly, pure RME. Experiments were carried out at steady state conditions at different engine speeds, from 1400 to 3600 rpm with a step of 200 rpm, at full and medium load. Energy analysis was performed to characterize the distribution of the supplied fuel energy to the engine; the waste heat recovery potentiality was investigated through exergy analysis. Indicating data were detected and the combustion noise was calculated. Gas emissions and PM were measured and particles were characterized in terms of number and diameter at exhaust. The pollutant formation was investigated by combustion phase detection through non-intrusive optical diagnostic. Flames images were post-processed by two-colour pyrometry method to assess the temperature and the radiation of sooting flames that were correlated to NO_x and PM emissions.

It was found out that B50 and, mainly, B100 has higher combustion efficiency than diesel fuel. The distribution of the different kinds of energy is influenced by engine working parameters. There is a trade-off between the waste heat of the exhaust gas and the cooling water: the heat recovered by exhaust gas increases with the engine speed and load; on the other hand, the largest amount of cooling water energy is available at low load and speed. Exhaust gas energy has the highest recovery potentiality because of the higher temperature at which it is available. Regarding the effect of fuel properties on energy distribution, a decrease of the heat recovered by exhaust gas is detected as the content of biodiesel increases meanwhile, there is no a definite trend for the cooling water energy with the biodiesel based fuels.

The engine total efficiency can be improved through recovery of exhaust gas and cooling water energy: the highest first low efficiency of the investigated engine based micro-cogeneration system is reached at high engine speed and load, in disagreeing with the engine efficiency.

Indicating data showed that the effect of biodiesel properties is evident mainly at high engine speeds. In these operating conditions, in fact, the combustion evolution for RME based fuels is more advanced and characterized by more lengthened diffusive tail with respect to diesel fuel. Lower noise emissions are detected with blended and pure RME.

Optical measurements based on two-colour pyrometry were performed in order to have a better understanding of combustion evolution and pollutant formation. It was proved that temperature detection through optical measurements provides more accurate information than indicating data. It was found out that RME based fuels has higher in-cylinder temperature with respect to diesel fuel and the EGR has a stronger effect on reducing the temperature of blended and pure RME. As result of the higher flame temperature and the larger oxygen availability, blended and pure RME emits larger amounts of NO_x. Lower in-cylinder soot concentrations were detected for B50 and B100 and, in agreement with optical data, lower PM emissions were measured at exhaust for biodiesel. Concerning particle number and size, biodiesel emits fewer particles of smaller diameter.

A novelty of the present work consists in employing non-intrusive optical diagnostic techniques for the optimization, mainly in terms of pollutant emission reduction, of a future cogeneration system. Results presented in this thesis have proved that blended and pure biodiesel could be used for a CI engine based micro-cogeneration system with benefits in

terms of both pollutant emissions and combustion noise reduction. However, thermodynamic analysis of combustion process has pointed out the need of dedicated injection strategies when the engine is fuelled with biodiesel. At some operating conditions, in fact, the injection strategy set for diesel fuel does not results in a properly phased combustion process when the engine runs with RME based fuels. Therefore, a proper engine calibration could help to further take advantage by the inherent exhaust emission reduction of biodiesel. A slightly increase of EGR, for example, could balance the biodiesel PM benefit for lower NO_x emissions. In this regards, optical diagnostic techniques could be a useful tool for a future adaptive control of the engine.

Results shown in this thesis work could be useful for the development of novel polygeneration platforms based on the fossil fuel and renewable sources technologies suitable for electrical and thermal energy production. The platforms could be developed considering the integration of different generation technologies, such as ICE, fuel cell, micro gas turbine, photovoltaic panel, wind turbine and energy storage systems. The issues of limited fossil fuels and their negative impact on the environment have led to the widespread of renewable resources in the supply of energy such as solar and wind; however, it is necessary to take into account their discontinuity and no programmability. Therefore, in the near future, ICEs will still play an important role in the energy production. Nevertheless, they could be fuelled with vegetable fuel, such as RME, overcoming the problem of fossil fuels depletion and limiting the issue of pollutant emissions.

APPENDIX A: Two-colour pyrometry method

The two-colour pyrometry method is the most widely used technique for diesel combustion studies. It allows to evaluate the flame temperature measurements and the in-cylinder soot concentration that provide useful information about the two exhaust emissions of most concern for a diesel engine, NO_x and PM, respectively [38-41, 46-55]. The theory of two-colour pyrometry is well described in [90-92]. The soot particles generated from the combustion process in a diesel engine are at high temperature and emit radiation in the visible and infrared spectrum. The two colour pyrometry involves the measurement of the radiation emitted by the incandescence soot particles at two wavelengths. Using these measurements and by making appropriated assumptions about the nature of the soot particles, it is possible to estimate the instantaneous flame temperature and the soot concentration. Since the two-colour method utilizes the thermal radiation from soot particles, it measures directly the temperature of soot particles. The temperature of combustion gases is not directly measured. However, it was found out that the differences between the two temperatures is negligible (<1 K) when the ambient gas and soot particles have attained thermal equilibrium [93] a condition that can be reached in about 10^{-5} to 10^{-6} seconds within the cylinder [94]. Therefore, it may be assumed that the soot particle and combustion gas temperatures are approximately the same. The intensity of radiation from a body varies with the wavelength and the temperature. This is described mathematically by Planck's equation:

$$E_{b,\lambda}(T) = \frac{C_1}{\lambda^5 (e^{(C_2/\lambda T)} - 1)} \qquad \text{(AA.1)}$$

where:

- $E_{b,\lambda}(T)$ [Wm^{-3}] is the monochromatic emissive power at temperature T;
- λ [μm] is the wavelength;
- C_1 is the first Planck's constant and it is $3.7418 \cdot 10^{-16}$ Wm^2;
- C_2 is the second Planck's constant and it is $1.4388 \cdot 10^{-2}$ mK.

The emissivity of soot particles can be estimated according to the empirical correlation due to Hottel and Broughton [95]:

$$\varepsilon_\lambda = 1 - e^{(-KL/\lambda^\alpha)} \tag{AA.2}$$

where:

− K is an absorption coefficient proportional to the number density of soot particles

− L is the geometric thickness of the flame along the optical axis of the detection system;

− α is a parameter depending on the physical and optical properties of the soot in the flame.

Matsui et al. [96] carried out a validation study of the above correlation by performing measurements of the soot emissivity at three wavelengths in a diesel engine. They concluded that in the visible range this is a correct functional relation between emissivity and wavelength. Using Equation A.2, the two color equation is obtained as follow:

$$KL = -\lambda^\alpha \ln\left[1 - \left(\frac{e^{(C_2/\lambda T)} - 1}{e^{(C_2/\lambda T_a)} - 1}\right)\right] \tag{A.3}$$

where T is the actual flame temperature and T_a is the apparent temperature, defined as the temperature of a blackbody that will emit the same radiation intensity as a non-blackbody at temperature T.

Since the product KL is constant, if two wavelengths are chosen, the right hand side of Equation A.3 can be solved for each wavelength as shown:

$$\left[1 - \left(\frac{e^{(C_2/\lambda_1 T)} - 1}{e^{(C_2/\lambda_1 T_{a1})} - 1}\right)\right]^{\lambda_1^{\alpha_1}} = \left[1 - \left(\frac{e^{(C_2/\lambda_2 T)} - 1}{e^{(C_2/\lambda_2 T_{a2})} - 1}\right)\right]^{\lambda_2^{\alpha_2}} \tag{AA.4}$$

If λ_1, λ_2, α_1 and α_2 are known, and the apparent temperatures are measured, Equation A.4 can be solved for the only unknown temperature. Once the value of the flame temperature has been estimated from Equation A.4, substitution of T back into Equation A.3 gives estimation for the value of the product KL which is proportional to the soot concentration.

APPENDIX B: Elaboration of exhaust emissions

The emission values were converted from ppm or % unit to g/kg_f by means of the air and fuel flow method [73]. Moreover, the knowledge of the engine bsfc allowed to express the emissions in g/kWh.

It is worth underling that diesel emissions are wet and mass calculations should employ concentration data on a wet basis; CO_2 is measured on dry basis and the conversion from dry to wet basis is approximated by the relation:

$$ppm[wet] = ppm[dry] \cdot \left(1 - y \cdot \frac{F}{A}\right) \tag{AB.1}$$

where y are the atoms of hydrogen per carbon atom; F and A are the mass of fuel and air per unit time, respectively.

The equations used to calculate mass emissions are the followings [73]:

- $CO[g/kg_f] = CO[\%] \cdot 28 \cdot 10 \cdot \dfrac{1}{M_{ex}} \cdot \left(\dfrac{\dot{m}_a + \dot{m}_f}{\dot{m}_f}\right)$ $\tag{AB.2}$

- $CO_2[g/kg_f] = CO_2[\%] \cdot 44 \cdot 10 \cdot \dfrac{1}{M_{ex}} \cdot \left(\dfrac{\dot{m}_a + \dot{m}_f}{\dot{m}_f}\right) \cdot \left(1 - y \cdot \dfrac{\dot{m}_f}{\dot{m}_a}\right)$ $\tag{AB.3}$

- $HC[g/kg_f] = HC[ppm] \cdot 13.85 \cdot 10^{-3} \cdot \dfrac{1}{M_{ex}} \cdot \left(\dfrac{\dot{m}_a + \dot{m}_f}{\dot{m}_f}\right)$ $\tag{AB.4}$

- $NO_x[g/kg_f] = NO_x[ppm] \cdot 46 \cdot 10^{-3} \cdot \dfrac{1}{M_{ex}} \cdot \left(\dfrac{\dot{m}_a + \dot{m}_f}{\dot{m}_f}\right)$ $\tag{AB.5}$

- $PM[g/kg_f] = PM[mg/m^3] \cdot 10^{-3} \cdot \dfrac{1}{\rho_{ex}} \cdot \left(\dfrac{\dot{m}_a + \dot{m}_f}{\dot{m}_f}\right)$ $\tag{AB.6}$

where $\dot{m}_a$ and $\dot{m}_f$ are the mass flow rate of the air and fuel, respectively. M_{ex} is the exhaust molecular weight; at fuel/air ratios leaner than 0.068, it can be assumed to be 29 and the density of the exhaust gas, ρ_{ex}, is that of the air. It was considered that CO has a molecular weight of 28. HC has an average hydrogen-to-carbon ratio of 1.85/1 and a molecular weight of 13.85. In accordance with present practise, NO_x mass determination is made in terms of NO_2 whose molecular weight is 46.

APPENDIX C: Analysis of in-cylinder pressure

In-cylinder pressure signal versus crank angle data can be used to obtain quantitative information on the progress of combustion. It allows to calculate the ROHR, the heat released (HR) and the mean temperature in the cylinder [57].

The ROHR is one of the most important parameter used to justify the combustion characteristics of a fuel; it influences the overall engine performance and emission formation. For heat release analysis, the cylinder is considered to be a thermodynamically closed system. According to the first law of thermodynamics, the energy balance of such a system can be expressed as [57]:

$$\frac{dQ}{dt} = \frac{dU}{dt} + \frac{dW}{dt}$$

(AC.1)

where dQ/dt is the rate of heat transfer to the system, dU/dt is the rate of change of internal energy of the system and dW/dt is the rate of work transfer from the system. The internal energy, U, can be expressed as:

$$U = mc_v T$$

(AC.2)

where m is the mass in the system, c_v is the specific heat at constant volume and T is the temperature. If the mass in the system is constant the derivative of U is:

$$\frac{dU}{dt} = mc_v \frac{dT}{dt}$$

(AC.3)

from the ideal gas law:

$$pV = mRT$$

(AC.4)

where V is the volume and R is the specific gas constant and with m and R assumed constant, it follows that:

$$\frac{dT}{T} = \frac{dV}{V} + \frac{dp}{p} \tag{AC.5}$$

Using Eq. AC.4 and AC.5, Eq. AC.3 can be rewritten in the form:

$$\frac{dU}{dt} = \frac{c_v}{R}\left(p\frac{dV}{dt} + V\frac{dp}{dt} \right) \tag{AC.6}$$

The work performed by the system can be expressed as:

$$\frac{dW}{dt} = p\frac{dV}{dt} \tag{AC.7}$$

Neglecting mass exchange and using Eq. AC.6 and AC.7, Eq. AC.1 can be rewritten as:

$$\frac{dQ}{dt} = \frac{c_v}{R}\left(p\frac{dV}{dt} + V\frac{dp}{dt} \right) + p\frac{dV}{dt} \tag{AC.8}$$

The specific gas constant can be expressed as:

$$R = c_p - c_v \tag{AC.9}$$

where c_p is the specific heat ratio at constant pressure. Eq. AC.9 and the ratio $\gamma = c_p/c_v$ can be used to simplify Eq. AC.8 into:

$$\frac{dQ}{dt} = \frac{\gamma}{\gamma-1} p\frac{dV}{dt} + \frac{1}{\gamma-1} V\frac{dp}{dt} \tag{AC.10}$$

It is of interest to study the heat release rate as a function of crank angle degree, θ, hence, Eq. AC.10 can be rewritten as:

$$\frac{dQ}{d\theta} = \frac{\gamma}{\gamma-1} p\frac{dV}{d\theta} + \frac{1}{\gamma-1} V\frac{dp}{d\theta} \tag{AC.11}$$

References

1. Cakir U, Comakli K, Yuksel F. The role of cogeneration systems in sustainability of energy. Energy Conversion and Management 2012; 63: 196-202.

2. Directive 2004/8/EC of the European Parliament and of the Council on the promotion of cogeneration, Official Journal of the European Union, 11 February 2004, 21.2.2004: L 52/50-L 52/60.

3. Goyal R, Sharma D, Soni SL, et al. An experimental investigation of CI engine operated micro-cogeneration system for power and space cooling. Energy Conversion and Management 2015; 89: 63-70.

4. European Parliament resolution of 12 September 2013 on microgeneration – small-scale electricity and heat generation (2012/2930RSP).

5. Aussant CD, Fung AS, Ugursal VI, Taherian H. Residential application of internal combustion engine based cogeneration in cold climate-Canada. Energy and Buildings 2009; 41: 1288-98.

6. Onovwiona HI, Ugursal VI. Residential cogeneration systems: a review of the current technology. Renewable & Sustainable Energy Reviews 2006; 10: 389-431.

7. Rosato A. Sibilio S. Energy performance of a micro-cogeneration device during transient and steady-state operation: Experiments and simulations. Applied Thermal Engineering 2013; 52: 478-91.

8. Dengler P. Geimer M. Zahoransky R. Potential of Reduced Fuel Consumption of Diesel-Electric APUs at Variable Speed in Mobile Applications. SAE paper 2011-24-0075.

9. www.energifera.com.

10. www.cummins.com.

11. Magno A, Mancaruso E, Vaglieco BM. Effects of a biodiesel blend on energy distribution and exhaust emissions of a small CI engine. Energy Conversion & Management 2015; 96: 72-80.

12. Magno A, Mancaruso E, Vaglieco BM, Energetic and pollutant emission analysis of a small diesel engine fuelled with diesel and diesel/RME blend. The 27th International Conference on Efficiency, Cost, Optimization, Simulation and Environmental impact of Energy Systems, ECOS2014, Turku, Finland, June 15-19, 2014.

13. Mastrullo R, Mazzei P, Vanoli R. Fondamenti di Energetica. Liguori Editore, Napoli, 1992.

14. Fu J, Liu J, Feng R, et al. Energy and exergy analysis on gasoline engine based on mapping characteristics experiment. Applied Energy 2013; 102: 622-30.

15. Abusoglu A, Kanoglu M. First and second law analysis of diesel engine powered cogeneration systems. Energy Conversion and Management 2008; 49: 2026-31.

16. Ozkan M, Ozkan DB, Ozener O, et al. Experimental study on energy and exergy analyses of a diesel engine performed with multiple injection strategies: Effect of pre-injection timing. Applied Thermal Engineering 2013; 53: 21-30.

17. Challen B, Baranescu R. Diesel Engine Reference Book. Butterworth Heinemann, Oxford, 1999.

18. Anderson L.G. Effects of Biodiesel Fuels Use on Vehicle Emissions. Journal of Sustainable Energy & Environment 2012; 3: 35-47.

19. Canakci M. Combustion characteristics of a turbocharged DI compression ignition engine fuelled with petroleum diesel fuels and biodiesel. Bioresource Technology 2007; 98: 1167-75.

20. Imran S, Emberson DR, Wen DS, et al. Performance and specific emissions contours of a diesel and RME fuele compression ignition engine throughout its operating speed and power range. Applied Energy 2013; 111: 771-77.

21. Di Iorio S, Magno A, Mancaruso E, Vaglieco BM. Effect of Diesel/RME Blend on Particle Emissions from a Diesel Engine for Quadricycle Vehicle. SAE paper 2014-01-1602.

22. Di Iorio S, Magno A, Mancaruso E, Vaglieco BM, Arnone L, Dal Bello L. Engine performance and emissions of a small diesel engine fueled with various diesel/RME blends", SAE paper 2014-32-0135.

23. Lapuerta M, Armas O, Rodriguez-Fernandez J. Effect of biodiesel fuels on diesel engine emissions. Progress in Energy and Combustion Science 2008; 34: 198-223.

24. Tan P, Ruan S, Hu Z, et al. Particle number emissions from a light-duty diesel engine with biodiesel fuels under transient-state operating conditions. Applied Energy 2014; 113: 22-31.

25. Agarwal AK, Dhar A, Gupta JG, et al. Effect of fuel injection pressure and injection timing on spray characteristics and particulate size-number distribution in a biodiesel fuelled common rail direct injection diesel engine. Applied Energy 2014; 139: 212-21.

26. Pope CA, Dockery DW. Health Effects of Fine Particulate Air Pollution: Lines that Connect. Journal of the Air & Waste Management Association 2006; 56(6): 709–42.

27. How HG, Masjuki HH, Kalam MA, et al. An investigation of the engine performance, emissions and combustion characteristics of coconut biodiesel in a high-pressure common-rail diesel engine. Energy 2014; 69: 749-59.

28. Mueller CJ, Boehman AL, Martin GC. An Experimental Investigation of the Origin of Increased NO_x Emissions When Fueling a Heavy-Duty Compression-Ignition Engine with Soy Biodiesel. SAE paper 2009-01-179.

29. Palash SM, Kalam M, Masjuki HH, et al. Impacts of biodiesel combustion on NO_x emissions and their reduction approaches. Renewable and Sustainable Energy Reviews 2013; 23: 473-90.

30. Tsolakis A, Megaritis A, Wyszynski ML, et al. Engine performance and emissions of a diesel engine operating on diesel-RME (rapeseed methyl ester) blends with EGR (exhaust gas recirculation). Energy 2007; 32: 2072-80.

31. Tompkins BT, Song H, Bittle JA, et al. Efficiency considerations for the use of blended biofuels in diesel engine. Applied Energy 2012; 98: 209-218.

32. Jena J, Misra RD. Effect of fuel oxygen on the energetic and exergetic efficiency of a compression ignition engine fuelled separately with palm and karanja biodiesels. Energy 2014; 68: 411-19.

33. Abedin MJ, Masjuki HH, Kalam MA, et al. Energy balance of internal combustion engines using alternative fuels. Renewable and Sustainable Energy Reviews 2013; 26: 20-33.

34. Ozturk E. Performance, emissions, combustion and injection characteristics of a diesel engine fuelled with canola oil-hazelnut soapstock. Fuel Processing Technology 2015; 129: 183-91.

35. Lahane S, Subramanian KA. Effect of different percentages of biodiesel-diesel blends on injection, spray, combustion, performance, and emission characteristics of a diesel engine. Fuel 2015; 139: 537-45.

36. Lesnik L, Iljaz J, Hribernik A, et al. Numerical and experimental study of combustion, performance and emission characteristics of a heavy-duty DI diesel engine running on diesel, biodiesel and their blends. Energy Conversion and Management 2014; 81: 534-46.

37. Ozener O, Yuksek L, Tekin A, et al. Effects of soybean biodiesel on a DI diesel engine performance, emission and combustion characteristics. Fuel 2014; 115: 875-83.

38. Magno A, Mancaruso E, Vaglieco BM. Experimental Investigation in an Optically Accessible Diesel Engine of a Fouled Piezoelectric Injector. Energy 2014; 64: 842-852.

39. Magno A, Mancaruso E, Vaglieco BM. Optical Investigation of Injection and Combustion Phases of a Fouled Piezoelectric Injector in a Transparent CR Diesel Engine. SAE Paper 2013-01-1591.

40. Magno A, Mancaruso E, Vaglieco BM, et al. Study on Spray Injection and Combustion of Fouled and Cleaned Injectors by means of 2-D Digital Imaging in a Transparent CR Diesel Engine. SAE Paper 2013-24-0062.

41. Di Iorio S, Magno A, Mancaruso E, Vaglieco B.M. Analysis of soot particles and NO_x in the cylinder and at exhaust of a compression ignition engine fuelled with RME and diesel fuel. MCS-13, Eighth Mediterranean Combustion Symposium, Çeşme, Izmir, Turkey, September 8-13, 2013.

42. Magno A, Mancaruso E, Sequino L, Vaglieco BM. Analysis of spray evolution from both piezo and solenoid injectors in single cylinder research engine. ILASS-2013, 25th European Conference on Liquid Atomization and Spray Systems, Chania, Greece, 1-4 September 2013.

43. Catapano F, Di Iorio S, Magno A, Sementa P, Vaglieco BM. A comprehensive analysis of the effect of ethanol and methane and methane-hydrogen blend on the combustion process in an optical PFI engine. Energy 2015; http://dx.doi.org/10.1016/j.energy.2015.02.051

44. Dec JE. A Conceptual Model of a DI Diesel Combustion Based on Laser-Sheet Imaging. SAE paper 970873.

45. Dec JE. Advanced compression-ignition engines-understanding the in-cylinder processes. Proceedings of the Combustion Institute 2009; 32: 2727-42.

46. Sison K, Ladommatos N, Song H, et al. Soot generation of diesel fuels with substantial amounts of oxygen-bearing compounds added. Fuel 2007; 87: 345-52.

47. Mancaruso E, Vaglieco BM. Premixed combustion of GTL and RME fuels in a single cylinder research engine. Applied Energy 2011; 91: 385-94.

48. Mancaruso E, Sequino L, Vaglieco BM, et al. Spray Formation and Combustion Analysis in an Optical Single Cylinder Engine Operating with Fresh and Aged Biodiesel. SAE International Journal of Engines, 2011; 4(1): 1963-77.

49. Mancaruso E, Sequino L, Vaglieco BM. First and Second Generation Biodiesels Spray Characterization in a Diesel Engine. Fuel 2011: 90(9): 2870-83.

50. Automotive Exhaust emissions and Energy Recovery. Apostolos Pesidiris, London, 2014.

51. Kong S, Ricart M., Reitz RD. In-Cylinder Diesel Flame lmaging Compared with Numerical Computations. SAE technical paper 950455, 1995.

52. Magno A, Mancaruso E, Vaglieco BM. Endoscopic investigation of combustion process in a small compression ignition engine fuelled with rapeseed methyl ester. SAE paper 2014-01-2649.

53. Magno A, Mancaruso E, Vaglieco BM. In-cylinder combustion process analysis of a small compression ignition engine fuelled with both blended and pure biofuel. The 12th International Conference on Combustion & Energy Utilisation – 12ICCEU, Lancaster, UK, September 29-October 03, 2014. Energy Procedia DOI: 10.1016/j.egypro2015.02.016.

54. Jeon, J, Lee JT, Lim YS, et al. Flame temperature distributions of biodiesel fuel in a single-cylinder diesel engine. Fuel Processing Technology 2013; 110: 227-34.

55. Aoyagi Y, Osada H, Shimada K. High EGR Rate Combustion and its Flame Temperature Observed by a Bore Scope System in a Heavy Duty Diesel Engine. THIESEL 2012 Conference on Thermo- and Fluid Dynamic Process in Direct Injection Engines, 11-14 September, Valencia, Spain.

56. Della Volpe R, Migliaccio M. Motori a combustione interna per autotrazione. Napoli, Liguori, 1995.

57. Heywood JB. Internal Combustion Engine Fundamentals. McGraw-Hill, New York, 1988.

58. Ferrari G. Motori a combustione interna. Torino, il capitello, 1996.

59. Zhao H. Advanced direct injection combustion engine technologies and development Volume 2: Diesel Engine. Woodhead Publishing, UK, 2009.

60. http://ec.europa.eu/eurostat

61. Sekmen P, Yilbasi Z. Application of energy and exergy analyses to a CI engine using biodiesel fuel. Mathematical and Computational Applications 2011; 4: 797-808.

62. Baumgarten C. Mixture Formation in Internal Combustion Engines. Germany, Springer 2006.

63. Musculus MPB, Miles PC, Pickett LM. Conceptual models for partially premixed low-temperature diesel combustion. Progress in Energy and Combustion Science 2013; 39: 246-283.

64. Torregrosa AJ, Broatch A, Pla B, Monico LF. Impact of Fischer-tropsch and biodiesel fuels on trade-offs between pollutant emissions and combustion noise in diesel engines. Biomass & Bioenergy 2013; 52: 22-33.

65. Tree DR, Svensson KI. Soot process in compression ignition engines. Progress in Energy Combustion and Science 2007; 33: 272-309.

66. Kittelson DB. Engines and nanoparticles: a review. Journal of Aerosol Science 1998; 29 (5): 575-88.

67. Resitoglu IA, Altinisik K, Keskin A. The pollutant emissions from diesel-engine vehicles and exhaust aftertreatment systems. Clean Technologies and Environmental Policy 2015; 17: 15–27.

68. www.pco.com.

69. www.horiba.com.

70. Zhao H, Ladommatos N. Engine Combustion Instrumentation and Diagnostic. SAE, Warrendale PA, 2011.

71. Atkins RD. An Introduction to Engine Testing and Development. SAE, Warrendale PA, 2009.

72. www.avl.com.

73. Measurement of Carbon Dioxide, Carbon Monoxide, and Oxides of Nitrogen in Diesel Exhaust. SAE J177 APR82.

74. www.tsi.com.

75. Andersson J, Giechaskiel B, Munoz-Bueno R, Sandbach E, Dilara P. Particle Measurement Programme (PMP) Light-duty Inter-laboratory Correlation Exercise (ILCE_LD) Final Report. European Communities, Luxembourg, 2007.

76. www.dekati.com.

77. Standard Specifications for Biodiesel Fuel Blend Stock (B100) for Middle Distillate Fuels. ASTM International Specification: ASTM D 6751, 2008.

78. Stone R. Introduction to internal combustion engines. SAE, Warrendale PA, 2012.

79. Canakci M, Sanli H. Biodiesel production from various feedstocks and their effects on the fuel properties. Journal of Industrial Microbiology Biotechnology 2008; 35: 431-41.

80. Rajasekar E, Selvi S. Review of combustion characteristics of CI engines fueled with biodiesel. Renewable and Sustainable Energy Reviews 2014; 35: 390-99.

81. Atadashi IM, Aroua MK, Abdul Aziz A. High quality biodiesel and its diesel engine application: A review. Renewable and Sustainable Energy Reviews 2010; 14: 1999-2008.

82. Holman J. Experimental methods for engineers. Singapore, McGraw-Hill, 1994.

83. Demirbas A. Progress and recent trends in biodiesel fuels. Energy Conversion and Management 2009; 50: 14-34.

84. Petchers N. Combined Heating, Cooling & Power Handbook: Technologies & Applications. The Fairmont Press, Lilburn, 2003.

85. Lesnik L, Vajda B, Zunic Z, et al. The influence of biodiesel fuel on injection characteristics, diesel engine performance, and emission formation. Applied Energy 2013; 111: 558-70.

86. Zhao H, Ladommatos N. Optical diagnostic for soot and temperature measurement in diesel engines. Progress in Energy and Combustion Science 1998; 24: 221-55.

87. Kittelson DB, Watts WF, Johnson JP. On-road and laboratory evaluation of combustion aerosols-Part1: Summary of diesel engine results. Journal of Aerosol Science 2006; 37: 913-30.

88. Chuepeng S, Xu H, Tsolakis A, Wyszynski M, Price P. Particulate Matter size distribution in the exhaust gas of a modern diesel Engine fuelled with a biodiesel blend. Biomass & Energy 2011; 35: 4280-89.

89. Kittelson, D, Abdul-Khalek I. Formation of Nanoparticles during Exhaust Dilution. EFI Members Conference Fuels, Lubricants Engines, & Emissions, January 18-20, 1999.

90. Zhao H, Ladommatos N. A Guide to Measurement of Flame Temperature and soot Concentration in Diesel Engines Using Two-Colour Method Part 1: Principles. SAE paper 941956, 1994.

91. Zhao H, Ladommatos N. A Guide to Measurement of Flame Temperature and soot Concentration in Diesel Engines Using Two-Colour Method Part 2: Implementation. SAE paper 941957, 1994.

92. Quoc HX, Vignon JM, Brun M. A New Approach of the Two-Color Method for Determining Local Instantaneous Soot Concentration and Temperature in a D.I. Diesel Combustion Chamber. SAE paper 91073, 1991.

93. Shack AZ. Temperaturedifferenz zwischen flame und kohlenstoffteilchen. Z Techn Physik 1925; 6(10) 530-40.

94. Baker HD, Ryder EA, Baker NH. Temperature Measurement in Engineering Vol. 2. Omega, Stamford, 1961.

95. Hottel H, Broughton F. Determination of True Temperature and Total Radiation from Luminous Gas Flames. Ind and Eng Chem 1932; 4(2): 166-74.

96. Matsui Y, Kamimoto K, Matsuoka S. A Study of the Time and Space Resolved Measurement of Flame Temperature and Soot Concentration in SI Diesel Engine by the Two-Colour Method. SAE paper 790491, 1979.